



Catalysts for the direct electrolysis of seawater

Moretti, Enzo Raffaele

Publication date:
2023

Document Version
Publisher's PDF, also known as Version of record

[Link back to DTU Orbit](#)

Citation (APA):
Moretti, E. R. (2023). *Catalysts for the direct electrolysis of seawater*. Technical University of Denmark.

General rights

Copyright and moral rights for the publications made accessible in the public portal are retained by the authors and/or other copyright owners and it is a condition of accessing publications that users recognise and abide by the legal requirements associated with these rights.

- Users may download and print one copy of any publication from the public portal for the purpose of private study or research.
- You may not further distribute the material or use it for any profit-making activity or commercial gain
- You may freely distribute the URL identifying the publication in the public portal

If you believe that this document breaches copyright please contact us providing details, and we will remove access to the work immediately and investigate your claim.

DTU Energy
Department of Energy Conversion and Storage

Catalysts for the direct electrolysis of seawater

Enzo Raffaele Moretti

Lyngby, 2023



Supervisor: Prof. Wolff-Ragnar Kiebach

Co-supervisors: Dr. Mikkel R. Kraglund & Dr. Ruth Knibbe

DTU Energy

Department of Energy Conversion and Storage

Technical University of Denmark

Anker Engelunds Vej

Building 310

2800 Kongens Lyngby, Denmark

Abstract

The deployment of renewable energy sources has accelerated in recent years, and consequently, one of their inherent challenges became increasingly relevant: The main sources of renewable energy, wind and solar, are intermittent in nature, and the production capacity therefore does not match the energy demand at all times. As a result, they are only base-load capable if the energy produced can be stored and reconverted again when needed. Apart from energy production, a complete decarbonization of society also implies that CO₂ free alternatives for industrial processes such as steel and cement production must be found. Hydrogen as an energy carrier can serve these purposes, and a general understanding has developed that green hydrogen production by means of water electrolysis will be a key technology to reach the above mentioned goals.

Although alkaline water electrolysis has been commercialized since the early 20th century, efficiency is still a major shortcoming of this technology. The work presented herein is therefore concerned with the development of highly active, noble metal-free catalysts for alkaline electrolysis and, more generally, the efficient exploration of the associated chemical spaces using machine learning guided experimentation.

The work conducted in the context of this thesis can be divided in three parts. In a first approach, a co-precipitation method was used to screen various combinations of single, binary and ternary metal hydroxides derived from eight different metals (Fe, Cr, Al, Co, Ni, Mn, Zn, Cu) with regard to their oxygen evolution reaction (OER) activity. The compounds are deposited directly onto Ni foam substrates, mimicking technical electrodes. Electrochemical tests were conducted in conventional and saline KOH to assess the suitability for direct seawater electrolysis. Samples containing Fe generally outperformed Fe free compositions, and NiFeCr showed the lowest overpotential of all samples with 247 mA cm⁻² in 1 M KOH. OER activity was found largely similar between the two electrolytes, although some compositions are identified with considerable differences in overpotential such as NiMn.

Subsequently, an autonomous experimentation system was designed based on the same synthesis method to optimize the OER overpotential in complex multi metal hydroxides. A combination of lab robotics, custom made instrumentation and machine learning guided optimization allows for extremely high experimental throughput and efficient material screening without human interaction. The system has the capability to independently test and optimize the material composition under practical conditions in a closed loop. To the best of the authors' knowledge, it is the first system of this kind applied to alkaline OER catalysts. First results illustrate the excellent data quality and reproducibility, as well as the general feasibility of the optimization approach. The trends known from previous manual experiments were reproduced with the autonomous system and multi metal doping showed high sensitivity of the overpotential with respect to the composition.

Lastly, highly porous Ni hydrogen evolution reaction (HER) catalysts are prepared by machine learning guided electrodeposition. The synthesis parameters current density, temperature, deposition time and ligand concentration are varied to increase the electrochemically active surface area and consequently HER activity. The best samples achieve 10 mA cm^{-2} at a very low overpotential of -117 mV, rivalling the most active reported Ni electrodes to date. The use of common laboratory instruments in connection with the human-in-the-loop approach makes this highly efficient workflow accessible to many researchers.

Resumé

Udbredelsen af vedvarende energikilder er accelereret i de senere år, og derfor er en af deres iboende udfordringer blevet stadig mere relevant: De vigtigste kilder til vedvarende energi, vind og sol, er periodiske af natur, og produktionskapaciteten matcher derfor ikke energibehovet på alle tidspunkter. Derfor kan de kun klare grundbelastningen, hvis den producerede energi kan lagres og omdannes igen, når der er behov for det. Bortset fra energiproduktion indebærer en fuldstændig dekarbonisering af samfundet også, at der skal findes CO₂-frie alternativer til industrielle processer som stål- og cementproduktion. Brint som energibærer kan tjene disse formål, og der har udviklet sig en generel forståelse af, at grøn brintproduktion ved hjælp af vandeletrolyse vil være en nøgleteknologi til at nå de ovennævnte mål.

Selvom alkalisk vandeletrolyse har været kommercialiseret siden begyndelsen af det 20. århundrede, er effektiviteten stadig en stor mangel ved denne teknologi. Det arbejde, der præsenteres her, handler derfor om udvikling af meget aktive, ædelmetalfrie katalysatorer til alkalisk elektrolyse og mere generelt om effektiv udforskning af de tilknyttede kemiske rum ved hjælp af maskinlæringsstyrede eksperimenter.

Det arbejde, der er udført i forbindelse med denne afhandling, kan opdeles i tre dele. I den første del blev der anvendt en samudfældningsmetode til at screene forskellige kombinationer af enkelte, binære og ternære metalhydroxider afledt af 8 forskellige overgangsmetaller (Fe, Cr, Al, Co, Ni, Mn, Zn, Cu) med hensyn til deres iltudviklingsreaktions (OER) aktivitet. Forbindelserne er deponeret direkte på Niskumsubstrater, der efterligner tekniske elektroder. Elektrokemiske tests blev udført i konventionel og saltholdig KOH for at vurdere egnetheden til direkte havvandselektrolyse. Prøver indeholdende Fe var generelt bedre end Fe-frie sammensætninger, og NiFeCr viste det laveste overpotentiale af alle prøver med 247 mA cm⁻² i 1 M KOH. OER-aktiviteten var stort set ens mellem de to elektrolytter, selvom nogle sammensætninger blev identificeret med betydelige forskelle i overpotentialet, såsom NiMn. Efterfølgende blev der designet et autonomt eksperimenteringssystem baseret på den

samme syntesemetode for at optimere OER-overpotentialiet i komplekse multimetallhydroxider. En kombination af laboratorierobotteknologi, specialfremstillet instrumentering og maskinlæringsstyret optimering giver mulighed for ekstremt høj eksperimentel gennemstrømning og effektiv materialescreening uden menneskelig interaktion. Systemet har evnen til uafhængigt at teste og optimere materialesammensætningen under praktiske forhold i et lukket kredsløb. Så vidt forfatterne ved, er det det første system af denne art, der anvendes til alkaliske OER-katalysatorer. De første resultater illustrerer den fremragende datakvalitet og reproducerbarhed samt den generelle gennemførlighed af optimeringsmetoden. Tendenserne kendt fra tidligere manuelle eksperimenter blev reproduceret med det autonome system, og multimetaldoping viste høj følsomhed af overpotentialiet med hensyn til sammensætningen.

Endelig fremstilles meget porøse Ni hydrogen evolution reaction (HER)-katalysatorer ved hjælp af maskinlæringsstyret elektroaflejring. Synteseparametrene strømtæthed, temperatur, aflejringstid og ligandkoncentration varieres for at øge det elektrokemisk aktive overfladeareal og dermed HER-aktiviteten. De bedste prøver opnår 10 mA cm^{-2} ved et meget lavt overpotential på -117 mV , hvilket er på højde med de mest aktive Ni-elektroder, der er rapporteret til dato. Brugen af almindelige laboratorieinstrumenter i forbindelse med human-in-the-loop-tilgangen gør denne meget effektive arbejdsgang tilgængelig for mange forskere.

Acknowledgements

I would like to take the opportunity to thank everyone who was part of my PhD journey, and who made it a fun and hopefully successful experience.

First of all my gratitude goes out to my supervisors. Ragnar Kiebach, for giving me the freedom to explore when possible and steering me back on track when necessary. Mikkel Kraglund, for great advice and great discussions, and obviously for encouraging me to buy overpriced bike parts. Ruth Knibbe as well as Jiayun Zhang, for hosting me during my external stay at the University of Queensland in Brisbane, for the valuable input they provided and generally for making me feel welcome during my time in Australia.

I would like to thank Michael Birch, Mike Wichmann, Axel Boisen, Ishaq Khaliqdad, Atli Olsen and Michelle Rydberg Jensen, who helped me on countless occasions with practical issues in the lab or the workshop.

A sincere thank you also to Veronica Humlebæk Jensen, Sofie Skov, Emilie Jacobsen and Emil Howaldt Christiansen, whom I had the pleasure of supervising in the lab, and for their contributions to my work.

To the office mates, colleagues and friends I met at DTU: David Tran, Fabian Buchauer, Andrea Russo, Benedikt Axel Brandes, Yujie Zhao, Nis Fisker-Bødker, Mads Radmer Almind, Alexandros Pasadakis-Kavounis, Pernille Pedersen, Xanthi Georgolamprou, Anastasiia Karabanova, Patricia Rabelo Monich, and totally also Dmytro Serhiichuk, thank you for the discussions, the support, the laughs we shared and the beers we had together.

Of course I also want to thank my family, who supported and encouraged me the best they could in what they thought was a "doctor's degree in being an inventor" (close enough, I guess).

And obviously my girlfriend Kateřina, for being understanding and patient and just all around awesome.

List of publications

journal publications

Paper I

Machine Learning Guided Development of High-Performance Nano-Structured Nickel Electrodes for Alkaline Water Electrolysis

Veronica Humlebæk Jensen, Enzo Raffaele Moretti, Jonas Busk, Emil Howaldt Christiansen, Sofie Marie Skov, Emilie Jacobsen, Mikkel Rykær Kraglund, Arghya Bhowmik and Ragnar Kiebach

Applied Materials Today (submitted)

Paper II

Screening study of transition metal hydroxides as catalysts for conventional alkaline and direct seawater electrolysis

Enzo Raffaele Moretti, Mikkel Rykær Kraglund and Ragnar Kiebach

to be submitted

Paper III

Autonomous catalyst development for alkaline OER

Enzo Raffaele Moretti, Nis Fisker-Bødker, Tejs Vegge, Mikkel Rykær Kraglund, Jinhyun Chang and Ragnar Kiebach

to be submitted

Paper IV

Lab scale 3-electrode holder for zero/controlled-gap electrode configuration fabricated using 3D printing

Fabian Luca Buchauer, Andrea Russo, Enzo Raffaele Moretti, Sarmad Iqbal, Mikkel Rykær Kraglund and Christodoulos Chatzichristodoulou

to be submitted

Contents

Abstract	i
Resumé	iii
Acknowledgements	v
List of publications	vii
Contents	ix
1 Introduction	1
2 Theoretical concepts	9
2.1 Water electrolysis technologies	9
2.1.1 Alkaline electrolysis	10
2.1.2 PEM electrolysis	13
2.1.3 Solid oxide electrolysis	14
2.1.4 Sea water electrolysis	15
2.2 Electrocatalysts for alkaline OER and HER	20
2.2.1 Hydrogen evolution reaction	23
2.2.1.1 HER catalysts	23
2.2.2 Oxygen evolution reaction	24
2.2.2.1 OER catalysts	26
2.3 Laboratory automation in materials research	29
2.3.1 High-throughput experimentation	31
2.3.2 Robotics	32
2.3.3 Machine Learning	37

3	Experimental test setups	39
3.1	PEEK planar near-zero-gap cell	39
3.2	Automated test setup	40
3.2.1	North Robotics N9 platform	40
3.2.2	Electrochemical test cell	41
3.2.3	Sample and vial holder	43
3.2.4	Gripper	44
3.2.5	Pump assemblies	45
4	Screening Study of transition metal hydroxides as OER catalysts for conventional alkaline and seawater electrolysis	47
4.1	Introduction	47
4.2	Manuscript draft	50
5	Autonomous Catalyst Development for alkaline OER	73
5.1	Introduction	73
5.2	Manuscript draft	75
5.3	Experimental obstacles and learnings	98
6	Machine Learning Guided Development of High-Performance Nano-Structured Nickel Electrodes for Alkaline Water Electrolysis	103
6.1	Introduction	103
6.2	Manuscript draft	105
	Conclusion	135
	Appendices	137
	Appendix A Journal articles	139
	Appendix B Drawings and pictures	147
	List of Figures	154
	List of Tables	159
	Bibliography	161

CHAPTER 1

Introduction

As of 2023, anthropogenic climate change¹ and its practical implications have transitioned from a distant theoretical projection into a tangible presence in our daily lives. Across the globe, weather events and climate extremes are already experiencing noticeable effects. The escalation in both frequency and severity of heat waves and heavy precipitation occurrences has been observed over most land areas since 1950. Distressingly, nearly half of all coastal wetlands have been lost within the past century, alongside an increase in agricultural and ecological droughts in specific regions. Numerous biological species have migrated towards the poles or to higher elevations as a response to rising temperatures. The repercussions extend to food and water security, as well as human well-being both physically and mentally. It is crucial to acknowledge that these events have either been directly caused or significantly influenced by climate change, which in turn is propelled by human-caused greenhouse gas emissions [2].

Around the middle of the 19th century, the industrial revolution has set off a rapid increase in the global demand for energy. Biomass, the primary source of energy for humankind up until that point, was not sufficient to satisfy this demand and consequently, new energy carriers were exploited - oil, coal and natural gas have since been driving the industrial development around the world. The parallel growth of the world's population and its rising standards of living have done their bit to increase energy demand from an estimated 8000 TWh in 1850 [3] to 70500 TWh in 1973 and 168300 TWh in 2021 [4]. The burning of fossil fuels and other hydrocarbons like firewood releases air pollutants like, among others, sulfur dioxide (SO₂), nitrogen dioxide (NO₂) and carbon monoxide (CO). According to the world health organization (WHO), 6.7 million premature deaths were caused by air pollution globally in 2019, rendering it one of the greatest environmental risk to health [5]. Unfortunately, severe air pollution and its effect on health is not the only drawback of fossil fuels.

¹The term climate change describes long-term shifts in average temperature and weather patterns [1].

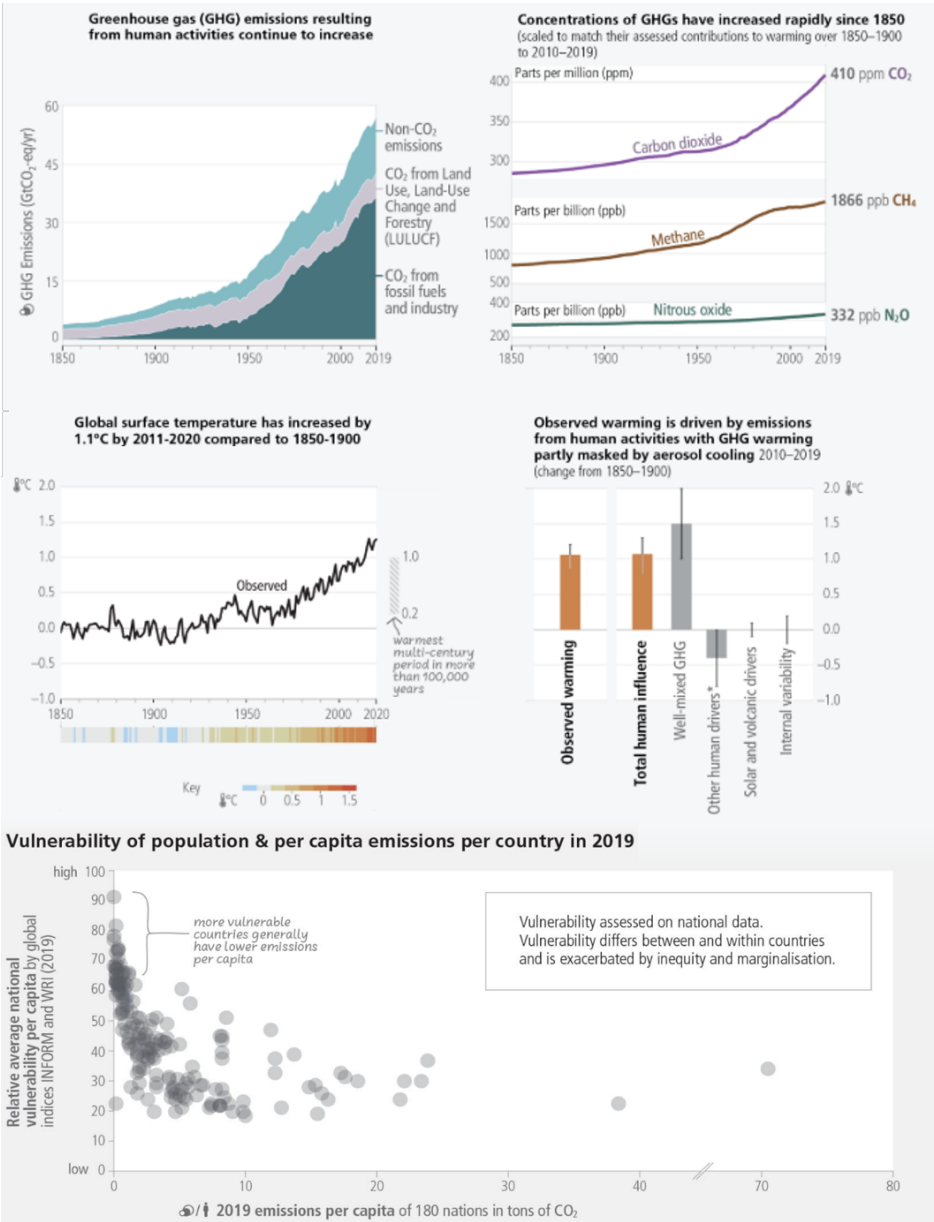


Figure 1.1. Top: Historic data (1850–2020) showing the increase in atmospheric greenhouse gas concentrations caused by human activities and the resulting increase global surface temperature; Bottom: Vulnerability of countries with respect to effects of climate change vs. the respective national CO₂ emissions per capita in 2019. Adapted from [2]

As a result of their growing consumption over the last two centuries, the emissions of greenhouse gases and consequently their concentration in the atmosphere rose significantly, in the case of CO₂ from 280 ppm in the pre-industrial era to 410 ppm in 2019 (see Figure 1.1) [2]. These gases trap some of the thermal infrared radiation emitted from the earth's surface in the atmosphere and by this cause the average global surface temperature to rise, also known as global warming.

Countries that historically emitted lower amounts of CO₂, thus making a lesser contribution to the greenhouse effect, ironically find themselves more vulnerable to the impacts of global warming compared to major emitting nations (see Figure 1.1).

The IPCC's 6th Assessment Report (AR6) shows that in order to limit the impact of these effects in the future, a drastic reduction in greenhouse gas emissions will be required from the 2020s onwards.

A key factor in achieving this is the rapid replacement of fossil fuel-based energy production with renewable energy. Although the deployment of renewable energy power plants continues to increase worldwide and is projected to increase even faster in the future [6], the absolute contribution to the primary energy supply is still very low [7, 8]. The combined energy supply from solar, wind, hydro, geothermal and ocean amounts to 5.5 % globally, and modern bioenergy to 6.8 % as of 2022. This compares to target values of 17.4 % and 13.1 %, respectively, which the IEA's net zero scenario calls for to be reached by 2030, which can only be achieved if the net deployment rate of renewables is accelerated even more. This task - already very challenging in itself - is further complicated by a characteristic of renewable energy

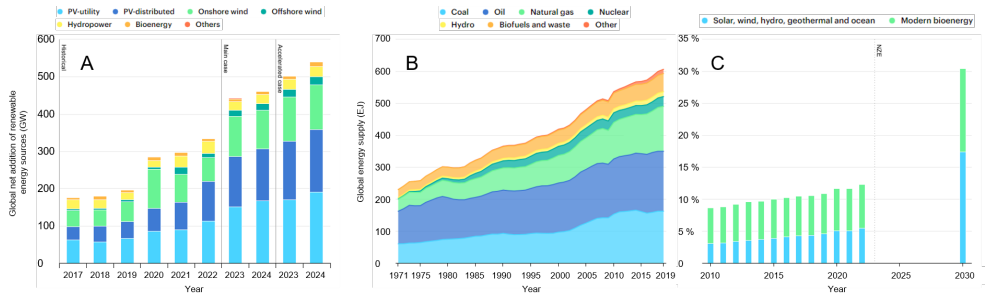


Figure 1.2. A: Global net addition of renewable energy sources (GW) (empirical for 2017-2022, projected for 2023-2024). B: Global energy supply by source (EJ) for 1971-2019. C: Relative contribution of renewable energy sources to the global energy supply for 2010-2022 and required contributions by 2030 according to the IEA's net zero scenario. Adapted from [6–8]

technologies that becomes increasingly relevant as their share of the energy supply rises: The two main sources of renewable energy, wind and solar radiation, are intermittent in nature. Unlike gas turbines and coal-fired power plants, their output cannot be precisely matched to the demand within short time frames - electricity is only available when the sun is shining or the wind is blowing and consequently, their production potential is also highly dependent on geographical factors such as average solar irradiance or wind speed. In practice, this means that at a regional level there are times with no supply at all and other times when the supply exceeds the demand. In the latter case, the excess energy must either be exported, stored or curtailed² in order to ensure grid stability. In many countries, the curtailment of renewable energies increases as their market share rises (see Figure 1.3) [9], since energy storage solutions are still scarce.

Pumped Hydroelectric Energy Storage (PHES) is an established technology that was first implemented in 1907 at the Engeweiher pumped storage facility near Schaffhausen, Switzerland [10]. It is by far the most widespread energy storage technology and accounted for 8500 GWh - over 90 % of the worlds energy storage capacity - in 2020 [11].

²Curtailment describes the deliberate reduction of power output in order to balance energy supply and demand or due to transmission constraints

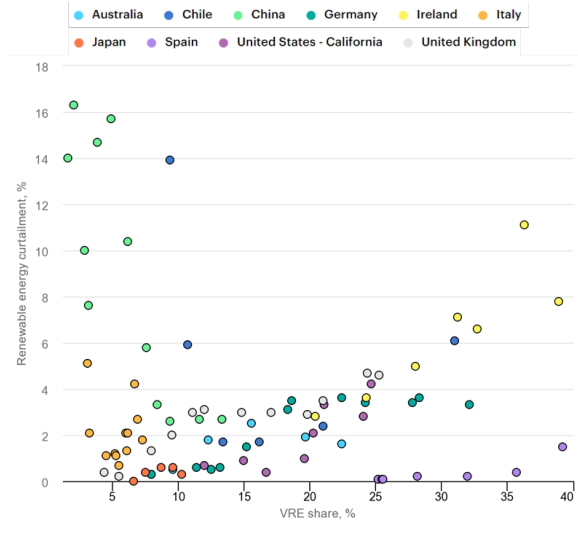


Figure 1.3. Relative curtailment of renewable energy in relation to their variable renewable energy (VRE) share for several countries (data from 2010-2022). Adapted from [6–8]

The process stores energy in the form of the gravitational potential energy of water pumped from a lower elevation reservoir to a higher elevation. Low-cost, off-peak surplus electricity is typically used to power the pumps. During periods of high electricity demand, the stored water is released through turbines to generate electricity. Unfortunately, the global potential for PHES is very limited, and it can't be used in geographically flat areas due to the lack of height difference between reservoirs - for example in Denmark or the Netherlands.

As Figure 1.4 shows [12], a wide range of alternative technologies is available, all with their individual strengths and shortcomings. Especially batteries have become increasingly relevant for transportation in the form of battery-electric cars, but also for grid balancing as of recently [11]. However, some of the most relevant application areas for energy storage cannot be addressed with most of the currently available technologies. Long-term storage requires very large storage capacities, which can not be achieved with batteries at present due to escalating costs. Although the energy density of batteries is fairly high, it is still not sufficient for long-distance and heavy-duty transport, air travel, or shipping. Hydrogen is a promising candidate to fill this

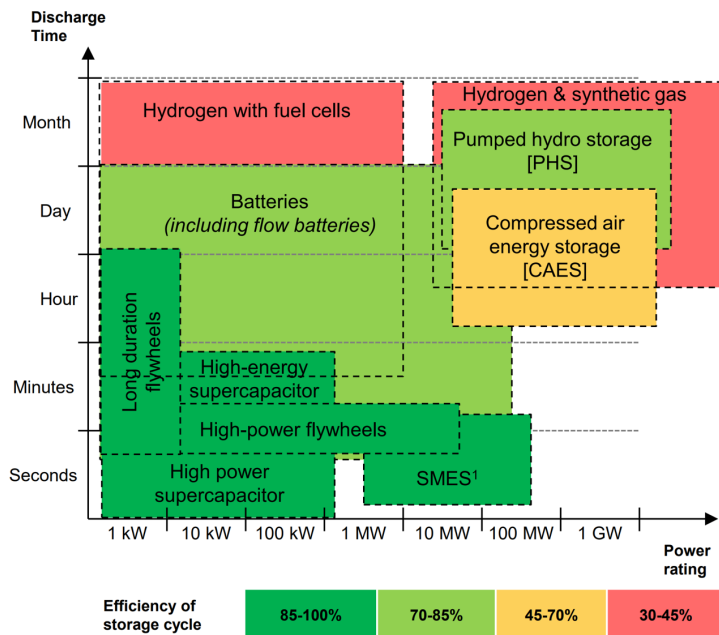


Figure 1.4. Comparison of different energy storage technologies in terms of discharge time, power rating and round-trip efficiency. From [12]

gap. Liquified or pressurized hydrogen is energy dense, can be stored for months, and unlike batteries its power and storage capacities can be scaled independently, qualifying it for long-term grid storage. It can be combined with CO , or CO_2 captured from the atmosphere into hydrocarbons such as Methanol, which is, in contrast to pure hydrogen, liquid at standard temperature and pressure. Additionally, it can be used as a chemical precursor to decarbonize CO_2 -intensive chemical processes such as in the steel and cement production [13].

The downside of hydrogen as an energy storage solution is its comparatively very low efficiency when considering a power-to-power scenario. The hydrogen has to be generated by means of electrolysis, is then usually compressed or cryogenically liquified and finally used to generate electrical energy again by a fuel cell. Even in the best-case scenario, this results in a round-trip efficiency of 29% [14] with state-of-the-art technology. Other pathways, such as via methanation or when reconverting the hydrogen by combustion, yield even lower efficiencies.

However, when combined with intermittent renewable energy sources, hydrogen production can be applied to reduce curtailment and make use of energy that otherwise would be completely lost. This allows for renewables to be base-load capable, which is difficult to achieve with other technologies as mentioned before. In this context, it has become a general understanding that hydrogen will play a crucial role in the decarbonization of society and that the demand for green hydrogen will as a result increase drastically over the coming years. The Net Zero Emissions Scenario for 2050, as envisioned by the International Energy Agency, projects a demand for a total installed electrolyzer capacity of 850 GW by 2030 and 3600 GW by 2050. This represents a staggering 7000-fold increase in less than three decades, considering that only 0.5 GW were operational by the end of 2021 [15]. This suggests that any emerging technology in this field must meet certain criteria, including the use of cost-effective materials, straightforward fabrication processes, and the ability to scale to terawatt-hour (TWh) levels for industrial application. Furthermore, to become economically viable, novel electrolyzers must surpass the efficiency of existing systems. The utilization of catalyst materials featuring high activity and composed of readily available elements offers a promising route to attain these goals.

The objective of this PhD project is to develop catalyst materials derived from abundant transition metals, both for the hydrogen evolution reaction (HER) and oxygen evolution reaction (OER) in alkaline conditions. An additional aspect under consid-

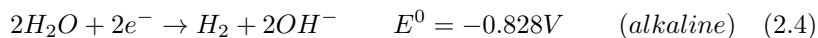
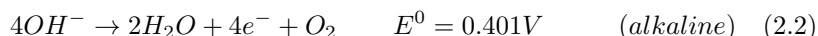
eration is their suitability for direct seawater electrolysis. This technology aims to use seawater without prior desalination as the electrolyte for water splitting. This might help to reduce cost, complexity and size of electrolyzer systems, potentially broadening their fields of application, especially when space constraints or access to freshwater are an issue. The experimental results are divided into 3 chapters. Chapter 4 is concerned with a screening study of metal hydroxides comprised of eight different metals (Fe, Cr, Al, Co, Ni, Mn, Zn, Cu) as OER catalysts for alkaline electrolysis. The samples are tested in both conventional, alkaline electrolyte (1 M KOH) and saline-alkaline electrolyte (1 M KOH + 0.5 M NaCl) as a seawater surrogate to assess how their OER activity is affected by the presence of NaCl. Based on the simple but effective synthesis route utilized in this work, in Chapter 5 an autonomous experimentation platform is designed for machine learning guided, high-throughput optimization of complex, multi metal hydroxides. The data quality and reproducibility of the system is presented, as well as the first screening and optimization results. In Chapter 6 machine learning is implemented into a Ni electrodeposition method in a human-in-the-loop approach. By varying process parameters (current density, temperature, ligand concentration and time), highly porous Ni electrodes are obtained with overpotentials as low as - 117 mV at 10 mA cm⁻².

CHAPTER 2

Theoretical concepts

2.1 Water electrolysis technologies

Water electrolysis describes the electrochemical splitting of water into molecular oxygen and hydrogen by means of applying an external electrical current. In its simplest form, an electrochemical cell for water electrolysis consists of two electrodes, the anode and the cathode, and an electrolyte. The redox reaction is split into two half-reactions, of which per definition the oxidation takes place at the anode and the reduction at the cathode. The electrolyte connects the two electrodes ionically, but isolates them electronically. Since the reaction involves an exchange of electrons, an electrical conduction path is necessary for the reaction to occur. When an external power supply is connected to the two electrodes, a current can flow and drive the reaction:



The potentials are given vs. standard hydrogen electrode (SHE). While the sum of the two half reactions remains the same (see equation 2.5), the exact reaction pathway depends on the availability of ionic charge carriers in the electrolyte and therefore on the pH value.

In a real electrolyzer, a mixing of the gases evolved at anode and cathode has to be

prevented, such that pure H_2 can be obtained and highly flammable mixtures¹ of H_2 and O_2 that pose a potential fire hazard are avoided. This is usually achieved by means of a diaphragm or membrane, the characteristics of which are a major contributor to the performance differences between the different electrolyzer technologies. It should be noted that there are also separatorless electrolyzer configurations discussed in recent literature [16], although investigations on such systems remain relatively rare.

2.1.1 Alkaline electrolysis

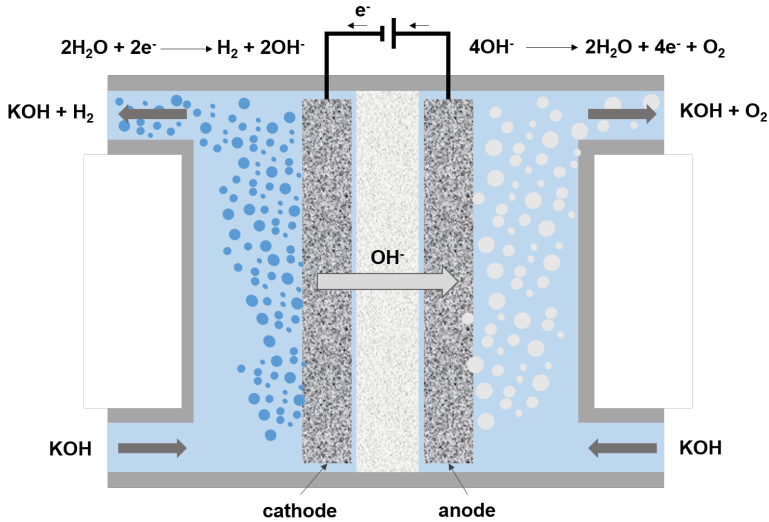


Figure 2.1. Schematic working principle of an alkaline electrolyzer.

Alkaline water electrolysis (AWE) is the oldest, most mature and most widely implemented water splitting technology. MW-scale systems have been commercially used for almost a century [17–19]. One of the advantages of AWE is that it does not rely on noble metal catalysts but can be operated with relatively common and inexpensive catalysts derived from transition metals like nickel, iron and cobalt. Despite that, the technology is not economically competitive with the extraction of hydrogen from fossil sources such as natural gas, coal and oil and thus only contributes around

¹The lower flammability limit for Hydrogen is generally accepted to be 4 mol%.

4% of the global hydrogen production to this day [20]. In a typical commercial cell,

Table 2.1. Typical operation conditions of state-of-the-art alkaline, PEM and SOEC electrolyzers [21–23]. Values marked with * are estimated from Figure 2.3.

	AWE	PEM	SOEC
Temperature	70 - 100 °C	50 - 80 °C	600 - 850 °C
Current density	0.2 - 1.2 A cm ⁻²	0.6 - 2.0 A cm ⁻²	0.5 - 2.0 A cm ⁻² *
Cell voltage	1.8 -2.4 V	1.8 - 2.2 V	1.0 - 1.5 V*
Pressure	< 40 bar	< 30 bar	< 25 bar
Target stack lifetime	< 90000 h	< 20000 h	< 20000 h
Voltage efficiency (HHV)	62 - 82 %	67 -82 %	> 100 %

metal (perforated) plates, meshes or foams are used as electrodes that are separated by porous diaphragms in a concentrated (up to 45 wt.%) alkaline electrolyte (aqueous KOH or NaOH) that is circulated through the cell. The separator is necessary to prevent the gas products from mixing while ensuring ionic contact between the electrodes. The operating temperature of modern alkaline electrolyzers is usually between 70-100 °C and mainly limited by the structural integrity of the separator [21]. Asbestos was widely used as a diaphragm material in commercial electrolyzers for a long time, however suffers from corrosion issues at elevated temperatures in highly alkaline solutions and was ultimately banned in the European Union by 2005 due to its toxicity [24, 25].

Today, the most commonly known porous separator uses a compound of zirconium dioxide (ZrO₂) and polysulfone (PSU) on a polymeric backbone and is sold under the trade name ZirfonTM (Agfa-Gevaert N.V.). ZirfonTM Perl UTP 500 is currently among the most used separators for alkaline electrolysis and rated for temperatures up to 110 °C. While this material is known for its good gas separation properties and high ionic conductivity, the porous structure of diaphragms generally demands relatively high thickness to prevent gas mixing. This results in large electrode distances and consequently high ohmic losses, which effectively limit the practical current densities (see Table 2.1) and decrease the overall efficiency of the electrolyzer. However, since the gas transport depends significantly on the microstructure and chemical surface properties of the diaphragm, improvements can still be expected in this area [26].

High temperature and pressure alkaline electrolysis

A relatively recent approach to alkaline electrolysis is the utilization high temperatures in order to accelerate reaction kinetics and ion conduction [27]. Although extra energy is supplied to the system in the form of heat, the overall thermodynamics allow an operation with improved efficiency compared to low temperature alkaline electrolysis. To circumvent the limitation of the operating temperature by the boiling point of the electrolyte, the cells are pressurized up to 87 bar and 400 °C [28].

Under these extreme circumstances, polymer based diaphragms like ZirfonTM are unstable and novel materials need to be developed. Titanate ceramics (BaTiO₃, CaTiO₃, SrTiO₃), Zirconates (f.e. YSZ) or NiO might be suitable candidates and have shown excellent performance with up to 1.0 A cm⁻² at 1.5 V vs. RHE [29,30], but their long term stability under the harsh conditions at high temperatures in strongly alkaline electrolyte remains to be proven.

Anion exchange membrane electrolysis

Another novel take on alkaline electrolysis is the replacement of the porous diaphragm with a polymer-based OH⁻-conducting membrane. This concept holds several advantages over conventional AWE. While noble-metal free catalysts can still be employed, the system can be operated with dilute KOH or even distilled water [31].

The absence of the highly corrosive concentrated KOH in this technology mitigates problem with leaking, allows for easier handling and can have positive effects of the cost and lifetime of auxiliary equipment in contact with the electrolyte. Additionally, the anion exchange membranes used are considerably less expensive than the polymer membranes commonly used in PEM electrolyzers. AEM electrolyzers have gained interest largely due to the potentially high performance it offers at low cost [32]. This technology has seen rapid development in recent years, and first commercial systems are available [33].

Alkaline electrolysis and the development of novel catalysts are the main focus of this PhD thesis. For this reason, an overview of the progress in catalyst development for AWE is given in greater detail in section 2.2.

2.1.2 PEM electrolysis

The first PEM electrolyzers were introduced in the 1960s in order to overcome the issues associated with alkaline electrolysis, such as low partial load range, low current densities, and low pressure operation [22]. This technology uses a H^+ -conducting, solid polymer electrolyte membrane and is referred to as polymer electrolyte membrane or proton exchange membrane electrolysis, both of which are known under the acronym PEM.

Although not as established as AWE, PEM electrolyzers have been available for about 25 years and the first commercial systems reaching the MW scale have been around since the early 2010s [34]. The polymer electrolyte membranes (the sulfonated fluouropolymer Nafion[®] (DuPont) being one of the most common ones) achieve very high proton conductivity and gas separation, and allow for compact systems operated at high pressures. The very low thickness of the membranes (20 - 300 μm) are to a large degree responsible for the advantages of the PEM electrolyzer, since it minimizes the ohmic losses caused by long ionic diffusion paths. Current densities above 2.0 A cm^{-2} , much beyond the current capabilities of AWE systems, can be achieved,

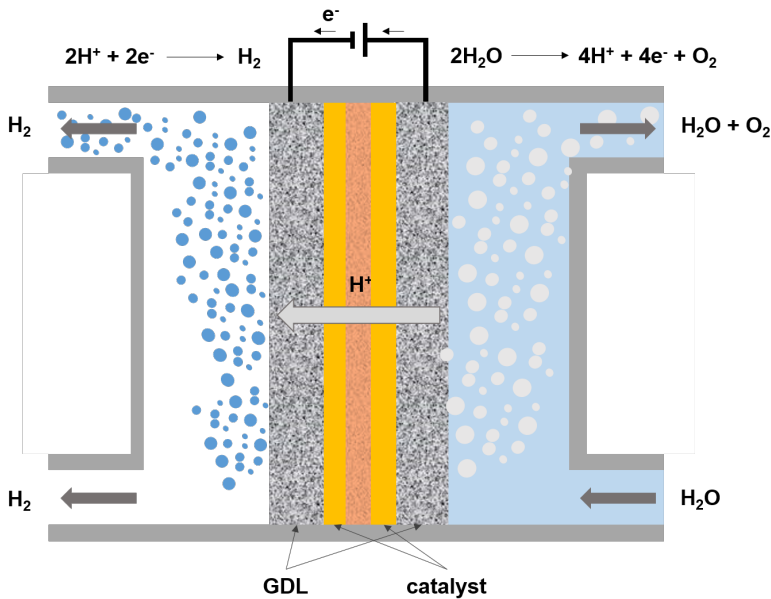


Figure 2.2. Schematic working principle of an PEM electrolyzer.

but come at the cost of a significantly reduced choice of materials.

Due to the very low pH in proximity to the membrane surface and the strongly oxidizing potentials, catalysts are practically limited to noble metals such as Platinum for the HER and Ir or IrO₂ for the OER. Current collectors and other auxiliary parts also need to be resistant to the corrosive environment and are typically made from Titanium. These material requirements, together with the high cost of the membranes, make PEM electrolyzers an expensive technology. Additionally, the harsh environment leads to lower lifetimes than AWE systems. Beyond that, especially the Iridium supply is extremely limited and might becoming a limiting factor if PEM electrolyzers were employed on a larger scale [35].

2.1.3 Solid oxide electrolysis

Among the three major water electrolysis technologies, solid oxide electrolysis is the most recent development. It was first presented in the 1980s [36] and is now on the verge of large scale commercialization. In the last two decades, the technology has seen immense development with a more than doubling of the electrochemical performance and an improvement of the long-term stability by a factor of ~ 100 [23].

Unlike alkaline and PEM electrolyzers, solid oxide electrolyzers (SOEC, Solid oxide electrolysis cell) operate at high temperatures in the range of 600 °C to 850 °C [37] and are consequently fed

with steam instead of liquid water. The dense ceramic electrolyte is capable of conducting oxide ions (O^{2-}) and typically consists of yttria-stabilized zirconia (YSZ). The electrodes are porous to ensure easy gas exchange and are made of a Ni-YSZ composite on the cathode and Sr-doped LaMnO₃ (LSM) or lanthanum-strontium(-ferrite)-cobaltite (LSC(F)) [38] on the anode side. Thin (0.1 to 5 μm) layers of gadolinia-doped ceria (CGO) are commonly used to prevent reaction between oxygen

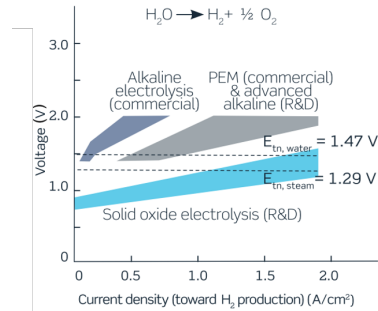


Figure 2.3. Performance comparison of AEM, PEM and SOEC water electrolysis technologies. Thermoneutral voltages for splitting of steam ($E_{tn,steam} = 1.29$ V) and water ($E_{tn,water} = 1.47$ V) highlighted with dashed lines. Adapted from [23]

electrode materials and YSZ [39]. Due to the high temperatures, the reaction kinetics of water splitting are much faster than for other technologies. As a result, the electrical efficiencies achieved with SOECs are far superior: An SOEC operated at thermoneutral potential for the splitting of steam (1.29 V) will attain an electrolysis current density of $\sim 1.5 \text{ A cm}^{-2}$, whereas AWE and PEM electrolyzers operated at thermoneutral potential for the splitting of liquid water (1.47 V) attain far lower current densities (PEM: $\sim 0.5 \text{ A cm}^{-2}$, AWE: $\sim 0.1 \text{ A cm}^{-2}$, see Figure 2.3) [23]. Another aspect that distinguishes SOECs from the other technologies is the possibility to operate in the so-called co-electrolysis mode, splitting a mixture of H_2O and CO_2 into syngas ($\text{CO} + \text{H}_2$) at the cathode and oxygen at the anode. At present, the capital expenditure (CAPEX) of SOEC systems is reported in the range of 1600 - 2400 €/kW [23,40], compared to the 800 - 1500 €/kW for AWM and 14-2100 €/kW for PEM electrolyzers [19,41]. These number however should be taken with a grain of salt, since the market for water electrolysis is rapidly changing and the CAPEX for all three types of electrolyzers are projected to decrease significantly over the next years [42]. Ultimately, the operational cost (OPEX) will be the decisive factor in choosing a specific technology over the others, and studies suggest that here the cost of electricity will be the main contributing factor [43].

2.1.4 Sea water electrolysis

All of the aforementioned technologies for water electrolysis heavily rely on pure water feeds. This demand can be satisfied as long as the hydrogen production capacity stays relatively small. However, according to the International Energy Agencies Net Zero Emissions Scenario, a globally installed electrolyzer capacity of 850 GW in 2030 and 3600 GW in 2050 will be needed [15] - an incredible 7000-fold increase over the ca. 0.5 GW that were operational by the end of 2021. Although the performance metrics of state-of-the-art electrolyzers in 2050 can not be predicted accurately, a simple estimation² yields a demand for pure, electrolysis compatible water of ca. 10^{11} kg per year.

Since the price of electricity is a significant component of the total cost of hydrogen production, many of the most promising geographical areas for large scale water electrolysis are located in coastal regions with ample wind and solar irradiation for cheap

²Assumptions: average electrolyzer efficiency (HHV) = 75%, average electrolyzer load = 25%, $\text{HHV}_{\text{H}_2} = 144 \frac{\text{MJ}}{\text{kg}}$.

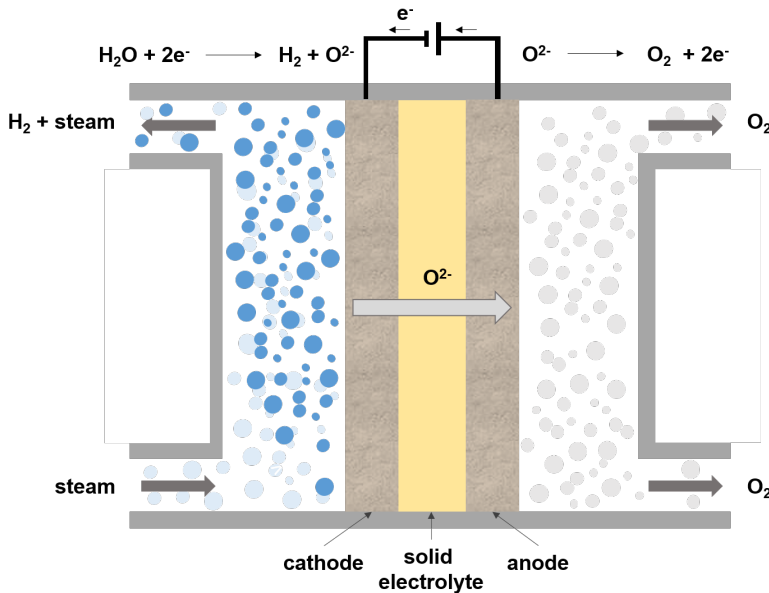


Figure 2.4. Schematic working principle of an solid oxide electrolyzer.

renewable energy generation. These areas however often see extremely little precipitation and therefore have limited access to fresh water, but a practically unlimited supply of seawater.

Unfortunately, seawater is everything but pure water and contains various impurities that can affect water electrolysis. The composition of seawater can vary somewhat depending on location, depth, and other factors, but usually includes organic compounds, such as dissolved proteins and tiny organisms, plankton, or sediment particles. The key challenge with respect to electrolysis are the dissolved salts in seawater, typically amounting to ca. 3.5 wt.%, most of which (ca. 3 wt.% or 0.5M) is NaCl. Cl^- is electrochemically active in a similar potential range and competes with the oxygen evolution reaction.

While formation mechanisms for different chlorine species are dominant depending on the pH, all of them are highly corrosive and must be avoided for water electrolysis operation. Broadly speaking, there are three different ways of achieving this: removal of chlorine or other redox active species from the seawater (desalination), or the suppression of the formation of corrosive species either thermodynamically or kinetically. There are several established technologies for the desalination of seawater

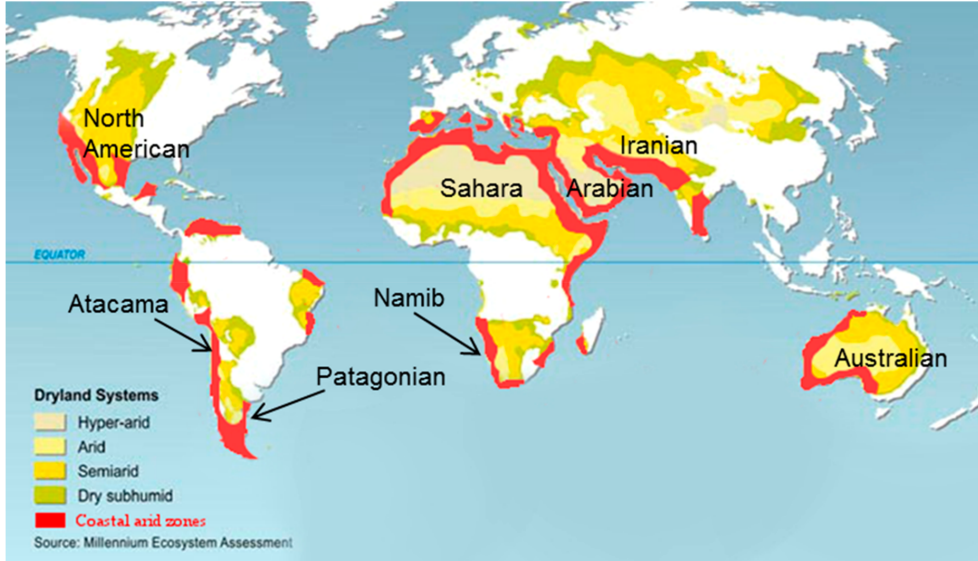
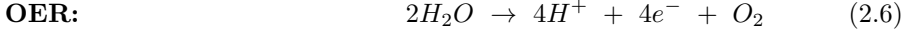


Figure 2.5. Global dryland areas with the coastal arid zones - potentially suitable for cheap hydrogen production from seawater - highlighted in red. From [44]

like reverse osmosis, nanofiltration or several types of distillation [45], but adding this preparation step of the electrolyte to the process adds technical complexity, makes electrolysis systems larger and more expensive to operate. The question whether or not direct seawater electrolysis can be a reasonable alternative to conventional alkaline or PEM electrolysis combined with seawater desalination is still debated in the research community [46, 47].

In 2016, Dionigi et al. investigate the thermodynamics involved in OER and chlorine oxidation and propose a design criterion for seawater electrolysis based on a Pourbaix diagram for a seawater surrogate (aqueous electrolyte with 0.5M NaCl, see Figure 2.6) [48]. They show that in acidic conditions, the chlorine evolution reaction (CER) is kinetically favored over the OER and is the dominant reaction. Additionally, its thermodynamic onset potential lies only marginally above the OER in low pH, which

leaves only a small potential window for water splitting:

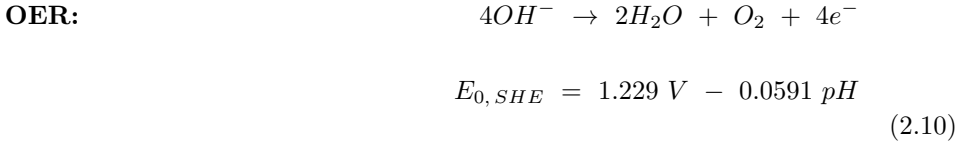


$$E_{0, SHE} = 1.229 \text{ V} - 0.0591 \text{ pH} \quad (2.7)$$



$$E_{0, SHE} = 1.36 \text{ V} \quad (2.9)$$

However, while still kinetically disadvantaged due to the complex, four intermediate reaction, the OER is thermodynamically highly favorable over hypochlorite formation, which is the dominant reaction in alkaline conditions:



$$E_{0, SHE} = 1.72 \text{ V} - 0.0591 \text{ pH}$$

Since both reactions are equally dependent on the pH, this can be translated into a useable overpotential window, in which OER can take place without the competing evolution of chlorine species:

$$\eta_{OER} \leq 480 \text{ mV} \quad \text{at } pH > 7.5 \quad (2.11)$$

They point out that, although this criterion doesn't describe the only operating conditions in which selective oxygen evolution from seawater electrolysis can be achieved, those conditions are the most favorable ones. To stay below 480 mV overpotential and still reach high current densities is already a tough requirement, especially if noble metal free catalysts are desired. If this window shrinks further, the task to avoid the evolution of chlorine species becomes unrealistic from thermodynamic considerations alone.

Besides this approach, other concepts have been proposed in recent years to make seawater electrolysis feasible. In 2020, Drespe et al. investigate several electrolyzer configurations based on anion exchange membranes [49]. Inspired by the working principle of PEM electrolyzers, they use different electrolyte feeds at anode and cathode to keep Cl ions away from the anode and thus prevent a competing reaction with

the OER. In their test setup, they prepare an membrane electrode assembly (MEA) consisting of $\text{Ni}_{0.66}\text{Fe}_{0.34}\text{-LDH}$ and Pt/C as catalysts for anode and cathode and a Tokuyama A201 anion exchange membrane.

With neutral seawater (0.5 M NaCl, pH 7-8) fed to the cathode and 0.5 M KOH to the anode, they achieve stable performance over 12 h at 200 mA cm^{-2} . In fact, even when operated with 800 mA cm^{-2} at 2.4 V cell potential, they find that the electrolyzer stayed fully selective towards the OER, despite small amounts of Cl^- found on the anode side after the test. This is attributed to the intrinsically selective properties of the NiFe-LDH catalyst. Over an extended period of operation (100 h), however, the cell voltage deteriorates substantially by ca. 100 mV. Rather than effects of evolving chlorine species, degradation of the anode catalyst, current collectors and particularly the AEM are identified as the main cause of this performance loss.

In 2023, the same group report an updated version of the asymmetric electrolyzer that is fed with an alkaline seawater surrogate (1 M KOH with salt mixture adding up to 3.5 wt. %) to the anode and consists of a custom AEM, NiFe LDH OER catalyst and CoP HER catalyst. At 60°C , they report similar stability over 100 h and a cell voltage below 2.0 V at 1 A cm^{-2} [50]. Besides AEM based technologies, other interesting and novel approaches to direct seawater splitting were reported, such as a Cl^- blocking layer structure of MgCo-MnO_2 on a Co(OH)_2 catalyst [51], PTFE membranes that block liquid water but are vapour permeable [52]. In early 2023 Guo *et al.* present a proton exchange membrane bases system in which the local reaction environment is adjusted by means of a water dissociation catalyst layer (Cr_2O_3) on top of the bifunctional OER and HER catalyst (CoO_x) [53]. In their fully symmetric setup (neutral seawater fed to both electrodes, Nafion 115 membrane, 60°C), they report 1 A cm^{-2} at an outstanding 1.87 V cell voltage.

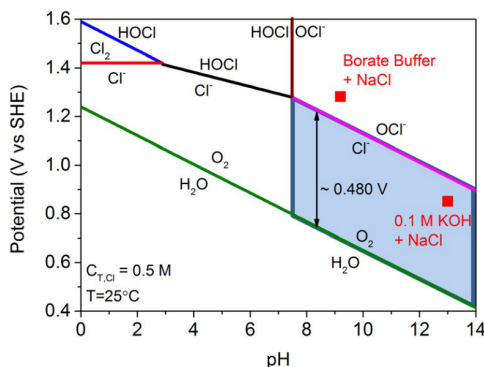


Figure 2.6. Pourbaix diagram for an artificial seawater model (aqueous electrolyte with 0.5M NaCl), showing the chlorine reactions competing with the OER in dependance of the pH. From [48]

2.2 Electrocatalysts for alkaline OER and HER

At the core, water electrolysis is a way to convert electrical energy into chemical energy by means of breaking and forming certain chemical bonds. The water molecule is split into its constituents, oxygen and hydrogen, of which usually only the hydrogen is of interest, since oxygen is already naturally one of the main components of the atmosphere. The energy that can be stored in this phase change is defined by the change in formation enthalpy of formation $\Delta_f H$ between reactant and products, given at standard temperature and pressure by:

$$\Delta_r H = \sum \nu \Delta_f H(\text{products}) - \sum \nu \Delta_f H(\text{reactants}) \quad (2.12)$$

$$= \Delta_f H_{H_2} + \frac{1}{2} \Delta_f H_{O_2} - \Delta_f H_{H_2O(l)} \quad (2.13)$$

Since the formation enthalpy for H_2 and O_2 are zero, this simplifies to

$$= - \Delta_f H_{H_2O(l)} \quad (2.14)$$

$$= \mathbf{285.8 \text{ kJ/mol}} \quad (2.15)$$

Upon the phase change of the liquid reactant to the gaseous products, the systems entropy changes. The maximum amount of energy that can be extracted from the process is defined by the change in the Gibbs free energy

$$\Delta G = \Delta H - T\Delta S \quad (2.16)$$

$$= \mathbf{237.1 \text{ kJ/mol}} \quad (2.17)$$

The positive sign denotes that the process of splitting liquid water into gaseous hydrogen and oxygen requires an external supply of energy. In the opposite direction (recombination to water via fuel cell or combustion), the sign becomes negative, the process is spontaneous and energy is released.

In an electrolysis cell, an external electric field drives the reaction, and the supplied energy can be expressed in terms of electrical work. An electrical potential, the *reversible potential*, can then be associated with the reaction according to:

$$E_{rev} = - \frac{\Delta G}{nF} \quad (2.18)$$

where $n = 2$ is the number of charges participating in the reaction and $F = 96485 \text{ C mol}^{-1}$ is the Faraday constant. However, if the reaction is conducted at potentials

between E_{rev} and the *thermoneutral potential* E_{tn} :

$$E_{tn} = - \frac{\Delta H}{nF} \quad (2.19)$$

the heat of the cell is consumed in order to balance the heat of vaporization spent for the reaction. In this case, the reaction is an endothermic process and additional heat input is necessary to maintain a constant temperature of the electrolysis cell. At E_{tn} , the reaction occurs isothermally. Beyond that value, the process is exothermic. Besides the temperature, pressure and concentration of the species involved in the electrochemical reaction influence the cell potential. Under equilibrium conditions, this relationship is described by the Nernst equation

$$E = E^0 - \frac{RT}{nF} \ln Q \quad (2.20)$$

$$E = E^0 - \frac{RT}{nF} \ln \left(\frac{a_{H_2} \cdot a_{O_2}^{1/2}}{a_{H_2O}} \right) \quad (2.21)$$

where R is the universal gas constant and a_x are the activities of the different species. The latter can be substituted by the partial pressure for gas phase reactions such as steam electrolysis, or concentrations for reaction in dilute solutions. However, electrolytes are usually strongly alkaline and due to gas evolution, the system involves both liquid and gas phase components, which makes the application of this relationship difficult in practice.

Away from the thermodynamic equilibrium, energy losses associated with kinetic effects cause the cell potential to be significantly higher than E_{rev} described in equation 2.18. Essentially, 3 types of contributions can be distinguished:

$$E_{cell} = E_{rev} + E_{\Omega} + E_{kin} \quad (2.22)$$

$$E_{cell} = E_{rev} + I \cdot R_{\Omega} + \eta_{an} + \eta_{cat} \quad (2.23)$$

Table 2.2. Reversible E_{rev} , and thermoneutral E_{tn} cell potentials for various temperatures at standard pressure.

Temp. [°C]	E_{rev} [V]	E_{tn} [V]
20	1.233	1.482
25	1.229	1.481
40	1.216	1.479
60	1.200	1.475
80	1.183	1.472

E_Ω scales linearly with the current I , and is caused by ohmic resistances R_Ω in the electrodes and from ionic migration through the electrolyte. Since the main contribution comes from migration, these losses can be reduced by decreasing the distance between the electrodes, or by applying novel materials with better ionic conductivity. E_{kin} can be divided into respective contributions from anode (η_{an}) and cathode (η_{cat}) which are also called overpotentials. They are intrinsic to the catalyst materials and can therefore be minimized by choosing active catalysts or providing a large electrochemically active surface area.

The Butler-Volmer equation relates the current density i to these reaction overpotentials η and the exchange current density i_0 , which describes the equilibrium forward and backward current density at $\eta_{cat} = 0$.

$$i = i_0 \left[\exp\left(\frac{\alpha n F}{RT} \eta\right) - \exp\left(-\frac{(1 - \alpha) n F}{RT} \eta\right) \right] \quad (2.24)$$

The charge transfer coefficient α ($0 < \alpha < 1$) is often assumed to be 0.5.

One of the most important properties of an electrolyzer is its efficiency. This term describes how much of the electrical energy that is put into the reaction (E_{cell}) is stored in the formation of oxygen and hydrogen (ΔH). In this context, two different definitions are typically used: The higher heating value (HHV) specifies the value with respect to the formation of liquid water ($\Delta H_{HHV} = -\Delta H_{H_2O(l)}$), the lower heating value considers the formation of water vapor ($\Delta H_{LHV} = -\Delta H_{H_2O(g)}$). At standard conditions this can be expressed as

$$\eta_{HHV} = \frac{\Delta H_{H_2O(l)}}{n F E_{cell}} = \frac{1.481V}{E_{cell}} \quad \text{(higher heating value)} \quad (2.25)$$

$$\eta_{LHV} = \frac{\Delta H_{H_2O(g)}}{n F E_{cell}} = \frac{1.253V}{E_{cell}} \quad \text{(lower heating value)} \quad (2.26)$$

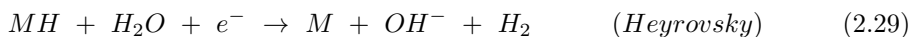
However, this definition only refers to the losses that occur through the dissipation of energy to heat. In practice, other factors can play a significant role, such as hydrogen loss, gas crossover and recombination. Additionally, the faradaic efficiency takes into account the fraction of electrons which does not participate in the water splitting reaction, but is lost to parasitic processes such as corrosion, oxidation and reduction of electrodes or hydrogen peroxide (H_2O_2) formation.

2.2.1 Hydrogen evolution reaction

The hydrogen evolution reaction (HER) under alkaline conditions proceeds through a two step process [54–56], involving the formation of a hydrogen intermediate on the catalyst surface by water dissociation



Followed by either chemical (eq. 2.28) or electrochemical (eq. 2.29) desorption and the resulting evolution of gaseous hydrogen.



The electrocatalytic activity with respect to the HER is to a large extent determined by the binding strength of the reaction intermediates to the catalyst surface [57]. In acidic media, platinum is well known to be an almost perfect HER catalyst in that respect. While still a very good catalyst in alkaline media, the activity is much lower, largely due to the increased complexity of the Volmer step (eq. 2.27), which involves water adsorption and hydroxide desorption.

2.2.1.1 HER catalysts

While this work is generally concerned with non-noble metal catalysts, Pt can still serve as a viable reference to compare other catalysts with. Apart from noble metals, a lot of different variations of Ni based catalysts for the HER have been reported with noteworthy performance. Especially NiMo compounds have shown exceptional HER activity, for example when prepared by electrodeposition or in the form of molybdenum doped Raney nickel. Wang *et al.* co-deposit a bimetallic, nanoporous NiMo catalyst with 20 % molybdenum content and achieve an extremely low overpotential of 10 mV at 10 mA cm⁻² in 1 M NaOH at room temperature [58]. They attribute the high performance to a combination of optimized Ni/Mo ratio, high surface area and the specific synthesis method. Comparable results have been published by several other groups as well, for instance by Jin *et al.*, which report 20 mV at 10 mA cm⁻² in 1 M KOH and very high specific surface areas of 169 m²g⁻¹ for their NiMo catalyst. The material is prepared by hydrothermal synthesis followed by annealing

at 450 °C on a Ni foam substrate. Other examples of highly active Ni based HER catalysts include Raney Ni, also referred to as spongy nickel. They are named after Murray Raney, who developed the material for the hydrogenation of vegetable oils in 1927 [59]. The materials are prepared by selective leaching of aluminium from NiAl alloys in concentrated NaOH solution. The remaining structure is highly porous and exhibits very large specific surface areas as a result. A similar effect can also be obtained with NiZn alloys. Other metals, such as molybdenum, can be incorporated in the alloy to improve the HER performance further. Los *et al.* reach 250 mA cm⁻² in 1 M NaOH at room temperature with regular Raney nickel at an already impressive 156 mV overpotential [60]. Addition of Mo (NiAl₃Mo_{0.153}) reduces this value to outstanding 57 mV in 1 M KOH.

Beyond Ni based catalysts, several other types of materials have shown good HER activity, for example Co or Mo based phosphides [61,62], carbides [63] and borides [64], or metal-free carbon based compounds [65]. Exfoliated NiFe LDH nanosheets coupled with negatively charged defective graphene has reached 20 mA cm⁻² at respectable 115 mV overpotential in 1 M KOH [66]. Table 2.3 shows an overview of selected reported catalysts for the alkaline HER.

2.2.2 Oxygen evolution reaction

The oxygen evolution reaction process is fundamentally more complex than the HER since it involves several intermediates and electron exchanges and therefore leads to higher overpotentials in most cases. The reaction pathway is still under debate, and several propositions have been made in the past [74–76]. A widely adopted understanding of the mechanism of oxygen evolution on metal oxide surfaces is based on a proposal of Rossmeisl *et al.* [77–79] and involves four intermediates. In this explanation, referred to as adsorbate evolution mechanism [80], the adsorption energy difference of *OH and *OOH intermediates is constant at 3.2 eV, also referred to as the scaling relationship, which predicts a fundamental lower limit for the OER overpotential of 370 mV from theoretical considerations.

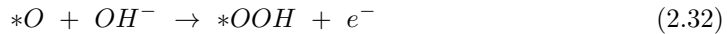
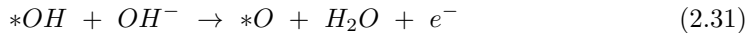


Table 2.3. List of representative non-noble metal-based electrocatalysts for the alkaline HER at room temperature ($\eta_{10} =$ overpotential at 10 mA cm⁻², RT = room temperature, C_{dl} = double layer capacitance). CC = carbon cloth, GCE = glassy carbon electrode, CMF = carbon micro flowers, NS = nanosheets, DG = defective graphene, CNT = carbon nano tube, PP = pressed powder, SP = sintered powder. ^a η measured at 20 mA cm⁻², ^b η measured at 250 mA cm⁻².

Catalyst	Electrolyte	η_{10} [mV]	Tafel slope [mV dec ⁻¹]	C_{dl} [mF cm ⁻²]	Stability at RT	Ref.
NiMo/Cu foam	1 M NaOH	10	-	47.36	1000 CV cycles/400 mV s ⁻¹	[58]
Ni ₄ Mo/Ni foam	1 M KOH	28	36	374	24 h at 10 mA cm ⁻²	[67]
Pt foil	1 M NaOH	36	-	-	-	[64]
Pt-C/Ni foam	1 M KOH	40	43	-	-	[68]
CoP/CC	1 M KOH	49	42.6	-	-	[61]
NiCo ₂ P _x /CF	1 M KOH	58	34.3	172.5	40 h at -0.106 V vs. RHE	[61]
CoMoB/GCE	1 M NaOH	66	67	34.7	30 h at -0.10 V vs. RHE	[69]
Mo ₂ C-CMF/GCE	1 M NaOH	100	65	0.38	40 h at -0.08 V vs. RHE	[64]
NiFe LDH-NS @ DG/Ni foam	1 M KOH	115 ^a	-	-	8 h at -0.105 V vs. RHE	[63]
					5 h at 100 mA cm ⁻²	[66]
NiSe ₂ /Ni foam	1 M KOH	120	-	-	12 h at 100 mA cm ⁻²	[68]
NiP/Ni foam	1 M KOH	130	58.5	23.1	24 h at -0.12 V vs. RHE	[70]
C ₃ N ₄ -CNT/carbon fiber	1 M KOH	131	79	-	$E_{cell} = 1.8$ V for 30 h	[65]
CoB/GC	1 M NaOH	166	-	0.24	-	[64]
Ni nanoparticles/GCE	1 M NaOH	180	111	2.605	100 ks at -1.5 V vs. Hg/HgO	[71]
Mo ₂ C PP	1 M KOH	190	54	-	48 h at -0.16 V vs. RHE	[62]
NiFe(OH) ₂ /Ni foam	1 M NaOH	210	-	-	$E_{cell} = 1.8$ V for 10 h	[72]
MoB PP	1 M KOH	220	59	-	48 h at -0.2 V vs. RHE	[62]
NiS/Ni foam	1 M KOH	230	123.3	4.2	24 h at -0.18 V vs. RHE	[70]
Ni(OH) ₂ /Ni foam*	1 M NaOH	245	-	-	-	[72]
Ni foam	1 M KOH	255	129	-	-	[68]
Ni foam*	1 M KOH	310	-	-	-	[70]
Ni foam*	1 M NaOH	355	-	-	-	[72]
Raney NiAlMo	1 M KOH	57 ^b	134	-	-	[73]
Raney NiAl	1 M NaOH	156 ^b	-	-	-	[60]

The mechanism is based on considerations in acidic conditions, but the general understanding is that it applies for alkaline conditions as well. Furthermore, it is not yet clear whether this mechanism also describes OER catalysis on other material surfaces such as metal hydroxides.

2.2.2.1 OER catalysts

Since the OER is responsible for a large fraction of the energy loss associated with water splitting, lots of research effort has been put into the search for and development of highly active and stable OER catalysts. IrO_x is still considered a benchmark in this regard, although not completely free of degradation issues in strongly alkaline conditions [81] and due to its scarcity and cost unfeasible for large scale employment. In their recent review on bulk and single atom catalysts for the OER, Iqbal *et al.* [80] give a good overview of the wide range of noble-metal free catalyst materials under investigation for alkaline water splitting, such as oxides, sulfides, phosphides and hydroxides (see Table 2.4). To improve the OER activity, common strategies include the fine tuning of the structure and introduction of metal dopants to the base material or encapsulation in conductive substrates, for example graphene or carbon nanotubes [80]. In 2014, Gerken *et al.* investigated almost 3500 compositions of ternary metal oxides ($\text{A}_x\text{B}_y\text{C}_z\text{O}_q$) in a screening study. They find that several nickel and cobalt based compositions show excellent performance. Several dopants increase the OER activity significantly, for example Cr, Sr or Ca, but Fe yield the largest effect with up to 4.8 times higher activity than the Ni oxide reference material. A lot of these general findings are also confirmed outside of this screening study, and Ni and Co oxides often are the basis of highly active catalysts.

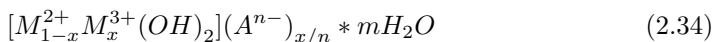
Tong *et al.* report a graphene based bifunctional electrocatalyst decorated with CoO_x nanoparticles for the oxygen evolution and oxygen reduction reactions, with low overpotentials of 295 mV at 10 mA cm^{-2} [82] in 0.1 M KOH. Wu and co-workers present mesoporous nanosheets of a Fe doped NiO with excellent performance, that only requires 206 mV overpotential to reach the same current density in 1 M KOH [83].

Within the oxide materials, the spinel and perovskite oxides have attracted particular interest. Spinel type oxides with the general formula AB_2O_4 ($\text{A} = \text{Ni, Mn, Cu, ...}$; $\text{B} = \text{Co, Fe, Mn, Cr, ...}$) have been heavily researched due to their excellent stability, while maintaining decent catalytic activity [84–86]. For this type of material, controlling oxygen vacancies seems to be a promising pathway to influence the OER

activity [87], as Peng and co-workers show on the example of a hollow structure of reduced NiCo_2O_4 (240 mV at 10 mA cm^{-2}) [88].

Perovskites have the general formula ABO_3 and extremely flexible elemental compositions, since both A- and B-site can accommodate multiple cations from the alkaline earth metals, alkali metals, lanthanides/actinides (A-site) or transition metals (B-site). Among these materials, lanthanum and strontium based compositions show favorable $^*\text{OH}$ binding energy [79] and are common research subjects. Many reported compositions with high OER activity also involve Ni, Co or Fe [89–93]. A well known issue with perovskites is the leaching of A-site cations (f.e. Sr) and resulting instability [94].

The materials that are most relevant for this thesis are metal hydroxides, in particular layered double hydroxides (LDH). The flexible composition makes the LDH properties tunable for various different applications such as CO_2 capture [95] and photocatalytic reduction [96] or as an alkaline OER catalyst. Although they show degradation issues in alkaline environments [97,98], these materials are PGM free, therefore prospectively cheap to produce and show exceptional OER performance [99–102]. They exhibit the general structure



In the LDH structure, some of the M^{2+} cations are substituted by M^{3+} cations (typically $x = 0.2 \dots 0.33$) in the brucite-like metal hydroxide layers. The created net positive charge is balanced by hydrated A^{n-} anions between the layers. The structure can accommodate a wide range of divalent (Co^{2+} , Ni^{2+} , ...) and trivalent (Fe^{3+} , Al^{3+} , ...) cations. Even M^+ and M^{4+} cations are possible, however limited to specific examples such as Li^+ and Ti^{4+} [103]. The interlayer anions are often supplied by the involved metal salts (NO_3^- , SO_4^{2-} , Cl^-), or by addition of anion sources during synthesis (CO_3^{2-}). Carrasco *et al.* [104] intercalate a range of organic surfactants into NiFe-LDH by means of an anion exchange reaction, and thereby increase the layer spacing by up to a factor of ~ 4 . They find an optimum in terms of OER performance for 25 Å (dodecyl sulfate) and Tafel slopes similar to exfoliated NiFe nanosheets for the most spaced LDH (octadecyl sulfate, 31.6 Å). However, LDH show a very high affinity for the intercalation of carbonate (CO_3^{2-}). Without maintaining a strictly carbonate-free environment, an anion exchange reaction will rapidly occur. For instance, even regular aqueous KOH may contain a certain amount of carbonate from dissolved atmospheric CO_2 over time. Interestingly, CO_3^{2-} intercalated LDH also show the best OER activity, which is presumably one of the

reasons why this aspect has otherwise not received much attention so far [101,105]. Under alkaline OER conditions, the LDH structure undergoes phase transformation similar to the one known from $\text{Ni}(\text{OH})_2$, which is illustrated in Figure 2.7. Under high potentials the metal ions oxidize further ($\text{M}^{2+} \rightarrow \text{M}^{3+}$, $\text{M}^{3+} \rightarrow \text{M}^{4+}$) and deprotonize to form oxyhydroxides, with interlayer distances close to those of the hydrous $\gamma\text{-NiOOH}$ phase ($\sim 7 \text{ \AA}$) [106]. Depending on their electrochemical history, mixed phases can occur, which is why these hydroxides are often referred to more generally as MO_xH_y .

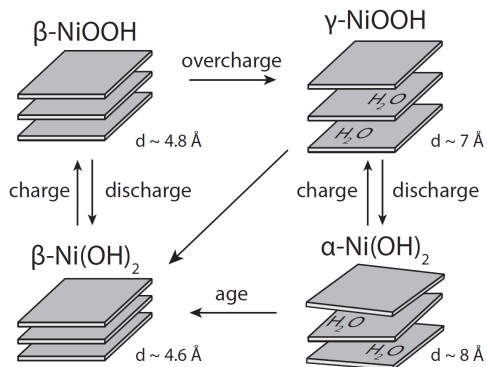


Figure 2.7. Bode diagram illustrating the different crystal phases of $\text{Ni}(\text{OH})_2/\text{NiOOH}$.

Many different synthesis routes have been reported for NiFe-LDH, such as hydrothermal synthesis [107–109], electrodeposition [110,111], co-precipitation [112,113] or even one-step self-assembly at room temperature [114].

Ni and Co based LDH have been a popular research subject in alkaline OER catalysis. The introduction of Fe in these structures increases their alkaline OER activity drastically. This so-called "Fe-effect" has been known in literature since the mid 1980s. Młynarek *et al.* [115] and Corrigan *et al.* [116,117] discovered that already very small Fe ppb to ppm levels of Fe in Ni electrodes can increase the OER activity manyfold. Since then, many hypotheses regarding the the exact mechanism that causes this effect have been presented, as a review from 2020 shows [118]. In the same year, Dionigi *et al.* use electrochemical measurements, in-operando techniques and DFT calculations to investigate the OER mechanism in NiFe LDH [106]. They provide evidence that the low overpotentials of *M*Fe LDH stem from O-bridged Fe-*M* reaction centers that stabilize OER intermediates, and based on that suggested the doping with redox-flexible cations as a general design principle for improved OER catalysts.

The flexibility of this structure allows for an enormous number of theoretically possible elemental combinations. The "Fe-effect" showcases that even very small changes in elemental composition can have a significant influence on the OER activity and consequently, various additional elements have been investigated. Amongst others,

V [107], Mo [119, 120], Co [108, 119], S [121], Ce [122], Fe^{2+} [123] and W [124] have been reported, usually on the basis of NiFe or CoFe LDH.

2.3 Laboratory automation in materials research

The demand for novel materials with properties tailored for specific applications is ever increasing. In many cases, this issue condenses to an optimization problem: In an extremely large array of possible material compositions and structures, which ones have the best properties for a certain task? The answer to this question is often too complex to be derived from first principles or via atomistic simulation, since it depends on material properties ranging across several length scales.

In many cases, screening through arrays of material compositions in a grid search is the viable option, but this approach remains extremely time-consuming and expensive. Once one has obtained a large amount of experimental data, it is not always straight forward to draw conclusions from them: the trends that exist between the different compositions and their performance figures might be described by a complex, non-linear function dependent on many input variables and invisible to the researcher without advanced data analysis techniques. Although the technology was not ready at the time, researchers have therefore attempted to outsource the process of gaining knowledge from experiments to artificial intelligence already in the 1960s [142]. It still took several more decades until the full automation of research, including the dynamic planning and execution of physical experiments, was realised.

In 2009, King *et al.* report a robotic research system ("*Adam*"), which is capable of carrying out lab experiments on the growth of yeast strains, analyse the data and form research hypotheses from it [143]. Since then, many developments have been published in regard to the acceleration and automation of materials research in the fields of pharmaceuticals, thinfilms, photocatalysts and others [144–155]. The technologies utilized to achieve this can be broadly summarized in three categories: *high-throughput experimentation*, *robotics* and *machine learning*.

A common denominator of all of the systems described in recent literature is that the experiments they carry out are extremely simple. As of today, the full automation of complex, multi-step synthesis and characterization workflows reliably still poses a big obstacle in this field of research.

The system described in Chapter 5 attempts to combine all three technologies to

Table 2.4. List of representative non-noble metal-based electrocatalysts for the alkaline OER at room temperature (η_{10} = overpotential at 10 mA cm⁻², RT = room temperature, C_{dl} = double layer capacitance).

Catalyst	Electrolyte	η_{10} [mV]	Tafel slope [mV dec ⁻¹]	C_{dl} [mF cm ⁻²]	Stability at RT	Ref.
Oxides						
CoO _x /BNG	0.1 M KOH	295	57	-	-	[82]
Co ₃ O ₄	1 M KOH	266	76	-	8 h at 1 mA cm ⁻²	[125]
Fe-NiO	1 M KOH	206	~ 49	~ 81	-	[83]
NiCo ₂ O ₄	1 M KOH	365	292	-	3 h at η = 780 mV	[126]
Peroxsites						
La _{0.9} Co _{0.1} NiO ₃	1 M KOH	270	45	~ 11	48 h at 1.6 V vs. RHE	[89]
La(CrMnFeCoNi)O ₃	1 M KOH	325	~ 51	~ 0.4	50 h at 10 mA cm ⁻²	[90]
Ba _{0.5} Str _{0.5} Co _{0.8} Fe _{0.2} O _{3-δ}	1 M KOH	280	~ 103	6	100 h at η 0.3 V	[91]
Str _{0.95} Co _{0.8} Fe _{0.2} O _{3-δ}	0.1 M KOH	370	49	15.5	-	[92]
PtBa _{0.5} Str _{0.5} Co _{1.55} Fe _{0.45} O _{5-δ}	1 M KOH	290	69	42	~ 2000 h at 100 mA cm ⁻²	[93]
Sulfides						
ZN-Co-S NN	1 M KOH	320	55	~ 10	10 h at 1.9 V vs. RHE	[127]
Co ₉ S ₈ HMs	1 M KOH	420	113	-	4% degrdn./400 CV cycles/5 mV s ⁻¹	[128]
CuCo ₂ S ₄ nanosheets	1 M KOH	310	86	-	12 h at 10 mA cm ⁻²	[129]
FeNiS ₂ NSS	0.1 M KOH	310	46	-	10 h at 1.7 V vs. RHE	[130]
Phosphides						
NiFeP	1 M KOH	233	42.5	-	30 h at 10 mA cm ⁻²	[131]
CoP nanowires	1 M KOH	248	78	-	1000 h at 20 mA cm ⁻²	[132]
NiCoP/rGO	1 M KOH	270	65.7	-	18 h at 20 mA cm ⁻²	[133]
Fe _{1.1} Mn _{0.9} P nanorod	1 M KOH	440	39	-	9% degrdn./20h/1.58 V vs. RHE	[134]
Hydroxides						
CoFe-LDH/rGO	0.1 M KOH	396	43	36.1	10 h at 5 mA cm ⁻²	[135]
NiCo-LDH	0.1 M KOH	290	113	-	-	[136]
Ni _{0.75} Fe _{0.25} LDH	1 M KOH	347	64	~ 0.2	> 18 h at 10 mA cm ⁻²	[137]
Fe ³⁺ -Ni _{0.66} Fe _{0.34} LDH (Fe ²⁺ ·Fe ³⁺ ~ 1:1)	1 M KOH	195	40.3	-	-	[123]
Ni _{0.75} V _{0.25} LDH	1 M KOH	318	50	~ 0.3	> 24 h at 10 mA cm ⁻²	[137]
NiFeMn LDH	1 M KOH	270	47	-	15 h at 1.54 V vs. RHE	[138]
Co _{0.8} V _{0.2} OOH	1 M KOH	190	39.6	61.8	100 h at 10 mA cm ⁻²	[139]
Co _{0.8} Zn _{0.2} OOH	1 M KOH	235	35.7	-	40 h at 20 mA cm ⁻²	[140]
Ni _{0.7} Fe _{0.3} OOH	1 M KOH	200	39	~ 3.1	> 100 h at 350 mA cm ⁻²	[141]

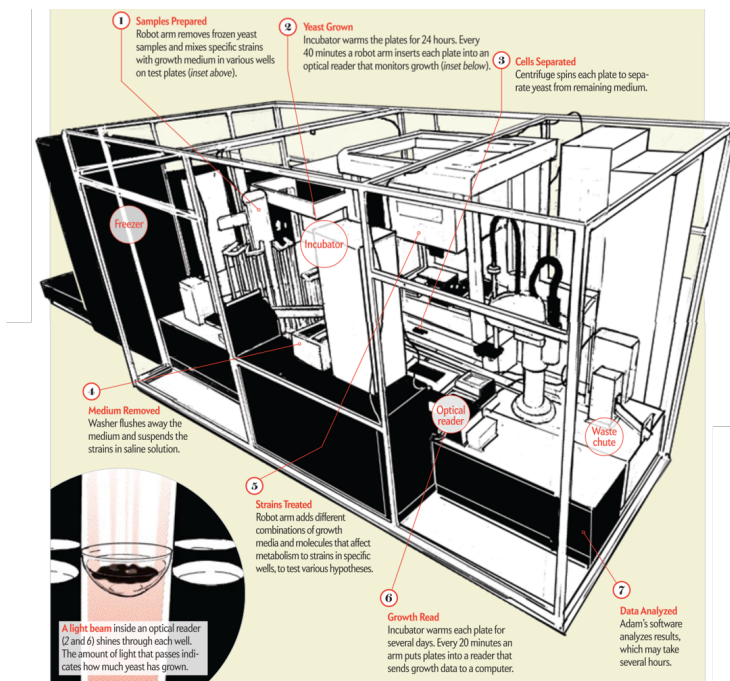


Figure 2.8. Autonomous robotic system for the investigation of yeast growth as described in [143]. Adapted from [144]

automate the search for multi-metal hydroxides as highly active catalysts for the OER. Detailed information about the experimental equipment used for this task can be found in Section 3.2.

2.3.1 High-throughput experimentation

High-throughput Experimentation (HTE) describes the extensive parallelisation of experimental workflows in order to accelerate the systematic assessment of large phase spaces. This can refer to the pure synthesis of material compositions, its testing or characterization, or the entire experimental process [156], including experimental planning and automated data analysis. HTE is a standard procedure in pharmaceutical research [157], and has also been applied to other fields of materials research [158] and in particular to heterogeneous catalysis [156, 159, 160].

One example for HTE published in 2014, Gerken *et al.* presents a study in which 3500 compositions of trimetallic metal oxides were tested for alkaline OER catalysis

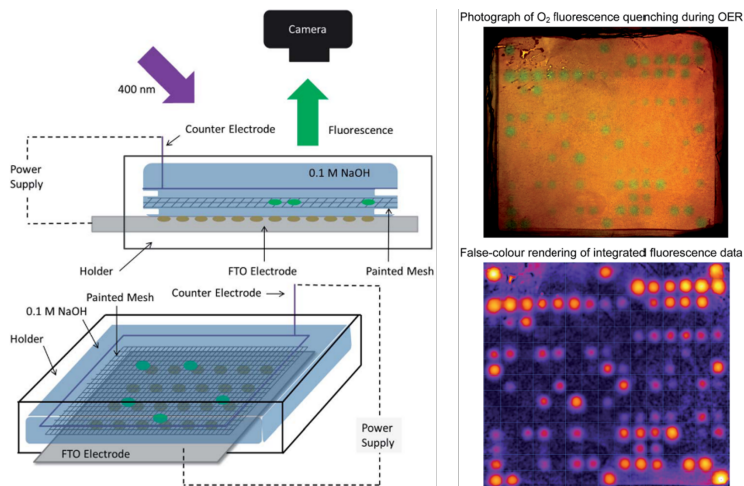


Figure 2.9. Batch screening of alkaline OER catalysts by means of laser-induced fluorescence of a stainless steel mesh coated with oxygen-sensitive paint. Adapted from [145]

by means of batch synthesis and testing, in which 210 combinations are investigated in parallel (see Figure 2.9) [145].

15×14 arrays of catalyst compositions ($A_xB_yC_zO_q$) with 20 % increments of various metals (Mg, Al, Ca, Ti–Ga, Sr, Mo, Ba, Ce, W, Bi) are prepared by drop-casting precursor solutions with a liquid-handling robot onto an fluorine-doped tin oxide (FTO) coated glass plate and subsequent calcination. The array is then manually placed in an electrolyte bath (0.1M NaOH) and operated as the anode. A defocused 400 nm laser makes the amount of evolved oxygen visible by means of a stainless steel mesh coated with fluorescent, oxygen-sensitive paint. The figure of merit (OER activity) is measured by detecting the intensity of fluorescent light emitted from the respective position in the array.

While this concept is not fully autonomous, it achieves very high throughput by means of the high degree of parallelization. This however comes at the cost of indirect measurement and the uncertainties associated with the data analysis and interpretation. The phase space is screened via a linear grid search, with pre-defined compositions.

2.3.2 Robotics

Robotics are an integral part of many lab automation concepts, since it allows to conduct physical experiments without the need for a human researcher, and provide

superior speed and accuracy especially for simple, repetitive tasks such as liquid dispensing or positioning of solid samples.

The term "robot" encompasses very different concepts, but generally describes computer-controlled systems that can perform complex series of tasks automatically. In the following section, several types of robotic systems for lab automation reported in recent literature are introduced. Each concept has its own advantages and disadvantages and as of now, research on autonomous materials research has not converged towards one specific approach. It should be noted that obviously combinations of these concepts are possible and some of the examples given fall in more than one category. For the sake of simplicity, these platforms are listed in the category that is most exemplary for them.

Liquid-handling platforms

A commonly found approach is the use of purely liquid-handling platforms. Typically, precursor liquids are accessed with an array of pumps and moved between reactors and test equipment [149,161]. In the system presented by Dave *et al.* (see f.e. Figure 2.10), battery electrolyte formulations are tested in terms of their electrochemical

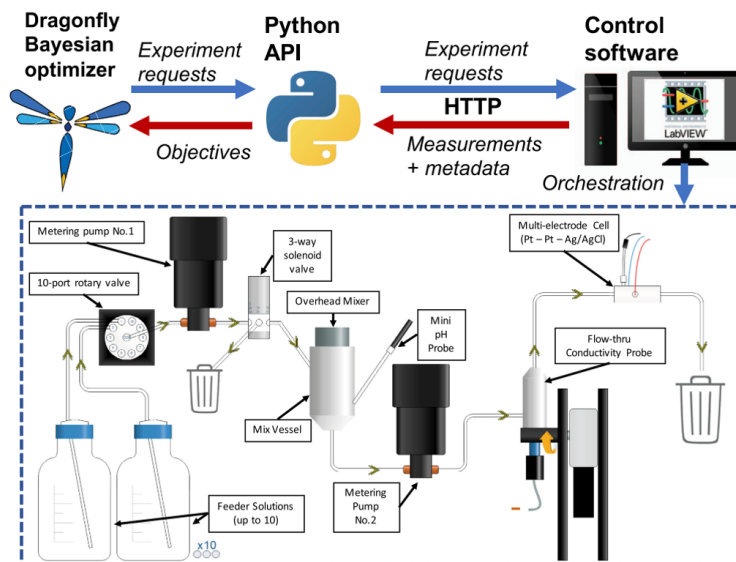


Figure 2.10. Liquid handling organic synthesis robot for autonomous reactivity prediction. Adapted from [149]

stability. The authors stress that the combination of precise and repeatable robotic testing with machine learning optimization (here: Dragonfly Algorithm [162]) allowed them to find an optimum electrolyte composition that the human researcher arguably might have missed.

The advantage of these systems is the reduced technical complexity compared to other types of robots. The reactants and products can be completely secluded from their environment, which mitigates problems with contamination, reactions of precursors with ambient air or issues with corrosion due to their evaporation. Conversely, since these systems lack the ability to handle solid samples between synthesis and test stations, their use cases are somewhat limited in comparison to other approaches.

Gantry-type robots

Gantry type robots can, on a lab scale, be based on modified, commercially available 3D printers. These are compact in size and already come equipped with many capabilities that are useful for conducting lab experiments such as a robotic "arm" capable of moving in a 3-dimensional space, USB and internet connectivity or web cams for remote monitoring. Kitson *et al.* use a modified Prusa i3 (see Figure 2.11) in 2016 to automate ibuprofen synthesis [163]. Compared to many pieces of equipment designed for lab use, consumer-grade 3D-printers are available at very low cost, making lab

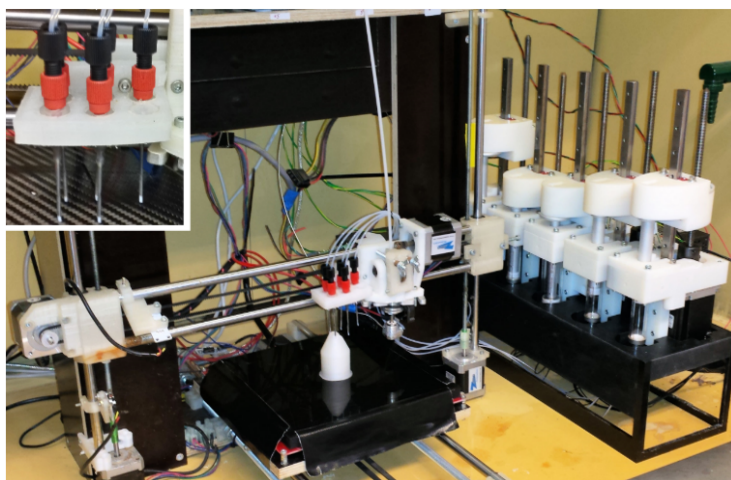


Figure 2.11. Modified 3D-printer for the automated synthesis of ibuprofen. Adapted from [163]

automation potentially accessible to more researchers.

Multi-axis robotic arms

Multi-axis robotic arms are somewhat similar to gantry type robots, in that they are stationary and relatively compact, while allowing to move and manipulate solid objects like vials, samples, or tools. MacLeod *et al.* use a North Robotics N9 platform to realise a autonomous thin-film characterization and optimization experiment (see Figure 2.12) [154]. Samples are fabricated by pipetting a precursor ink of varying composition onto a glass substrate and transferring it to a custom annealing oven. Subsequently, optical images are recorded and ultraviolet–visible– near-infrared spectra and electrical conductivity measurements are performed on the sample via customized equipment. From this data, a pseudo hole mobility value is calculated as the figure of merit (FoM). An optimization algorithm is then used to design the following ink composition such that the FoM is maximized.

As this experimental setup illustrates, the ability to handle solid objects extends the applicability of robotic systems to more complex experimental workflows. These systems however come at a much higher cost than the aforementioned consumer-grade 3D-printers or systems that are restricted to liquid handling. Another factor to consider is that the custom tools and equipment that are often necessary to carry out experiments with this type of system also increase cost, complexity and affect reliability (see also Section 5.3).

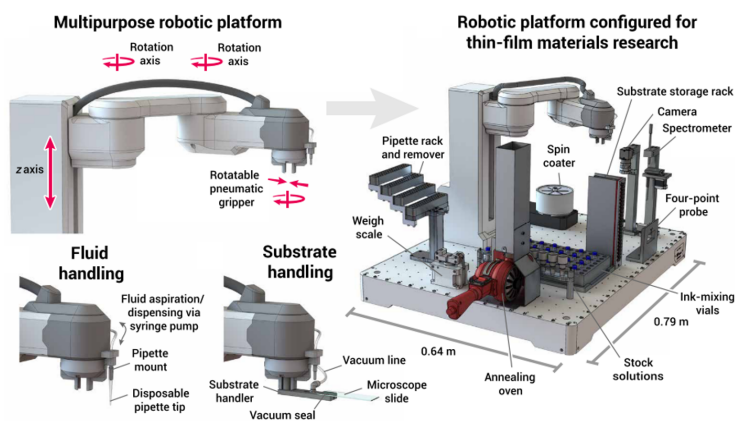


Figure 2.12. Thin-film characterization and optimization by means of a multi-axis robotic arm. Adapted from [154]

The specific robotic platform is the same as in our project and described in more detail in the corresponding manuscript draft in Chapter 5.

Free-roaming multi-axis platforms



Figure 2.13. Free-roaming multi-axis robotic platform for autonomous HER photocatalyst optimization. Adapted from [155]

All the aforementioned systems share a key characteristic: the basis of the concept is the automation of the instrumentation used to conduct the experiment. This comes with both benefits and drawbacks: synthesis, testing and characterization equipment is designed and optimized for a specific use case and as a consequence can be smaller, faster or more accurate than off the shelf counterparts. The entire experimentation system usually has a comparatively small footprint (our setup as well as many oth-

ers fit into a regular ventilated fume hood). On the other hand, this also means that it is usually designed to automate one very specific experiment and an adaptation of new characterization methods, or even completely new experiments, is not a straightforward possibility. Additionally, these systems often require specific laboratory infrastructure (pressurized gases, ventilation) to be available. For safety reasons, f.e. our own robotic platform must only be operated inside a closed fume hood, since it has no means to avoid collisions if a person would come into its range of motion. Burger *et al.* address these issues by turning the approach upside down: using a multi-axis, mobile robot platform that can freely move inside a regular laboratory, they "*automate the researcher rather than the instruments*" (see Figure 2.13) [155]. Their system operates mostly unmodified commercial instruments, such as a gas chromatograph and a solid dispensing station, to conduct experiments in a 10-dimensional parameter space, supported once again by a bayesian optimization algorithm. The object was to find stable, bio derived hole scavengers for photocatalytic HER with high efficiencies. Within a run time of eight days, they manage to conduct 688 experiments and identify formulations with six times higher activity. The researchers argue that their modular approach of a free-roaming robot platform potentially can be applied to a wide range of other research problems as well.

2.3.3 Machine Learning

Machine learning (ML), a subfield of artificial intelligence, has revolutionized various industries by providing powerful tools to extract patterns, make predictions, and optimize processes from vast data sets. In recent years, its application in the chemical sciences has gained significant momentum, fundamentally influencing how chemical compounds and processes are discovered and utilized.

One of the most prominent applications of ML in chemistry is predictive modeling of material properties. By training models on known chemical structures and their associated properties, machine learning algorithms can predict a wide range of material characteristics, including solubility, toxicity, stability, and reactivity. These predictions are invaluable in drug discovery, materials science, and environmental research, guiding the selection of promising compounds for further investigation. Beyond that, ML techniques like bayesian optimization also help to streamline experimental screening approaches and allow to find optima in vast chemical spaces efficiently by reducing the necessary number of experiments drastically in comparison to a regular grid

search. This does not only accelerate innovation, but also contributes to sustainable solutions by identifying environmentally friendly alternatives.

Ever more data is generated in any field of research as time moves on, and ML provides viable tools to extract information from this data. Consequently, many reports were published on the utilization of ML in material development in recent years, for example on prediction modelling to optimize organic synthesis [164], or research on alloys [165], batteries [166], electro- and photocatalysts [167].

The work presented in this thesis uses bayesian optimization algorithms in two different instances to accelerate the optimization of material properties. In Chapter 5, a closed loop screening platform for multi metal hydroxide OER catalysts is designed, using the Dragonfly algorithm [162] to optimize the sample composition to increase OER activity. In Chapter 6, a human-in-the-loop approach is applied to the widely used Gaussian Process Upper Confidence Bound (GP-UCB) algorithm [168] to find optimal synthesis parameters for high surface area Ni electrodes for the alkaline HER. In both cases, the optimization approach falls in the category of reinforced learning, in which measured data is returned to the ML algorithm after each experimental iteration to update the prediction model.

For the implementation of the ML optimisation, existing Python libraries were integrated into the experimental workflow. The development of the algorithms is not part of the present work.

CHAPTER 3

Experimental test setups

For the electrochemical experiments conducted in this thesis, two different setups have been used: a planar near-zero-gap cell and an automated test setup, which comprises the North Robotics N9 platform, an electrochemical test cell, a custom sample and vial holder, a stepped gripper tool and two pump assemblies. These setups are described in more detail in the following section.

3.1 PEEK planar near-zero-gap cell

For the electrochemical test described in Chapters 4 and 6 a simple planar near-zero-gap cell with inner dimensions of ca. 35 mm \times 26 mm \times 25 mm which is machine from solid PEEK was used. The working electrode (WE) is pressed against a separator (Zirfon PERL UTP 500) by means of an M3 PEEK screw, and connected via a piece of Ni wire or perforated plate that is place in between. The counter electrode (CE), a ca. 30 mm \times 35 mm perforated Ni plate, is fixed in place by a recess ca. 2 mm away from the separator, such that a Gaskatel MiniHydroflex reversible hydrogen reference electrode (RHE) can be placed in between. The connection to the potentiostat is established via crocodile clamps (see Figure 3.1 and B.1).

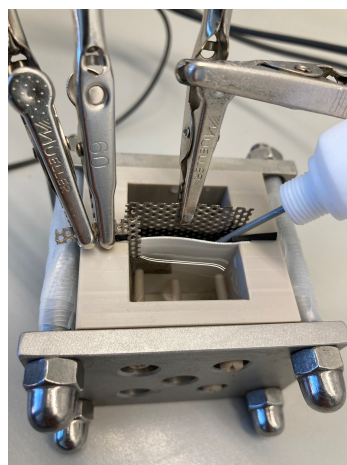


Figure 3.1. Planar near-zero-gap cell.

3.2 Automated test setup

3.2.1 North Robotics N9 platform

The system is based on the N9 robotic platform from North Robotics (Victoria, Canada). It consists of an aluminium table base, a robotic arm including its C9 controller unit, a pneumatic vial clamp and a liquid dispensing carousel. The table

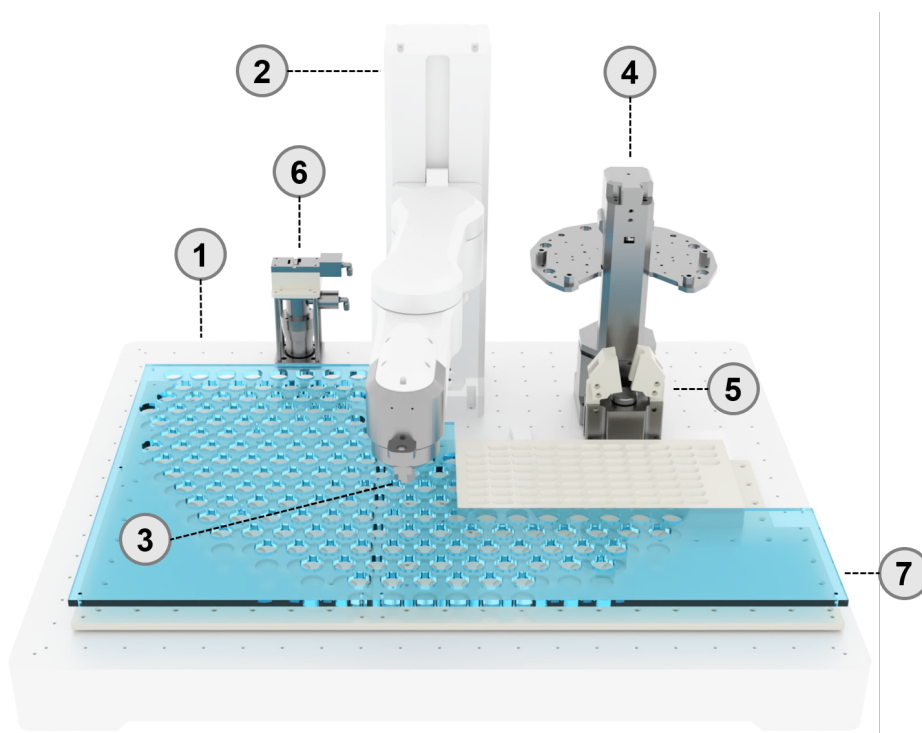


Figure 3.2. 3D rendering of N9 platform consisting of an aluminium table base (1), robotic arm (2) including gripper tool (3), liquid dispensing carousel (4) and vial clamp (5). Electrochemical test cell (6) and sample and vial holder (7) are custom parts developed in house. C9 controller not displayed.

base has outer dimensions of 814 mm * 664 mm, under mounts for the C9 controller and other auxiliary equipment and a rectangular 37.5 mm grid of M3 tapped holes on the surface. The 4-axis robotic arm features stepping motors to move in the horizontal plane (shoulder and elbow) and along the vertical z-axis. Additionally, there

is a pneumatically actuated gripper tool at the end of the robotic arm, which can be rotated at up to 1500 rpm.

3.2.2 Electrochemical test cell

The electrochemical test for the autonomous optimization of multi metal hydroxides as described in Chapter 5 were carried out in a custom made, beaker-type cell shown in Figure 3.3. The main body of the cell was machined from Polytetrafluoroethylene (PTFE) and consists of a base, a lid and a pneumatic piston attachment. The base holds a volume of ca. 12 ml when filled to the brim, and has a vertical outlet at the bottom with 4 mm diameter connected to the liquid waste container. The base is designed such that the electrolyte is not in physical contact with any metal parts other than the WE and CE, and the floor of the base is angled towards the outlet to avoid dead volume when flushing the cell. Behind the CE position, a safety overflow is implemented which is connected separately to

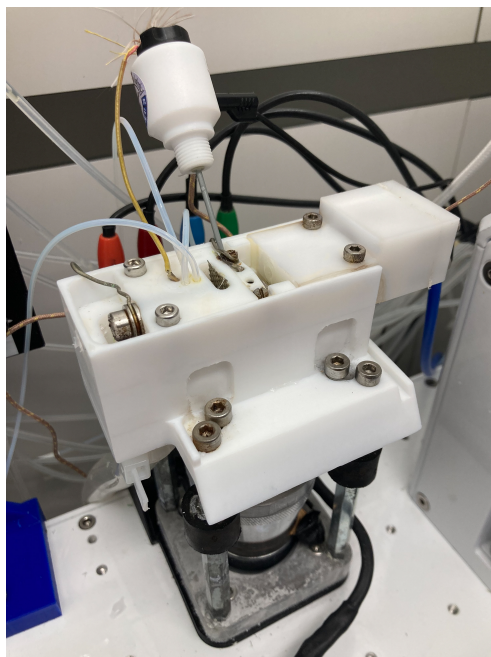


Figure 3.3. Beaker-type electrochemical test cell for the automated test setup.

the liquid waste container. The cell lid is mounted with two M3 screws in a recess as a secondary safety measure to avoid overflow, and has three inlets for 1.6 mm (outer diameter) tubes (1 M HCl, 1 M KOH, deionized water), a thermocouple shielded with PTFE shrink tube, a 10 mm × 3.2 mm opening for the CE and a mounting and connection mechanism for the WE current collector. The CE, a perforated Ni plate is fixated with a M4 screw. The WE current collector, a 20 mm × 10 mm platinum plate, is held in place with a narrow PTFE plate screwed one from the top with two M2 screws. The CE is bent such that it sits parallel with 2 mm distance to the WE. All screws are Ni plated steel screws. The reference electrode (RE), a

standard Gaskatel MiniHydroflex RHE, is placed diagonally at a 45° angle between WE and CE, with the tip located in the edge of the base, slightly offset with respect to the WE. WE and CE are connected to a gold plated banana plug terminal (separate plugs for current carrying and voltage sensing electrodes) with 1 mm Ni wire, to which the Gamry Reference 600 potentiostat is connected. The RE is connected directly to the potentiostat. The thermocouple is placed behind the CE such that it is submerged in the electrolyte during testing and connected to an Arduino Uno, which also records ambient temperature and humidity in the fume hood. The piston

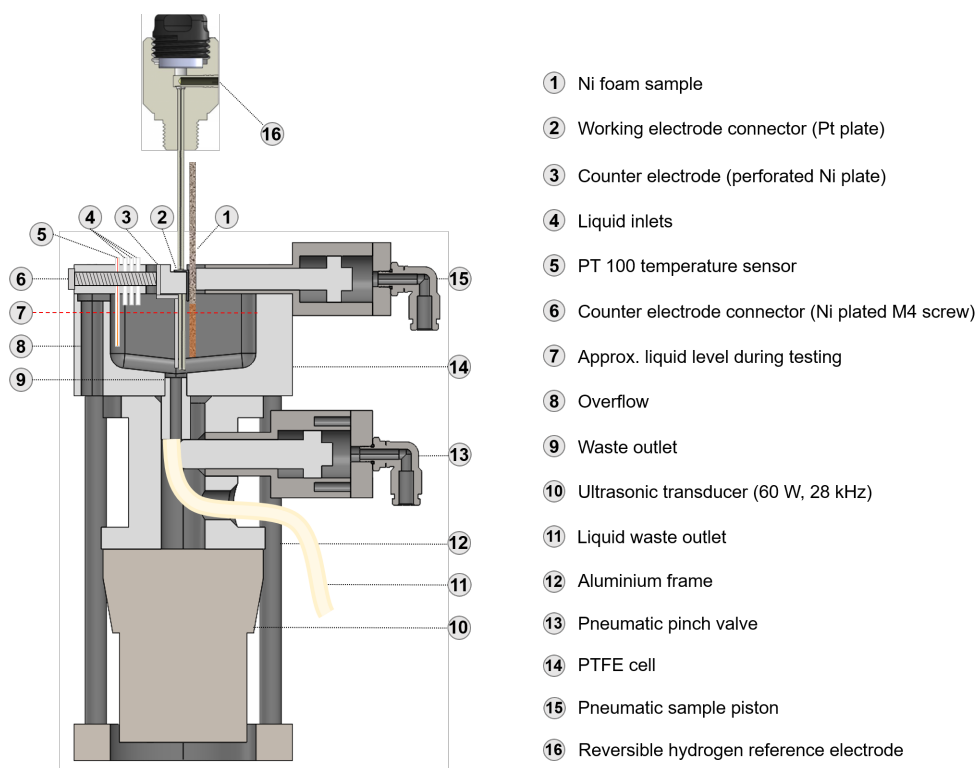


Figure 3.4. Cross-section of the electrochemical test cell.

attachment is mounted opposite to the lid and leaves a $5 \text{ mm} \times 28 \text{ mm}$ opening to insert the sample/WE. A PTFE piston (6 mm diameter) is actuated pneumatically with ca. 4 bar to press the WE against the platinum plate and retracted with a steel spring (not shown).

Below the main body of the cell, an cylindrical adapter machined from aluminium is

mounted with four M4 screws which houses a second piston attachment (8 mm PTFE piston) to act as a pinch valve for the cell outlet. Attached below the adapted is an ultrasonic horn (28 kHz, 60 W) via four M4 screws. The entire assembly is mounted onto an aluminium frame via four rubber vibration dampeners. The pneumatic pistons are connected to the labs compressed air supply by 6 mm push-in pneumatic fittings.

3.2.3 Sample and vial holder

The sample holder was machined from solid PTFE and consists of two parts to allow easier cleaning (see Figure 3.5). The top part has 82 identical $13.5\text{ mm} \times 2.5\text{ mm}$ cutouts for Ni foam substrates with dimensions $50\text{ mm} \times 10\text{ mm} \times 1.6\text{ mm}$. Tapering of the cutout opening is used to compensate for minor bends or incorrect positioning of the Ni foams. The cutouts are arranged in a linear grid and as close together

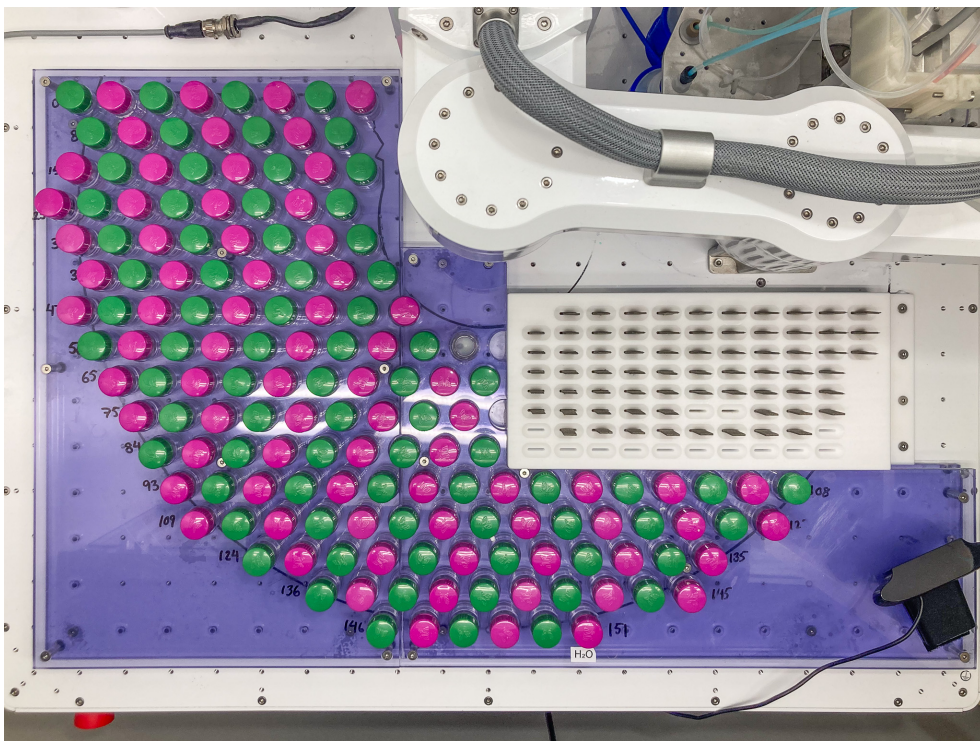


Figure 3.5. Sample and vial holder assembly.

as the dimensions of the robot gripper allow (see also Figures B.4 and B.5). A barbed fitting for 6 mm tubes is placed in the back of the sample holder top part, to which a membrane pump can be attached to create a drying air draft over the sample surface. For that, the top part is placed in a recess in the base, which leaves a 2 mm gap between both parts. The vial holder was cut from two plates of 8 mm acrylic glass offset by 20 mm with metal spacers. 152 circular 24 mm cutouts are arranged in a half-offset pattern along the operating range of the robotic arm to maximize space utilization. The distance between cutouts is 32 mm (center to center), which is the minimal distance achievable based on the diameter of the opened gripper tool. The vials used are 27 mm \times 40 mm screw cap glass vials (see Figure B.6). One of the vials is fixed in place with epoxy glue to act as a cap holder whenever another vial is uncapped to free up the gripper tool.

3.2.4 Gripper

The gripper used to handle vials and samples was machined from aluminium (see Figure 3.6). It was dimensioned such that the lower part can be used to grip and uncap screw cap vials with a cap diameter of 22 mm and the top, flat part to grip Ni foam sample. Exact dimensions can be found in the appendix (see Figure B.5).

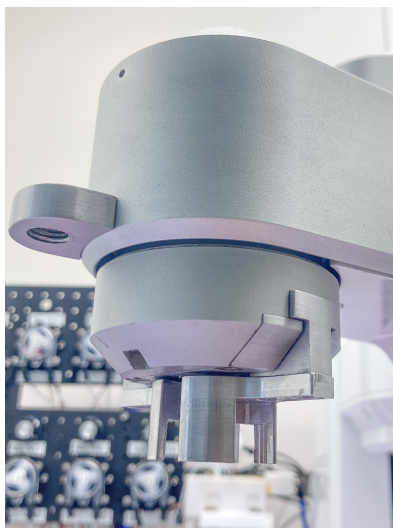
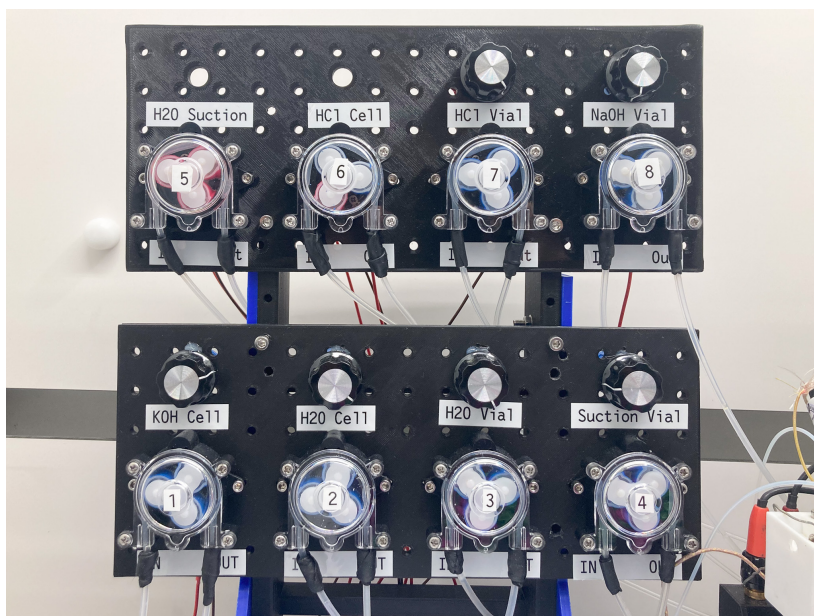


Figure 3.6. Stepped gripper machined from Aluminium.

3.2.5 Pump assemblies

In total, 17 liquid pumps were implemented in the experimental setup. 8 Tricontinent C3000 syringe pumps were used to dispense metal nitrate solutions (Fe, Cr, Al, Co, Ni, Mn, Zn, Cu) with 1 ml and 1.5 ml syringe volume. The pumps were connected with PTFE tubing (1/8" outer Ø, 3/32" inner Ø) to 3 liter polypropylene bottle chemical reservoirs. For the outlets, smaller PTFE tubing (1/16" outer Ø, 1/32" inner Ø) was used to avoid the formation of large droplets, which were connected to the dispensing carousel of the North Robotics N9 platform. All other liquids (KOH, $2 \times \text{H}_2\text{O}$, $2 \times \text{HCl}$, NaOH) were dispensed with generic 12 V peristaltic pumps connected to the chemical reservoir and outlet via a single piece of silicone tubing each (3 mm outer Ø, 1 mm inner Ø). Two additional peristaltic pumps were installed to empty full vials. The flow rate of the peristaltic pumps were calibrated with 500 Ohm potentiometers to the lowest value with which they would reliably pump, which typically was ca. 1 ml s^{-1} . For the volumes needed, this resulted in a relative error of ca. 1 %.

It should be noted that the syringe pumps did not work without major issues throughout the project. The pumps are controlled with Python code, since complex sequences of actions are necessary to pump liquids. After successfully carrying out a pump sequence, the script expects a return value sent from the pumps. This procedure was very prone to failure which caused the script to abort and had to be fixed with a cumbersome workaround. Additionally, these pumps had problems with air leaking into the tubing and dripping from the outlets. The peristaltic pumps on the other hand could only be controlled by switching them on and off via a relay, and the total volume dispensed was then defined by the delay time in between. This proved to be the much more reliable system, even though the cost per pump was lower by a factor of ~ 100 .



(a) Peristaltic pumps



(b) Syringe pumps

Figure 3.7. Pump assemblies used in autonomous experimentation setup.

CHAPTER 4

Screening Study of transition metal hydroxides as OER catalysts for conventional alkaline and seawater electrolysis

4.1 Introduction

The following work was carried out at the start of the PhD project to investigate the activity of different binary and ternary metal (oxy) hydroxide compositions with respect to the alkaline OER. For this, a rapid co-precipitation method was employed

to obtain Ni based catalyst layers directly on a Ni foam substrate, doped with either one or two additional elements comprised from a total of 8 transition metals (Fe, Cr, Al, Co, Ni, Mn, Zn, Cu). While a lot of literature already exists on NiFe LDH doped with one or more elements, comparative studies in which a wide range of these dopants is investigated under equal conditions remains missing. Similarly, the suitability of these metal hydroxides for seawater electrolysis is still largely unexplored. The objective of this initial study was therefore to address this gap, and assess which compositions are worthwhile to look into in greater detail. While most compositions had comparable OER activity for both electrolytes, some samples (f.e containing Mn or Cr) showed a significant difference, which would be a suitable subject for further investigations.

Over the course of the study however it became clear that the synthesis route comes with certain specific advantages and disadvantages. The reproducibility of results was surprisingly high given the simple procedure, and samples analysed with XRD and EDX showed that the dopants were well dispersed in the deposition layer. Layered double hydroxide was identified as the main crystal phase, with no substantial amount of secondary phases ¹. On the other hand, the method gives no straightforward control over the exact composition, meaning that a certain metal composition in the precursors did not necessarily yield a sample with the same metal composition. This makes it unfeasible for an in depth analytical study on the influence of sample and electrolyte composition on the OER activity, but especially suitable for the project on autonomous high-throughput screening that is described in Chapter 5. In this case, the primary objective is the discovery of optimal compositions within a large phase space. The "real" composition of any given sample with high performance can then always be found by means of additional manual investigations, f.e. XPS analysis. The extremely fast synthesis time seemed to be preferable over increased knowledge on the sample composition for this use case.

From this point onward, the high-throughput study was prioritized over more detailed analyses of the dopant effects. The following manuscript should therefore also be seen in the context of a pre-study on the feasibility of the described screening approach for autonomous high-throughput screening.

The experimental work and writing of the manuscript for the study was carried out

¹On that matter it should be noted that the samples investigated in terms of crystal structure were doped with a 3+ cation, enabling crystallization in the LDH phase. This is not necessarily the case for all compositions.

in whole by the author of this thesis under the supervision of Prof. Ragnar Kiebach and Mikkel R. Kraglund.

4.2 Manuscript draft

Screening Study of transition metal hydroxides as oxygen evolution reaction catalysts for conventional alkaline and seawater electrolysis

Enzo Raffaele Moretti¹, Mikkel Rykær Kraglund¹, and Ragnar Kiebach¹

¹Department of Energy Conversion and Storage, Technical University of Denmark, Anker Engelunds Vej, Building 301, 2800 Lyngby, Denmark

ABSTRACT

In this work, we investigate a series of Ni based transition metal hydroxides with respect to their oxygen evolution reaction (OER) activity for the use in alkaline and seawater electrolysis. By means of a co-precipitation method at room temperature, we deposit single metal, binary and tertiary hydroxide compounds, composed from eight different metals (Ni, Fe, Cr, Co, Al, Mn, Zn, Cu), directly onto a Ni foam substrate. A comparison of their oxygen evolution reaction (OER) performance both in conventional, 1 M KOH as well as in seawater substitute (1 M KOH + 0.5 M NaCl) shows no substantial difference between the two electrolytes. In good agreement with existing literature, NiFe based compounds generally deliver the best OER performance. Addition of Cr or Co results in further improvement over the binary NiFe sample, reaching an overpotential of 247 mV at 10 mA cm⁻² and 299 mV at 100 mA cm⁻², far below the thermodynamic onset potential of the chlorine evolution reaction. Several Fe free compounds (Al, Co, Mn) achieve substantial improvements over Ni foam, but cannot reach the performance of Fe samples. SEM images and XRD measurements reveal that the deposited catalyst layer is comprised of layered double hydroxides (LDH), while FTIR spectra indicate that the intercalated anion is CO_3^{2-} . XPS shows that the Ni to 3+ dopant ratio is 2:1, regardless of whether one or two dopants are used.

Keywords: seawater electrolysis, catalysis, alkaline electrolysis

1 INTRODUCTION

The intermittent nature of renewable energy sources holds several challenges: Energy must not only be generated but also stored, transported and converted while remaining economically competitive [1]. Hydrogen can be a vital part of the solution to this chal-

lenge. Renewable energy from wind or solar power can be used to generate hydrogen through water electrolysis. This hydrogen can subsequently serve as an energy storage buffer for electric grids, a clean fuel source, or as a precursor in the chemical industry [2, 3, 4].

In recent years, a significant scientific effort has been dedicated to improving the performance and efficiency of different water electrolysis technologies, such as alkaline (AEC) [5], proton exchange membrane (PEMEC) [6], anion exchange membrane (AEMWE) [7] and high temperature solid oxide electrolysis (SOEC) [8]. Nonetheless, all these approaches require pure water feeds, thereby mandating purification elements in the balance of plant. In many coastal zones that stand out as particular promising regions in terms of solar and wind energy resources [9], fresh water is scarce, whereas seawater is abundantly accessible in these areas. The composition of seawater can vary depending on location, depth, and other factors, but usually includes organic compounds, sediment particles and various salts. While all of these impurities need to be considered, especially the evolution of poisonous and corrosive chlorine species from dissolved NaCl poses a big issue for water electrolysis and makes additional purification steps imperative. While there are several established technologies for the desalination of seawater like reverse osmosis, nanofiltration or several types of distillation [10], this requirement escalates costs, introduces complexity, and enlarges the footprint of the electrolyzer system [11]. Using seawater directly as an electrolyte feed, without desalination holds the potential to make seawater electrolysis more cost-effective. Simultaneously, the reduced technical complexity and smaller footprint could potentially expand the scope of applications of such systems.

In spite of these potential advantages, only a limited number of investigations have been reported on catalyst materials suitable for use in seawater conditions. One proposed pathway to design a catalyst capable of suppressing the chlorine evolution reaction (CIER) in seawater is the application of an ion selective blocking layer [12], which physically hinders the chlorine from adsorbing on the active surface sites of the catalyst. While it is feasible to achieve relatively stable catalysts through this approach, effectively preventing chlorine evolution, it introduces an additional resistance to the electrochemical system, which leads to increased overpotentials and consequently efficiency losses. Given that efficiency plays a pivotal role in achieving commercial success in this context, it remains doubtful whether this technology will ever reach the state of economic feasibility.

Another approach to address the issue of corrosive chlorine species might however not be imperative. At pH 14, the thermodynamic equilibrium potential of the hypochlorite (OCl^-) formation lies ca. 480 mV above that of the OER ($E_{OER}^0 = 1.229$ V, $E_{OCl}^0 = 1.72$

V vs. RHE) [13]. If a catalyst can deliver sufficient current densities ($> 1 \text{ A cm}^{-2}$) within this potential window, hypochlorite formation is thermodynamically inhibited and an active suppression is not needed. In this case, any catalyst that is viable for conventional alkaline electrolysis is also a candidate for use with seawater (i.e. salinated) electrolyte. In 2020, Dresp *et al.* used an anion exchange membrane electrolyzer to feed seawater only to the cathode, while the anode is circulated with 0.5 M KOH. They show that under these conditions, the Cl^- crossover to the anode is kept low and the hypochlorite formation can be prevented even at higher potentials due to the intrinsic selectivity towards the OER of the used NiFe layered double hydroxide (LDH) catalyst. These materials are known to have exceptional catalytic activity with respect to the alkaline OER. Additional elements (Cr, Al, Mn, ...) can potentially further improve the performance as numerous studies in recent years have shown, but due to varying synthesis and testing conditions and a vast pool of suitable dopants a clear picture regarding their effect on the OER activity remains missing[14, 15, 16, 17, 18, 19, 20, 21].

The focus of this study lies in the exploration of highly active mixed-metal hydroxides catalysts for the oxygen evolution reaction (OER) in the context of conventional alkaline and seawater splitting. In this study, catalysts were synthesized via a simple co-precipitation process adopted from Li *et al.* [22]. Our investigation encompasses a screening study derived from eight readily available transition metals (Al, Cr, Mn, Fe, Co, Ni, Cu, Zn). The different catalysts were deposited onto a Ni foam substrate by a two-step dip coating process starting from metal nitrate solutions. These precursor solutions are both used individually and mixed in a 1:1 ratio with a second precursor, resulting in a total of 36 compounds. We investigate the effect of different doping metals on the structural properties of the catalyst, as well as on the catalytic activity with respect to the OER, in both conventional alkaline and saline-alkaline electrolytes.

2 MATERIALS AND METHODS

2.1 Materials

KOH (ACS reagent, $\geq 85 \%$), NaOH (ACS reagent, $\geq 85 \%$), Manganese (II) nitrate tetrahydrate (98.5 %), Nickel(II) nitrate hexahydrate (99 %), Iron(III) nitrate nonahydrate (99 %), Cobalt(II) nitrate hexahydrate (99 %), Zinc(II) nitrate hexahydrate (99 %), Chromium(III) nitrate nonahydrate (99 %), Aluminium(III) nitrate nonahydrate (99 %), Copper(II) nitrate hemipentahydrate (99 %), Acetone (98 %), Ethanol (98 %) and HCl (37 wt. %) were supplied by Sigma Aldrich. Ni foam (1.6 mm thickness, 450 μm cell size, 97 % porosity) was supplied by Alantum was used as substrate.

2.2 Sample preparation

For the present study, 36 compositions of transition metal (Al, Cr, Mn, Fe, Co, Ni, Cu, Zn) hydroxide coated Ni foam substrates were synthesized. Initially, 0.8 M single metal nitrate solutions were prepared by dissolving the respective metal nitrate in DI water. The binary metal nitrate solutions were then mixed from the single metal solutions in a 1:1 ratio. The samples are named according to the elements in the precursor solutions, i.e. “Al sample” if the synthesis was carried out using Aluminium nitrate solution or “MnCo sample” if the synthesis was carried out using a mixed Manganese and Cobalt nitrate solution.

The Ni foam substrates were cut with a die cutting tool into 25 mm * 25 mm pieces and sonicated consecutively in a 1:1 acetone and ethanol mixture for 30 min to remove organic residue and in 3 M HCl for 15 min to remove surface oxides. Afterwards the substrates were sonicated in DI water three times to remove all remaining HCl.

The as prepared substrates were then coated with the metal hydroxides by means of a modified version of the dip-coating process described by Li et al. [22]. First, the substrates were dipped in 36 ml of metal nitrate solution for 3 s. To achieve a thin, homogeneous coating layer, excess solution was drained from the pores by lightly pressing one edge of the foam onto a paper cloth for 5 s. Samples were left to dry in the air for 10 min. In a second step, the samples are dipped in 2.5 M NaOH solution for 3 s and left to dry for 5 min again. Following this, the samples were sonicated in DI water and ethanol several times until the cleaning solution remained clear. Subsequently, the samples were dried overnight at 60°C in air. The procedure is illustrated in Figure 1. The mass loading of the deposition layer was checked by means of a Spectroquant

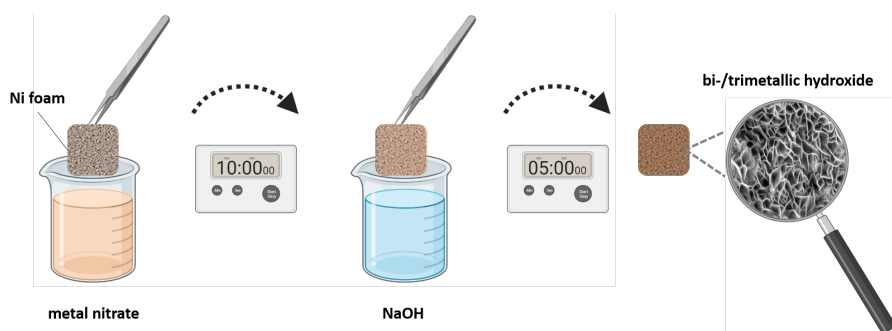


Figure 1. Schematic depiction of the co-precipitation synthesis process.

Move 100 Colorimeter. For this, the deposition layer was dissolved in 0.5 M HCl in an ultrasonic bath for 30 s. Subsequently, the Ni and Fe contents of the resulting solution

were measured. Assuming the molecular formula of the surface layer

$$[M_{1-x}^{2+}M_x^{3+}(OH)_2](A^{n-})_{x/n} * mH_2O \quad (1)$$

Since the metal hydroxide layer dissolves far quicker than the Ni substrate, this allowed for a reasonable estimation of the average mass loading, which was found to be 1.5 - 2.0 mg cm⁻¹.

2.3 Electrochemistry

The electrochemical tests were conducted using a three-electrode setup with a Gamry Reference 600 potentiostat in a planar-type cell with a near zero-gap configuration. Perforated Ni plates with a thickness of $d = 300 \mu\text{m}$ were utilized both as the counter electrode (approximately $31 \text{ mm} * 35 \text{ mm}$) and to connect the working electrode. The OER activity of the connector was determined by performing blank measurements of the cell setup without any test sample. A reversible hydrogen electrode (RHE, Gaskatel Mini HydroFlex) was used as reference electrode (RE). For the separator, ZIRFON PERL UTP 500 ($d = 500 \mu\text{m}$) was selected.

For the initial screening, the originally $25 \text{ mm} * 25 \text{ mm}$ samples were cut down to $10 \text{ mm} * 10 \text{ mm}$ and tested in both 1 M KOH (non-saline) and 1 M KOH + 0.5 M NaCl (saline) electrolyte. For conditioning, the samples underwent a short cyclic voltammetry scan (5 cycles, 20 mV s^{-1} , 0.8 - 1.6 V vs. RHE) for surface conditioning. Overpotential values (η) at 1 mA cm^{-2} and 10 mA cm^{-2} (95 % IR corrected) with respect to the OER were taken from linear sweep voltammetry (LSV) measurements from 1.6 V to 0.8 V vs. RHE at a scan rate of 1 mV s^{-1} . η at 100 mA cm^{-2} is from a subsequent 15 min chronopotentiometric (CP) measurement. Electrochemical impedance spectroscopy (EIS) in the frequency range from 1 Hz - 100 kHz with an amplitude of 10 mV was carried out before and after the testing sequence, the former of which was used to determine the IR.

2.4 Structure and Morphology

SEM images of the samples were taken before and after performing the electrochemical testing by means of a ZEISS Merlin scanning electron microscope (SEM). Energy dispersive x-ray spectroscopy was carried out on a Zeiss EVO MA10 SEM. The elemental composition and oxidation states of the coating surface were investigated using a Thermo Fisher Escalab 250Xi x-ray photoelectron spectrometer (XPS). The composition was obtained from quantitative analysis of the respective 2p spectra. Deconvolution was carried out using a Shirley type background. Attenuated total reflectance Fourier transform infrared (ATR-FTIR) spectra were recorded using PerkinElmer Spectrum

Two FT-IR Spectrometer in the wave number range 550-3500 cm^{-1} . XRD data was obtained with a Malvern PANalytical Aeris powder diffractometer with Bragg-Brentano geometry. The patterns were recorded at 0.5°/min from 5° to 90°. The thin deposition layer achieved with the co-precipitation method and the reduced useful surface area for x-ray diffraction measurements due to the Ni foam substrate made data acquisition challenging. For this reason, the deposited material was scraped off the sample surface mechanically with a scalpel until a sufficient amount of powder was obtained for XRD.

3 RESULTS AND DISCUSSION

Formation mechanism of catalyst layers on Ni foam

After the first synthesis step, the surface of the Ni foam is covered with metal nitrate solution. In the case of Fe nitrate this solution can act as a Lewis acid, which leads to a small amount of dissolution of surface Ni. These Ni ions are then available for precipitation in the second step. For this reason, the deposition layer of many samples can contain Ni, alongside the supplied metal ions from the nitrate solution.

3.1 Electrochemical Screening

An uncoated Ni foam served as a reference in terms of OER activity. The Ni foam was consecutively washed in ethanol and acetone, HCl and water as described previously (2.2). The overpotential at 10 mA cm^{-2} (η_{10}) was chosen as a figure of merit for the electrochemical performance, since the results at higher current densities are increasingly influenced by the properties of the test setup and bubble formation and trapping. To ensure reproducibility, three identical Fe samples were tested and yielded largely similar results, with $\eta_{10} = (255 \pm 3)$ mV.

The heat maps in Figure 2 show η_{10} tested in both 1 M KOH and 1 M KOH + 0.5 M NaCl, used as a seawater substitute, for all compounds as well as for the uncoated Ni foam.

Performance of single cation doped electrodes

Looking at the samples doped with a single cation (plotted diagonally in the matrices in Figure 2) in KOH, Cu, Zn and Mn show essentially unchanged OER activity with respect to the Ni foam (369 mV). A significantly reduced η_{10} is found for Co (317 mV), Al (312 mV) and in particular Fe (255 mV), which is in line with reports in the literature [23, 24, 25, 26]. A similar picture emerges in the case of the saline electrolyte (Fe: 259 mV, Ni foam: 359 mV), although Mn (321 mV) slightly outperforms both Co (325 mV) and Al (340 mV).

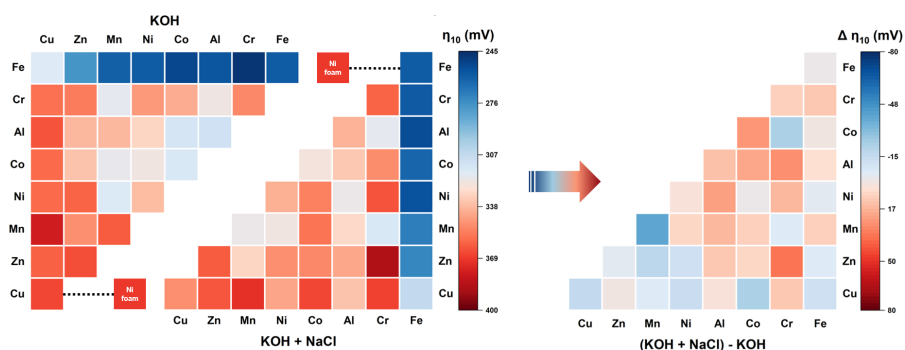


Figure 2. Heatmaps visualizing the overpotential at 10 mA cm^{-2} (η_{10}) of all investigated compounds tested in 1 M KOH and 1 M KOH + 0.5 M NaCl (left). Comparison of the respective overpotential difference between the two electrolytes (right).

Performance of double cation doped electrodes

Considering the entire doping matrix, a large fraction of the compositions show very little improvement or even a reduction in OER activity (MnCu in KOH, ZnCr in KOH + NaCl) compared to the Ni foam reference. Several Fe free samples, particularly those containing Al, Co, Cr and Mn, show improved performance, most with η_{10} in the range of ca. 310-325 mV. In the saline KOH the effect can also be found, but is less pronounced. However, none of them can reach or surpass the samples containing Fe, both in saline and non-saline electrolyte. This is in agreement with the widely reported “Fe-effect” [27, 25, 26]. The only exception to this is FeCu, which shows notably higher η_{10} than all other Fe compounds as well as several Fe free compounds (Al, Co, AlCo, Mn) in KOH. Figure 3a and b show a comparison of the uncoated Ni foam with the well-known NiFe LDH (Fe sample) and the best Fe-free and trimetallic compounds in both electrolytes. Although Fe free samples achieve improvements of ca. 50 mV at 10 mA cm^{-2} over Ni foam, NiFe-LDH still exceed its performance by roughly the same margin. Additional doping of the NiFe-LDH achieves even better results, as Figure 3c shows.

Influence of the electrolyte:

Comparing the results between the two electrolytes, the difference in overpotential ($\Delta \eta_{10}$) is relatively small compared to the effect of doping, with a negligible mean $\Delta \eta_{10}$ of 2.8 mV across the entire matrix. The Mn compound shows largest $\Delta \eta_{10}$ with 40 mV better performance in saline electrolyte, whereas the η_{10} values across the doping matrix span from 247 mV (FeCr) to 387 mV (ZnCr). Generally, less electrochemically active compositions seem to experience an improvement when NaCl is added, whereas the

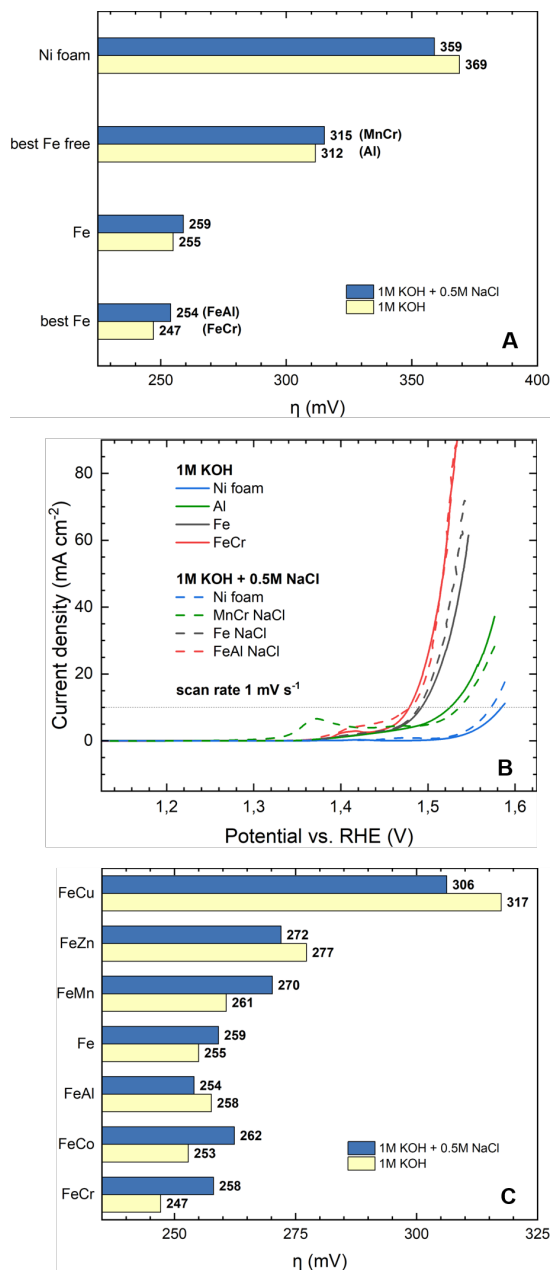


Figure 3. Overview of OER overpotential at 10 mA cm^{-2} of Ni foam, Fe and the best Fe-free and Fe-containing samples in both electrolytes (A) as well as the corresponding anodic LSV scans (B). Comparison of the effect of the dopant on the overpotential of Fe compounds (C).

highly active Fe samples appear to be slightly dampened.

Elemental composition of high-performing catalysts:

Figure 4A shows the elemental composition of electrodes containing Ni, Fe and a third metal determined by XPS analysis. All samples with a M^{3+} dopant (FeCo, FeCr, FeAl) show similar Ni contents between 61 and 64 % compared to the base Fe sample (65%), corresponding to a Ni to M^{3+} ratio of ca. 2:1. This also corresponds to the highest Fe content typically found in NiFe-LDH materials according to literature (Wang2012, Carrasco2019). The ratio with which the two M^{3+} precipitate differs significantly from the stoichiometric ratio of 1:1 and ranges from 16:20 (Fe:Cr) to 6:32 (Fe:Al). As the NiFe sample shows, additional Ni^{2+} supply through the precursor solution does not change the Ni:Fe ratio, presumably since Fe ions are still abundantly available for precipitation at 0.4 M concentration. The addition of Mn results in an unchanged Ni content in the final product as well and yields a Ni:Fe ratio of ca. 3:1. This is an indicator that Mn actually replaces Fe rather than Ni in the compound and thus is present in the hydroxide layer in a 3+ oxidation state. FeZn and FeCu show a different composition than the other samples. Both elements lead to higher M^{2+} :Fe ratio of 3:1, with significantly reduced Ni content.

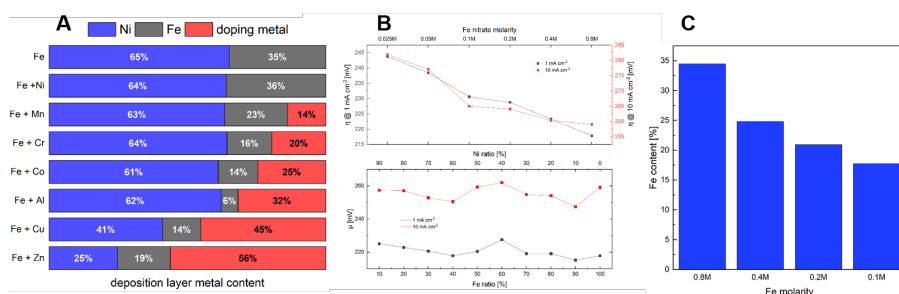


Figure 4. Surface layer composition measured by means of XPS analysis.

Effect of Fe concentration:

The effect of the Fe concentration in the synthesis solution on the OER activity was studied by comparing a series of NiFe samples synthesized with Fe nitrate solutions from 0.025 M to 0.8 M, as well as with mixed Ni and Fe nitrates in different ratios (0-90% Ni) with a total concentration of 0.8 M. The molarity of the NaOH solution was 2.5 M, similar to all other experiments. Interestingly, no significant trend in η is observed when varying Ni and Fe nitrate ratios whereas a linear improvement of the overpotential is observed with increasing molarity, resulting in a 23 mV lower η_{10} when using 0.8 M (as in the screening matrix) instead of 0.025 M Fe nitrate (Figure 4B). This

can be attributed to an increasing Fe content in the deposited NiFe-LDH layer (Figure 4C), that roughly corresponds to 5:1 (0.1 M), 4:1 (0.2 M), 3:1 (0.4 M) and 2:1 (0.8 M) Ni:Fe ratios.

3.2 Structural Characterization

Scanning electron microscopy, as well as the investigation of the crystal structure and oxidation states was performed on the Fe samples by means of XRD, FTIR and XPS. Figure 5A and B show the Ni foam surface after synthesis on the example of the FeCo sample. The coating appears to cover the substrate evenly with only a few, small areas with agglomerated material. EDX elemental maps (Figure 5B overlay) reveal that the metal ions are homogeneously distributed in the deposition layer, suggesting that the co-precipitation process yields Co-doped NiFe-LDH rather than separate phase domains of NiCo and NiFe LDH. Similar results were obtained for other samples, as can be seen in the supplementary information in Figure S1. This underscores the feasibility of using this synthesis method for screening studies of doped NiFe-LDH type materials.

As can be seen in the high magnification images in Figure 5C-F, the Fe containing samples exhibit the petal-like surface structure characteristic for LDH [28, 22, 29], also when doped with a 3+ (FeCo) or 2+ (FeZn) metal ion. The samples show structural widths in the order of several 100 nm, with exception of the FeAl sample, which generally appears to have a similar structure, however on a substantially smaller scale that was only visible at 500 kx magnification. The same was also true for the other, Fe-free Al samples. Surprisingly, this significant difference in surface morphology did not have a big impact on OER activity, as shown in Figure 3c. FeCu is the only Fe containing samples not showing the aforementioned petal-like structure (Figure 5G). Instead, the surface is decorated with crystalline chunks, which were identified to be primarily CuO_x species by means of EDX (Figure 5H). The underlying surface contains both Ni and Fe, but appears not to form NiFe-LDH, indicating that the Cu not only doesn't integrate into the LDH structure, but also actively inhibits its formation. Additionally, the Copper CuO_x crystallites are likely to block the catalytically more active Ni and Fe below, further impairing the OER activity.

The FTIR spectra (Figure 6) show an adsorption peak around 1350 cm^{-1} characteristic for CO_3^{2-} [30], except for the NiCu and FeCu samples. This is again an indication that LDH was formed, since one would expect carbonate anions to be intercalated in those structures. NiCu and FeCu miss this peak, meaning that there is no LDH present in the sample. This gives further confirmation that the addition of Cu inhibits LDH formation in compounds that would otherwise show this structure. XPS spectra were recorded for all Fe containing samples.

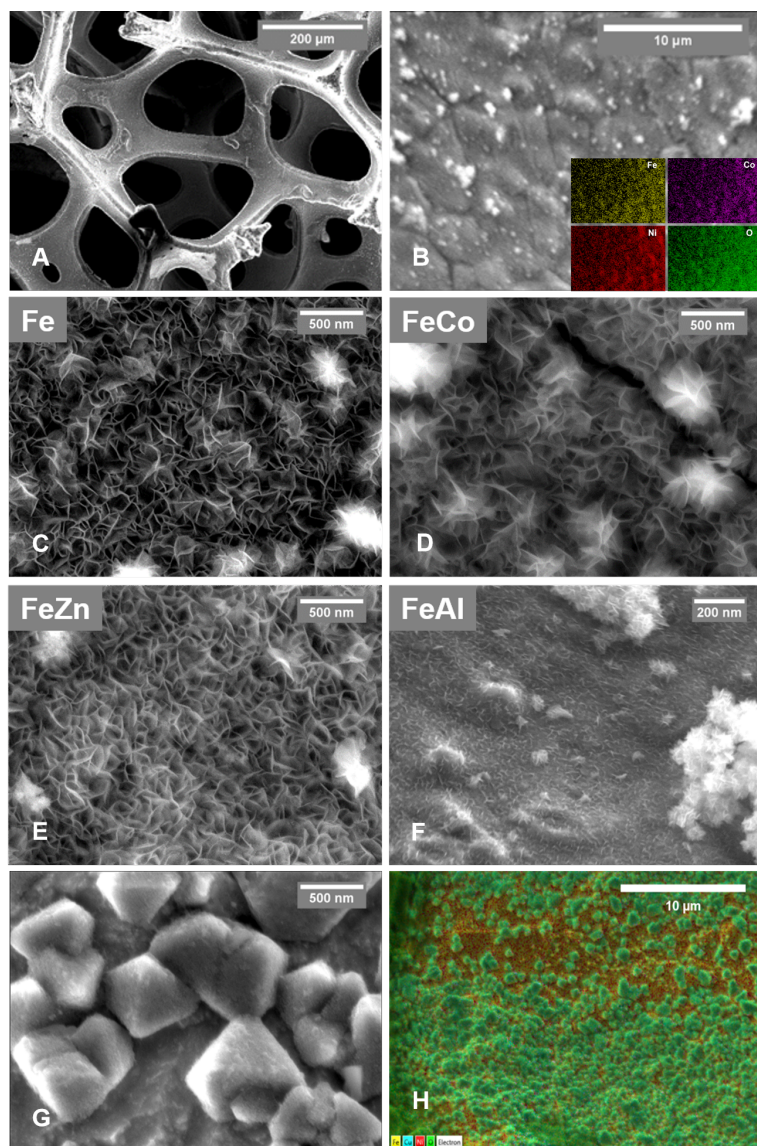


Figure 5. Ni foam surface after synthesis (A) and SEM-EDX image with elemental maps (B), indicating an even coating of the surface and homogeneous dispersion of the dopant in the deposition layer on the example of the FeCo sample. C-F: SEM images of Fe, FeCo, FeZn (250kx magnification) and FeAl (500kx magnification) samples. All samples show the petal-shaped surface structure characteristic for LDH-type materials, although the feature size is substantially smaller for the FeAl sample. G-H: SEM image and layered EDX maps of the FeCu sample showing phase separation of CuO_x species decorating a NiFe surface.

In Figure 7, the XPS Ni 2p spectrum of the Fe sample show peaks at 855.4 eV and 873.0 eV, which correspond to the Ni 2p_{3/2} and Ni 2p_{1/2} orbits, as well as their corresponding satellite peaks at 861.1 eV and 879.0 eV. These results indicate the Ni^{2+} oxidation state. The Fe 2p spectrum shows peaks at 711.3 eV and 724.4 eV (Fe 2p_{3/2} and Fe 2p_{1/2}) and their satellite peaks at 716.8 eV and 729.0 eV, which are typical characteristics of Fe^{3+} . The Co 2p spectrum (FeCo sample) displays a Co^{3+} spin-orbit doublet at 780.3 eV (Co 2p_{3/2}) and 796.0 eV (Co 2p_{1/2}) binding energy [31]. Their shakeup type satellite peaks appear around 785.1 eV and 802.5 eV. This means the initially present Co^{2+} has oxidized to Co^{3+} during the co-precipitation process. Mn 2p (FeMn sample) is also supplied as Mn^{2+} but shows peaks at 643.7 eV (Mn 2p_{3/2}) and 655.3 eV (Mn 2p_{1/2}), confirming that it is present in a 3+ oxidation state [32, 33, 34].

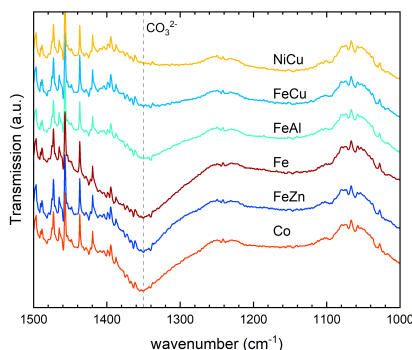


Figure 6. FTIR spectra showing the intercalation of CO_3^{2-} when 3+ ions are present in the deposition layer, indicating LDH formation.

Additionally, there are peaks at 639.3 eV corresponding to Mn metal [34], as well as a satellite peak at 648.0 eV. The FeCu sample shows no signs of $Cu(OH)_2$, for which a peak at 934.8 ± 0.5 eV would be expected [35]. The strong satellite features around 942 eV and the Cu 2p_{3/2} peak at 933.5 eV indicate the presence of $Cu(II)O$, while the Cu 2p_{1/2} peak at 932.3 eV suggest a substantial amount of $Cu(I)_2O$ [35]. The remaining dopants (Cr^{3+} , Al^{3+} , Zn^{2+}) were identified to be in their original oxidation state. The survey spectra (Figure 9) show no presence of nitrogen in the samples, which suggests that CO_3^{2-} has been intercalated instead of NO_3^- , which appears reasonable given the high tendency for anion exchange reactions towards carbonate intercalation in LDH-type materials [36, 37, 38].

XRD patterns in Figure 8 show the characteristic diffraction peaks of CO_3^{2-} intercalated NiFe LDH (PDF no. 40-0215) at 11.3° (003), 22.9° (006), 34.4° (012), 38.8° (015), 46.5° (018), 59.9° (110) and 61.2° (113) for the Fe sample. A small, additional peak is found at 28.4° that cannot be attributed to the LDH phase. This might originate

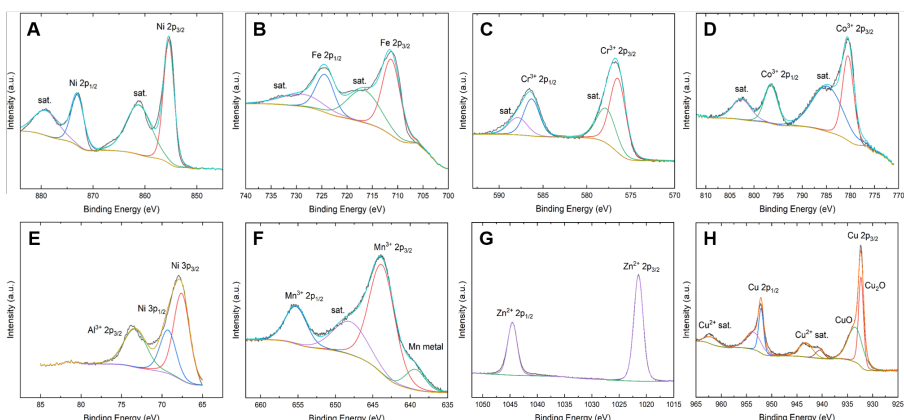


Figure 7. XPS spectra of Ni2p and Fe2p from Fe sample; 2p spectra of the other metals from the respective Fe containing samples.

from secondary phases formed during the synthesis process. The other Fe containing samples show comparable diffraction patterns, although crystallinity is generally low, and not all peaks are discernible in all samples. Nonetheless, this indicates that layered double hydroxide is present and the main phase in all samples containing Fe. FeCu again presents an exception with very low crystallinity and only the (003), (012) and the double peak around 60° visible. Surprisingly, no signs of a CuO_x phase are found in the data that was identified in the EDX maps and XPS spectra.

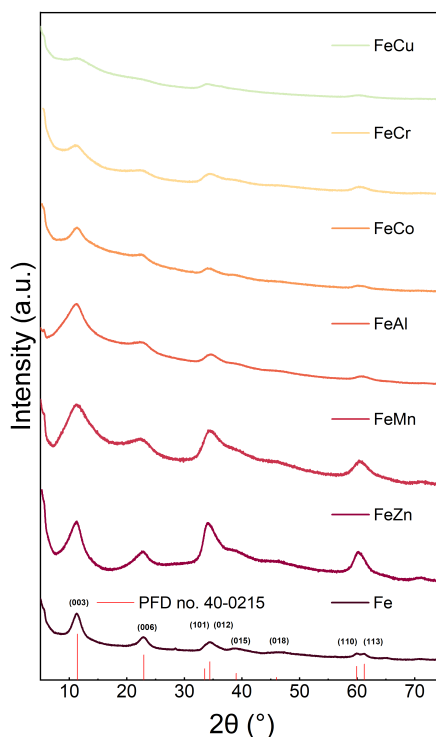


Figure 8. XRD patterns of Fe compounds. All samples show the characteristic NiFe-LDH peaks (PDF no. 40-0215).

4 CONCLUSION

In this work, a screening study of Ni based transition metal hydroxide compounds as catalysts for the OER in conventional alkaline and seawater electrolysis was conducted. A co-precipitation synthesis method was used to coat the active layer onto a Ni foam substrate.

Fe-containing compounds performed at least 35 mV better than Fe-free compounds, with the exception of FeCu. SEM, EDX and XPS revealed that the formation of copper oxides blocking the sample surface and the apparent prevention of LDH formation when Cu is added as the cause. Cr, Co and Al doping resulted in further improvement of the NiFe-LDH, achieving 247 mV overpotential at 10 mA cm^{-2} in the case of NiFeCr-LDH. XPS showed that Co and Mn, supplied as $2+$ ions, fully oxidize to $3+$ states. FTIR and XPS showed that the LDH materials were carbonate intercalated. Although some Fe-free samples show good OER activity, the best of them (Al, Co) still trail behind the Fe compounds by about 60 mV. Nonetheless, these results can be the starting point for a

more detailed study on Fe-free LDH compositions with high OER activity. The results in both electrolytes were largely similar, which means that most compounds are equally interesting for both conventional and seawater electrolysis as highly active OER catalyst. Nonetheless, some compositions show considerable differences in overpotential such as Mn, which can be the starting point for more in depth studies on the effect of salinity on the OER activity. Future work must also investigate whether practical current densities in the order of 1000 mA cm^{-2} can be reached below the thermodynamic onset potential of the chlorine evolution reaction while maintaining long-term stability.

REFERENCES

- [1] Mijndert van der Spek, Catherine Banet, Christian Bauer, Paolo Gabrielli, Ward Goldthorpe, Marco Mazzotti, Svend T. Munkejord, Nils A. Røkke, Nilay Shah, Nixon Sunny, Daniel Sutter, J. Martin Trusler, and Matteo Gazzani. Perspective on the hydrogen economy as a pathway to reach net-zero CO₂ emissions in Europe†. *Energy and Environmental Science*, 15(3):1034–1077, 2022.
- [2] George W. Crabtree, Mildred S. Dresselhaus, and Michelle V. Buchanan. The hydrogen economy. *Physics Today*, 57(12):39–44, 2004.
- [3] G. Matute, J. M. Yusta, and L. C. Correias. Techno-economic modelling of water electrolyzers in the range of several MW to provide grid services while generating hydrogen for different applications: A case study in Spain applied to mobility with FCEVs. *International Journal of Hydrogen Energy*, 44(33):17431–17442, 2019.
- [4] John O.M. Bockris. The hydrogen economy: Its history. *International Journal of Hydrogen Energy*, 38(6):2579–2588, feb 2013.
- [5] Martín David, Carlos Ocampo-Martínez, and Ricardo Sánchez-Peña. Advances in alkaline water electrolyzers: A review. *Journal of Energy Storage*, 23:392–403, jun 2019.
- [6] Marcelo Carmo, David L. Fritz, Jürgen Mergel, and Detlef Stolten. A comprehensive review on PEM water electrolysis. *International Journal of Hydrogen Energy*, 38(12):4901–4934, apr 2013.
- [7] Immanuel Vincent and Dmitri Bessarabov. Low cost hydrogen production by anion exchange membrane electrolysis: A review. *Renewable and Sustainable Energy Reviews*, 81:1690–1704, jan 2018.
- [8] A. Hauch, R. Küngas, P. Blennow, A. B. Hansen, J. B. Hansen, B. V. Mathiesen, and M. B. Mogensen. Recent advances in solid oxide cell technology for electrolysis. *Science*, 370(6513), 2020.
- [9] Sören Drespf, Fabio Dionigi, Malte Klingenhof, and Peter Strasser. Direct elec-

- trolytic splitting of seawater: Opportunities and challenges. *ACS Energy Letters*, 4(4):933–942, 2019.
- [10] Tamim Younos and Kimberly E Tulou. Overview of Techniques Overview of Desalination Techniques. *JOURNAL OF CONTEMPORARY WATER RESEARCH & EDUCATION*, 132(1):3–10, 2005.
 - [11] Ioannis C. Karagiannis and Petros G. Soldatos. Water desalination cost literature: review and assessment. *Desalination*, 223(1-3):448–456, 2008.
 - [12] Takuya Okada, Hikaru Abe, Ai Murakami, Tomohito Shimizu, Kenta Fujii, Toru Wakabayashi, and Masaharu Nakayama. A Bilayer Structure Composed of Mg—Co—MnO₂ Deposited on a Co(OH)₂ Film to Realize Selective Oxygen Evolution from Chloride-Containing Water. *Langmuir*, 36(19):5227–5235, 2020.
 - [13] Fabio Dionigi, Tobias Reier, Zarina Pawolek, Manuel Gliech, and Peter Strasser. Design Criteria, Operating Conditions, and Nickel-Iron Hydroxide Catalyst Materials for Selective Seawater Electrolysis. *ChemSusChem*, 9(9):962–972, 2016.
 - [14] Shanshan Jiang, Yang Liu, Hao Qiu, Chao Su, and Zongping Shao. High Selectivity Electrocatalysts for Oxygen Evolution Reaction and Anti-Chlorine Corrosion Strategies in Seawater Splitting. *Catalysts*, 12(3):261, feb 2022.
 - [15] Yuan Kong, Yi Wang, Wei Chu, and Zhongqing Liu. Tailoring surface and interface electronic structure of NiFe LDH via V doping for enhanced oxygen evolution reaction. *Journal of Alloys and Compounds*, 885:160929, dec 2021.
 - [16] Mengzhou Yu, Jiqi Zheng, and Ming Guo. La-doped NiFe-LDH coupled with hierarchical vertically aligned MXene frameworks for efficient overall water splitting. *Journal of Energy Chemistry*, 70:472–479, jul 2022.
 - [17] Gaiyun Zhao, Biao Wang, Qi Yan, and Xiaohong Xia. Mo-doping-assisted electrochemical transformation to generate CoFe LDH as the highly efficient electrocatalyst for overall water splitting. *Journal of Alloys and Compounds*, 902:163738, may 2022.
 - [18] Jian Bao, Zhaolong Wang, Junfeng Xie, Li Xu, Fengcai Lei, Meili Guan, Yan Zhao, Yunpeng Huang, Huaming Li, Rsc Li, / Chemcomm, and Chemcomm Communication. A ternary cobalt-molybdenum-vanadium layered double hydroxide nanosheet array as an efficient bifunctional electrocatalyst for overall water splitting †. *Chem. Commun*, 55:3521, 2019.
 - [19] Yonghao Gan, Zhi Li, Ying Ye, Xiaoping Dai, Fei Nie, Xueli Yin, Ziteng Ren, Baoqiang Wu, Yihua Cao, Run Cai, Xin Zhang, and Weiyu Song. Doping Mo into NiFe LDH/NiSe Heterostructure to Enhance Oxygen Evolution Activity by Synergistically Facilitating Electronic Modulation and Surface Reconstruction. *ChemSusChem*, 15(20), 2022.

- [20] Mengjie Liu, Kyung Ah Min, Byungchan Han, and Lawrence Yoon Suk Lee. Interfacing or Doping? Role of Ce in Highly Promoted Water Oxidation of NiFe-Layered Double Hydroxide. *Advanced Energy Materials*, 11(33):1–11, 2021.
- [21] Xinxuan Duan, Pengsong Li, Daojin Zhou, Shiyuan Wang, Hai Liu, Zhaolei Wang, Xingheng Zhang, Guotao Yang, Zhuang Zhang, Guoying Tan, Yaping Li, Lijun Xu, Wen Liu, Zihao Xing, Yun Kuang, and Xiaoming Sun. Stabilizing single-atomic ruthenium by ferrous ion doped NiFe-LDH towards highly efficient and sustained water oxidation. *Chemical Engineering Journal*, 446:136962, oct 2022.
- [22] Hongying Li, Xueliang Wang, Tao Wang, and Fengxia Xiao. A facile, green and time-saving method to prepare partially crystalline NiFe layered double hydroxide nanosheets on nickel foam for superior OER catalysis. *Journal of Alloys and Compounds*, 844:156224, 2020.
- [23] Jing Jiang, Ailing Zhang, Lili Li, and Lunhong Ai. Nickel–cobalt layered double hydroxide nanosheets as high-performance electrocatalyst for oxygen evolution reaction. *Journal of Power Sources*, 278:445–451, 2015.
- [24] Liangliang Feng, Yingying Du, Jianfeng Huang, Liyun Cao, Li Feng, Yongqiang Feng, Qianqian Liu, Dan Yang, and Koji Kajiyoshi. Nanoporous nial-ldh nanosheet arrays with optimized ni active sites for efficient electrocatalytic alkaline water splitting. *Sustainable Energy Fuels*, 4:2850–2858, 2020.
- [25] Dennis A. Corrigan and Shyam P. Maheswari. Catalysis of the Oxygen Evolution Reaction By Trace Iron Impurities in Thin Film Nickel Oxide Electrodes. *Electrochemical Society Extended Abstracts*, 85-1:934–935, 1987.
- [26] Dennis A. Corrigan and Richard M. Bendert. Effect of Coprecipitated Metal Ions on the Electrochemistry of Nickel Hydroxide Thin Films: Cyclic Voltammetry in 1M KOH . *Journal of The Electrochemical Society*, 136(3):723–728, 1989.
- [27] Sengen Anantharaj, Subrata Kundu, and Suguru Noda. “The Fe Effect”: A review unveiling the critical roles of Fe in enhancing OER activity of Ni and Co based catalysts. *Nano Energy*, 80(February 2020):105514, 2021.
- [28] Fabio Dionigi and Peter Strasser. NiFe-Based (Oxy)hydroxide Catalysts for Oxygen Evolution Reaction in Non-Acidic Electrolytes. *Advanced Energy Materials*, 6(23), 2016.
- [29] Michaela S Burke, Matthew G Kast, Lena Trotochaud, Adam M Smith, and Shannon W Boettcher. Cobalt-Iron (Oxy)hydroxide Oxygen Evolution Electrocatalysts: The Role of Structure and Composition on Activity, Stability, and Mechanism. *Journal of the American Chemical Society*, 137(10):3638–3648, 2015.
- [30] Mariko Adachi-Pagano, Claude Forano, and Jean Pierre Besse. Synthesis of Al-rich hydrotalcite-like compounds by using the urea hydrolysis reaction - Control of size

- and morphology. *Journal of Materials Chemistry*, 13(8):1988–1993, 2003.
- [31] Henan Jia, Zhaoyue Wang, Xiaohang Zheng, Jinghuang Lin, Haoyan Liang, Yifei Cai, Junlei Qi, Jian Cao, Jicai Feng, and Weidong Fei. Interlaced Ni-Co LDH nanosheets wrapped Co₉S₈ nanotube with hierarchical structure toward high performance supercapacitors. *Chemical Engineering Journal*, 351:348–355, nov 2018.
 - [32] Yaqiong Wang, Shi Tao, He Lin, Shaobo Han, Wenhua Zhong, Yangshan Xie, Jue Hu, and Shihe Yang. NaBH₄ induces a high ratio of Ni³⁺/Ni²⁺+boosting OER activity of the NiFe LDH electrocatalyst. *RSC Advances*, 10(55):33475–33482, 2020.
 - [33] Saurabh Singh, Nanasaheb M. Shinde, Qi Xun Xia, Chandu V.V.M. Gopi, Je Moon Yun, Rajaram S. Mane, and Kwang Ho Kim. Tailoring the morphology followed by the electrochemical performance of NiMn-LDH nanosheet arrays through controlled Co-doping for high-energy and power asymmetric supercapacitors. *Dalton Transactions*, 46(38):12876–12883, 2017.
 - [34] Mark C. Biesinger, Brad P. Payne, Andrew P. Grosvenor, Leo W.M. Lau, Andrea R. Gerson, and Roger St C. Smart. Resolving surface chemical states in XPS analysis of first row transition metals, oxides and hydroxides: Cr, Mn, Fe, Co and Ni. *Applied Surface Science*, 257(7):2717–2730, 2011.
 - [35] Mark C. Biesinger. Advanced analysis of copper X-ray photoelectron spectra. *Surface and Interface Analysis*, 49(13):1325–1334, 2017.
 - [36] B M Hunter, W Hieringer, J R Winkler, H B Gray, and A M Mü. Effect of interlayer anions on [NiFe]-LDH nanosheet water oxidation activity †. — *Energy Environ. Sci*, 9:1734, 2016.
 - [37] Jose A. Carrasco, Roger Sanchis-Gual, Alvaro Seijas-Da Silva, Gonzalo Abellan, and Eugenio Coronado. Influence of the interlayer space on the water oxidation performance in a family of surfactant-intercalated NiFe-layered double hydroxides. *Chemistry of Materials*, 31(17):6798–6807, 2019.
 - [38] Christine Taviot-Guého, Pierre Vialat, Fabrice Leroux, Fatemeh Razzaghi, Hubert Perrot, Ozlem Sel, Nicholai Daugaard Jensen, Ulla Gro Nielsen, Sophie Peulon, Erik Elkaim, and Christine Mousty. Dynamic characterization of inter- and intralamellar domains of cobalt-based layered double hydroxides upon electrochemical oxidation. *Chemistry of Materials*, 28(21):7793–7806, 2016.

SUPPLEMENTARY INFORMATION

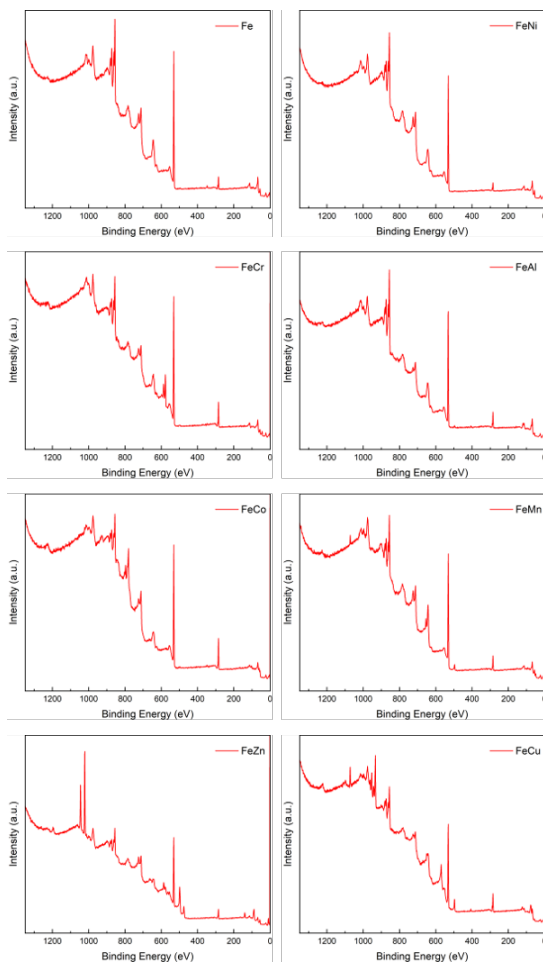


Figure 9. XPS survey spectra of Fe containing samples. There are no signs for Nitrogen in the samples (except for small amounts of NaNO_3 impurities in the FeCu sample), indicating that intercalated NO_3^- is quickly exchanged for CO_3^{2-} .

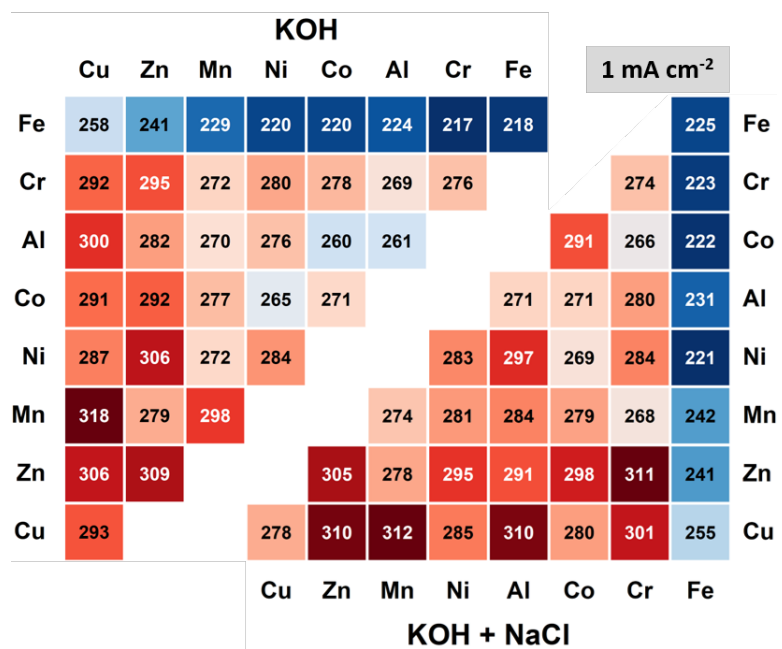


Figure 10. Heatmap at 1 mA cm⁻².

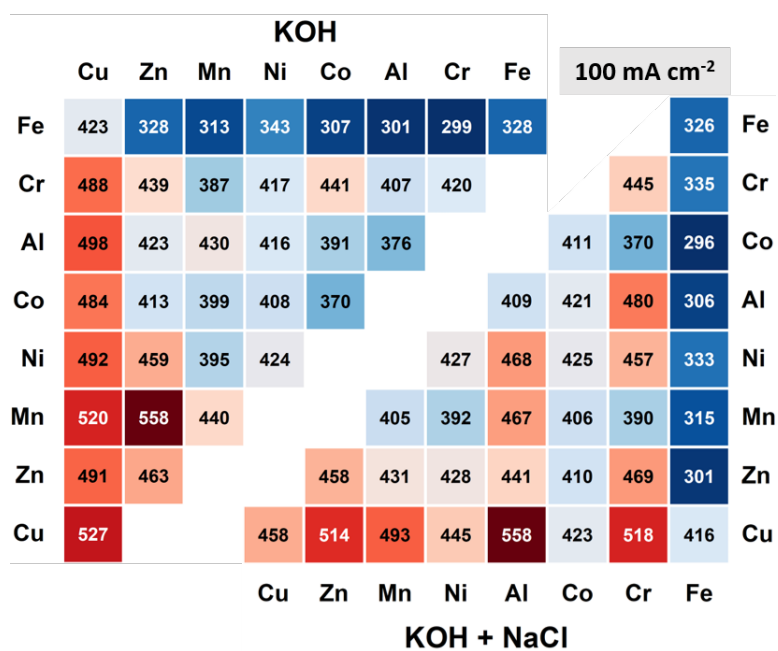


Figure 11. Heatmap at 100 mA cm⁻².

CHAPTER 5

Autonomous Catalyst Development for alkaline OER

5.1 Introduction

The synthesis method detailed in the preceding chapter (4) yielded samples of high performance and good reproducibility, achieved through a remarkably rapid and straightforward procedure.

At the same time, this method opens up a vast phase space of interesting materials thanks to the adaptable layered double hydroxide structure. This structure can accommodate a wide range of cations and interlayer anions. NiFe LDH is among the best-performing PGM-free catalysts in terms of alkaline OER activity but still has shortcomings, e.g. degradation caused by Fe leaching in strong bases [97, 98], especially at elevated temperatures. Using DFT calculations and in-operando techniques, Dionigi *et al.* showed in 2020 that the low overpotentials of *M*Fe LDH stem from O-bridged Fe-*M* reaction centers that stabilize OER intermediates [106], and based on that suggested the doping with redox-flexible cations as a general design principle for improved OER catalysts.

However, the numerous studies that have already investigated numerous dopants (Co, Cr, Al, Mn, V, La, Ce, to name only a few) for Ni and Fe based LDH in an effort to enhance activity and stability illustrate that this endeavor resembles the search for a needle in a haystack. The studies, as a whole, remain inconclusive as to which

dopant or combination of dopants is optimal, due to different synthesis procedures, testing protocols and setups or data analysis. Investigating large arrays of compositions under identical circumstances would allow for much better comparability, but would practically be extremely laborious despite the co-precipitation method being quite fast.

At present, metal hydroxide compositions beyond four doping elements have not even been explored in the field of OER catalysis, not least because the experimental effort would be unreasonable.

These circumstances make this synthesis approach a particularly interesting subject for high-throughput experimentation (HTE). HTE systems need sufficiently simple experiments such that the procedure does not become too complex to handle. While in practice the realisation of this project was not as straight-forward as one would expect given that the synthesis only consists of two dipping steps in aqueous solution (this is discussed in more detail in section 5.3), it is still considerably simpler than most procedures. As our work in "*Machine Learning Guided Development of High-Performance Nano-Structured Nickel Electrodes for Alkaline Water Electrolysis*" (see Chapter 6) has shown, applying ML to discrete optimization problems can accelerate materials discovery tremendously. If combined with HTE, otherwise inaccessible phase spaces can be investigated for high performance materials with complex, multi element compositions. Based on these considerations, we designed a materials acceleration platform based on a liquid- and sample-handling robotic arm to automate such an optimization experiment for the development of highly active alkaline OER catalysts. This project is a collaborative effort with several people across two sections actively involved in theory and practice. The design of the experimental concept and bespoke synthesis and testing equipment, as well as data analysis and sample pretreatment were mainly carried out by the author of this thesis. The software backbone, including data acquisition, handling, storing and integration of the optimization functionality into the workflow was mainly carried out by Nis Fisker-Bødker. The manuscript draft was written by the author of this thesis.

The project is still ongoing and the results presented herein are preliminary and will be followed by much more conclusive findings.

5.2 Manuscript draft

Autonomous Catalyst Development for Alkaline OER

Enzo Raffaele Moretti, Nis Fisker-Bødker, Tejs Vegge, Mikkel Kraglund, Jinhyun Chang, and Ragnar Kiebach

Department of Energy Conversion and Storage, Technical University of Denmark, Anker Engelunds Vej, 2800 Kgs. Lyngby, Denmark.

ABSTRACT

A lot of scientific effort is put into the search for highly efficient OER catalysts for alkaline water electrolysis that are ideally also robust and noble metal free at the same time. NiFe oxides and hydroxides have shown excellent OER activity and served as the starting point for many studies involving the addition of up to three dopants to the structure in an effort to improve its desired characteristics even further. However, as in all domains of materials research, the enormous scope of relevant compositions effectively limits experimental research to very small subsets of the entire phase space. In this work, we present an autonomous closed-loop materials screening system based on the rapid synthesis and characterization of multi metal hydroxides, which to the best of the authors knowledge is the first system of this type reported to date. Compounds are deposited on a Ni foam substrate by a co-precipitation method with varying ratios of metal ion precursors (Fe^{3+} , Cr^{3+} , Al^{3+} , Co^{2+} , Ni^{2+} , Mn^{2+} , Zn^{2+} , Cu^{2+}) and electrochemically investigated in a beaker-type, 3-electrode cell similar to conventional test setups. The system is able to synthesize and electrochemically test up to 75 different material compositions per day without human interaction. The meta-heuristic bayesian optimization algorithm Dragonfly is used to optimize the composition by analyzing trends in the test results and choosing the most promising candidate after every experimental iteration. We show first results in terms of data quality and reproducibility, as well as the optimization in a four and eight metal space. These findings showcase how autonomous materials discovery can make complex, multi-element compositions accessible for research and accelerate the development of novel materials drastically.

Keywords: autonomous experimentation, catalysis, alkaline electrolysis, oxygen evolution reaction

1 INTRODUCTION

As of today, green hydrogen is primarily produced via alkaline electrolysis, the most mature among the three major water splitting technologies [1]. One of the key obstacles on the path towards cheap, green hydrogen is the slow kinetics of the oxygen evolution reaction (OER), which is responsible for most of the energy loss during electrochemical water splitting. This is illustrated by the much higher overpotentials typically seen for the OER compared to the HER [2]. In recent years, substantial research effort has been spent on improved OER catalysts and particularly layered double hydroxides (LDH) have attracted a lot of interest in the scientific community [3, 4, 5, 6].

These materials show a similar structure to the naturally occurring hydrotalcite:



It consists of brucite-like metal hydroxide layers, in which some of the M^{2+} cations are substituted by M^{3+} cations (typically $x = 0.2 \dots 0.33$). The created net positive charge is balanced by hydrated A^{n-} anions between the layers (see Figure 1). The structure can accommodate a wide range of divalent (Co^{2+} , Ni^{2+} , ...) and trivalent (Fe^{3+} , Al^{3+} , ...) cations as well as interlayer anions (CO_3^{2-} , NO_3^- , various organic surfactants, ...). Even M^+ and M^{4+} cations are possible, however limited to specific examples such as Li^+ and Ti^{4+} [8].

This flexible composition makes the LDH properties tunable for various different applications such as CO_2 capture [9] and photocatalytic reduction [10] or

as an alkaline OER catalyst. For the latter, NiFe and CoFe based LDH have been a popular research subject. Although their long-term stability in alkaline environments is still a matter of debate [11, 12], these materials are PGM free, therefore prospectively cheap to produce and show exceptional OER performance [13, 14, 15, 16].

The presence of Fe, even in trace amounts, increases the OER activity manifold compared to plain Ni or Co hydroxide. This behavior has been discovered in the mid 80's by

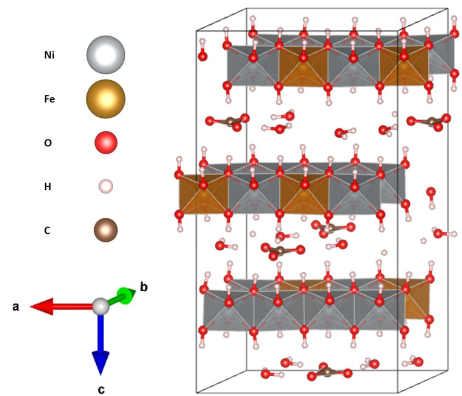


Figure 1. Schematic illustration of the NiFe LDH structure. The divalent (Ni) and trivalent (Fe) ions as well as the interlayer anions can be replaced by a wide range of different elements. Adapted from [7].

Młynarek et al. [17] and further investigated by Corrigan et al. [18, 19]. In 2020, Anantharaj et al. reviewed the proposed mechanisms for the “Fe effect”, showing that there are several conflicting proposals, and the exact catalytic mechanism still remains unclear [20]. Around the same time, Dionigi et al. propose that the OER proceeds via a Mars van Krevelen mechanism based on DFT calculations and in-operando measurements[7]. They attribute the effect to the stabilization of OER intermediates through O-bridged Fe-M reaction centers on the catalyst surface and suggest doping with redox-flexible cations as a route to improved OER catalysts. Consequently, many studies investigate doping these materials with one or more additional elements to improve OER activity and mitigate degradation issues [21, 22, 23, 24, 25, 26, 27, 28, 29, 30]. This iterative approach remains highly time-consuming and labor-intensive. The number of material combinations increases exponentially with the addition of dopants and other process variables, limiting practical research to small subsets of the overall search space. This is a well-recognized challenge in all domains of materials research. Furthermore, differences in synthesis or test procedure can often make it difficult to find a “true optimum” across different publications.

Computational techniques such as DFT simulation can help understand reaction mechanisms such as the OER and narrow down the search for better catalyst compositions. Although the rapid progress in computational power has in fact accelerated the development of novel materials, complex, multi-length-scale problems like electrocatalysis are often very demanding to simulate from first principles and examples remain rare [31, 32, 7]. Machine-learning based optimization on the other hand can help minimize the amount of experiments needed to find a certain optimum [33, 34, 35, 36, 37, 38], but ultimately still relies on the access to a large, high-quality data set. As a result, a lot of effort has been put into autonomous, high-throughput experimentation systems [39, 40, 41, 42, 43, 44, 45, 46, 47, 48, 49, 50] that can not only take advantage of the aforementioned computational developments, but also speed up the experimental part of materials design by orders of magnitude.

Despite great advances in autonomous materials discovery in recent years, a high-throughput autonomous experimentation system for alkaline OER catalysts has not been demonstrated. Among the systems demonstrated in other fields of materials research, many also share a similar experimental approach: the performance assessment of the samples relies on structural characterizations and testing in proxy experiments, since the complexity of many common experimental setups render them unfeasible for autonomous systems. This often means that the performance in the real-world application is only indirectly assessed. The current study addresses these shortcomings by directly testing OER activity in aqueous KOH on Ni foam substrates, closely resembling the

conditions for alkaline electrolysis.

The experimental setup automizes a facile NiFe-LDH co-precipitation synthesis route at room-temperature [51] by means of a robotic platform. The synthesis takes place directly on a Ni foam substrate by successively immersing it in metal nitrate and sodium hydroxide solutions. In addition to the synthesis, the system electrochemically characterizes the samples with respect to alkaline OER catalysis in a 3-electrode setup, analyses the output data and feeds calculated figures of merit (FoM) into the meta-heuristic optimization algorithm known as Dragonfly (DA) [52]. Based on the descriptors of the input values (metal nitrate precursors) and the output FoMs this algorithm then calculates an optimal combination of new input values for the next synthesis, which are fed into the robot control script. This therefore represents a closed-loop system which optimizes the desired properties of a certain material class with no necessity for human interaction.

2 MATERIALS AND METHODS

2.1 Materials

The following powder chemicals have been used to prepare 0.4 M metal nitrate stock solutions by dissolution in DI water: nickel (II) nitrate hexahydrate (99% Thermo Scientific), iron (III) nitrate nonahydrate (99%, Thermo Scientific), chromium (III) nitrate nonahydrate (99%, Thermo Scientific), copper (II) nitrate hemipentahydrate (99%, Thermo Scientific), aluminium (III) nitrate nonahydrate (99%, Thermo Scientific), manganese (II) nitrate tetrahydrate (98%, Thermo Scientific), zinc (II) nitrate hexahydrate (99%, Thermo Scientific), cobalt (II) nitrate hexahydrate (99%, Sigma-Aldrich). 1 M KOH and 2.5 M NaOH were diluted from concentrated solutions (45 wt.% NaOH and 47 wt.% KOH, Sigma Aldrich) that were pre-electrolysed for 24 h at 2.0 V. Ni foam substrates were cut to size from 300 mm * 200 mm * 1.6 mm sheets (450 µm cell size, Alantum). PTFE spray (Biltema) was used to treat the Ni foam strips.

3 SYNTHESIS PROCEDURE

The general concept of the experiment is based on a facile synthesis route for mixed metal hydroxide deposition directly onto Ni foam substrates. In the NiFe LDH case, the Ni foam is immersed in a Fe nitrate solution (0.4M) and set aside. The Fe acts as a Lewis acid and the solution exhibits a pH of ~ 4.5 . Consequently, a small amount of Ni^{2+} ions are dissolved from the foam surface into the surrounding solution. When immersed into a concentrated, strong base (NaOH) in the second synthesis step, the

metal ions co-precipitate to form



The interlayer anion is CO_3^{2-} , because CO_2 will readily dissolve into the base from ambient air, and LDH type materials have a large affinity for CO_3^{2-} intercalation. This approach is applied to obtain multi metal coatings by mixing nitrate solutions of different metals.

4 EXPERIMENTAL WORKFLOW

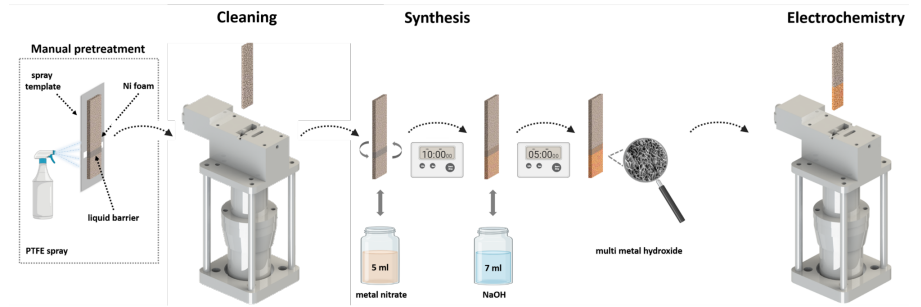


Figure 2. Illustration of the synthesis procedure used for the autonomous experiment.

The experimental workflow consist of 4 major components: manual pretreatment of the Ni foam substrates, synthesis, electrochemical testing as illustrated in Figure 2 and subsequent data handling, analysis and optimization.

Pretreatment

The substrates underwent a manual pretreatment procedure before they were positioned in the sample holder of the experimental setup. The Ni foam sheets were first laser cut into 50 mm * 10 mm * 1.6 mm strips (yielding ca. 120 pieces per Ni foam sheet) and subsequently degreased in an ethanol-acetone (1:1) bath under ultrasonification for 30 min.

Afterwards, the strips were washed in DI water three times and dried overnight at 60 °C. Using a mask, 5 strips at a time were treated with PTFE spray to create a liquid barrier ca. 4 mm below the center of the strips such that subsequent treatments would only effect the lower part of the samples.

Synthesis

Initially, a gripper tool transfers the Ni foam substrate into the electrochemical cell, which is filled with 9 ml 1 M HCl. After 60 s, the cell is drained and subsequently flushed with water three times to remove the remaining HCl in the sample, which is then returned into the sample holder.

A vial is picked up by the gripper tool, transferred to the vial clamp and uncapped. The combination of metal nitrates of choice is dispensed into the vial for a total volume of 5 ml. In this study, up to 8 dopants in 5 % increments were used, although generally the resolution is only limited by the accuracy of the syringe pumps (ca. 10 μ l/0.2 %, depending on viscosity, tube diameter etc.). The foam is then dipped 10 mm into the nitrate mixture under slow rotation (2 Hz) for 10 s and returned to its sample holder position. The used vial is emptied, flushed with water three times, recapped and returned to its position in the vial holder.

A second vial is similarly filled with 7 ml of NaOH, the first sample is dipped in for 10 s without rotation after a waiting period of 10 min and again returned to its sample holder position. After another 5 min waiting period the synthesis is considered complete.

The sample is transferred to the electrochemical test cell for cleaning. After 11.5 ml KOH is dispensed into an electrochemical test cell, an oxidizing current of 100 mA cm⁻² is applied to the sample for 60 s. The cell is then flushed with water three times, after which both the cell and the sample are considered clean and ready for testing.

Electrochemical Testing

For the electrochemical tests, 9 ml of KOH is dispensed into the cell. The testing position was previously calibrated such that the active area of the sample submerged in the electrolyte equals 1 cm².

The potentiostat is then triggered to run a test sequence starting with a short potentiostatic impedance spectroscopy (PEIS) measurement to validate proper electrical connection of the sample to the current collector (100 kHz - 1 kHz, 10 mV amplitude, bias 1.5 V vs. RHE) by measuring the IR drop. If the value is outside a specified interval ($0 \Omega < x \leq 1.5 \Omega$), the test sequence is aborted, the sample returned to the sample holder and the experiment is repeated with the next substrate.

If the connection is sufficient, the sequence is continued according to Table 1. As a second validation step is implemented after the first CP measurement. A potential between the thermodynamic OER onset (1.229 V vs. RHE) and 2.0 V is expected, otherwise the experiment is aborted and repeated as described before.

Once the tests are concluded, the sample is returned to its sample holder position and

Table 1. Electrochemical test sequence used in this study.

Technique	Parameters	U/I window	Cycles
CV	200 mV s^{-1}	0.8 - 1.6 V vs. RHE	25 x
CV	10 mV s^{-1}	0.8 - 1.6 V vs. RHE	1 x
CV	200 mV s^{-1}	0.95 - 1.05 V vs. RHE	100 x
CV	50/75/100/150/200 mV s^{-1}	0.95 - 1.05 V vs. RHE	3 x
PEIS	100 kHz - 1 Hz	$U_{dc} = 1.5$ V vs. RHE, $U_a = 10$ mV	1x
CP	60 s	100/50/20/10/5/2/1 mA	1 x
CV	10 mV s^{-1}	0.8 - 1.6 V vs. RHE	1 x

the cell is cleaned again (9 ml of 1 M HCl (1x), 11.5 ml water (3x), 60 s each).

Data Handling, Analysis and Optimization

The recorded electrochemical measurements as well as metadata including temperature and humidity values, chosen experimental parameters, metal ratios and a unique sample ID are saved as a data set in a HDF5 file container. The optimization of the material composition takes places by means of reinforced learning. The figure of merit (FoM) for optimization, in this case the overpotential at 10 mA cm^{-2} (η_{10}), is calculated by averaging the last 30 s of the CP measurement. This value is 95 % IR corrected and returned to the DA after every experimental iteration which then updates the training data set and suggests a new combination of metal precursors for the next synthesis accordingly. The algorithm is chosen since Gaussian process regression model performs well on relatively small data sets [53].

The experimental workflow as described takes ca. 52 min to complete and thus allows to test ca. 25 samples/day. This throughput can be increased drastically by parallelization of synthesis and electrochemical testing with no physical changes to the system. Testing happens independently of the synthesis, which means that sample n+1 can be prepared while sample n is still in the E-cell. The testing would then be the rate limiting step and the total duration would be reduced to ca. 30 min, increasing the throughput to ca. 48 samples/day. It should be noted that in this case the prediction model is always delayed by one experimental iteration, since the synthesis of sample n+1 takes place before the FoM of sample n has been evaluated.

The test sequence as described in section 4 is designed to provide similar information as regular electrochemical tests in beaker-type cells, including IV-curves, full CVs,

ECSA data and impedance spectroscopy. For purely optimization purposes, this extent of testing is not strictly necessary. In our case, only η_{10} is used as a figure of merit and consequently only surface conditioning and CP steps could be sufficient for this application, potentially increasing the throughput manifold again.

4.1 Experimental setup

4.1.1 Platform

The system is based on the N9 robotic platform from North Robotics. It consists of an aluminium table base, a robotic arm including its C9 controller unit, a pneumatic vial clamp and a liquid dispensing carousel. The table base has outer dimensions of 814

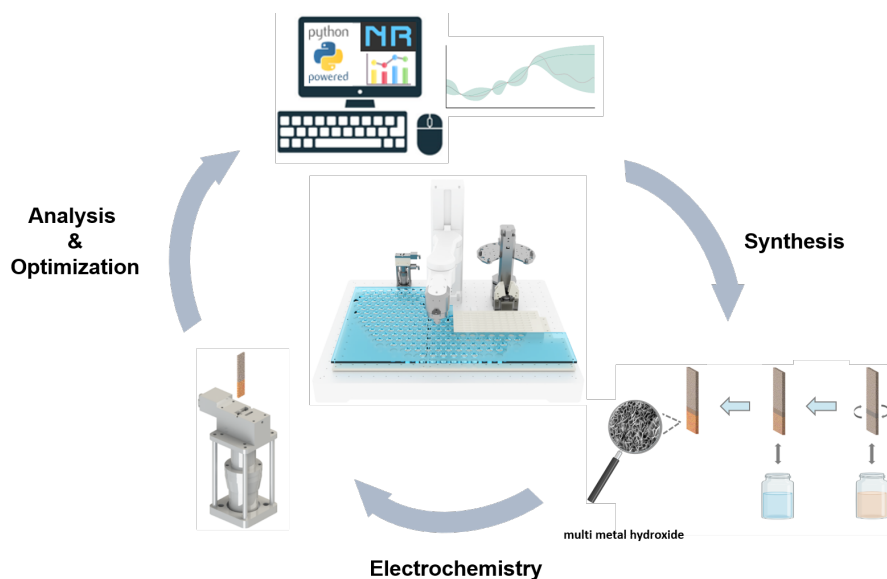


Figure 3. Schematic of the setup used for the autonomous catalyst development experiment.

mm * 664 mm, under mounts for the C9 controller and other auxiliary equipment and a rectangular 37.5 mm grid of M3 tapped holes on the surface. The 4-axis robotic arm features stepping motors to move in the horizontal plane (shoulder and elbow) and along the vertical z-axis. Additionally, there is a pneumatically actuated gripping tool at the end of the robotic arm, which can be rotated at up to 1500 rpm.

4.1.2 Liquid and Sample Handling

The dispensing carousel utilizes stepping motors to iterate between different dispensing positions and move along the z-axis. It is equipped with eight dispensing outlets using

PTFE tubing (1/16" OD, 1/32" ID) and PTFE fittings, which are connected to eight Tricontinent C3000 syringe pumps to dispense metal nitrate precursor solutions (Fe, Cr, Al, Co Ni, Mn, Zn, Cu).

The pumps are fitted with 1.5 ml syringes and offer a dispensing resolution of 3000 steps per full stroke. The inlets of the pumps use larger PTFE tubing (1/8" OD, 3/32" ID) to connect to 3 liter polypropylene bottle chemical reservoirs. The vial clamp is machined from PTFE and dimensioned to fit 27 mm * 40 mm screw cap glass vials.

The vials are arranged in a half offset pattern in a custom-made vial holder that is designed to fully utilize the operational space of the robotic arm, fitting 152 vials in total. One of the vials is fixed in place and acts as a cap holder. The sample holder was machined from PTFE and dimensioned to fit Ni foam strips of size 50 mm * 10 mm * 1.6 mm (450 μ m cell size, Alantum). It features 13.5 mm * 2 mm slits with funnel-shaped openings, and is equipped with a vacuum pump (KNF Laboport membrane pump) to create a drying air draft over the samples and can hold 75 samples in total. The gripper tool head was designed to enable the handling of both vials and Ni foam strips and was CNC machined from aluminium.

Eight additional, 12 V peristaltic pumps with silicone tubing (3 mm OD, 1 mm ID) were used to dispense liquids where less accuracy was needed (MilliQ water, NaOH, KOH, HCl) and as a suction mechanism to clean the used vials after a synthesis was completed.

4.1.3 Electrochemical Test Cell

The electrochemical test cell (E-cell, Figure 4) was CNC machined from PTFE and can hold a maximum of ca. 12 ml of liquid. For cleaning and electrochemical testing the sample is moved into the cell volume with the gripper tool through a 20 mm * 6 mm opening in the lid. It is then pushed against a Platinum plate current collector and held in place by means of a pneumatically actuated PTFE piston. The counter electrode (perforated Ni plate, 300 μ m thickness, 99.98 %, Veco) covers the cross-section of the cell interior (ca. 3 cm * 2 cm) and is fixated by a Ni plated M4 screw, which also acts as the current collector. It is placed in ca. 2 mm distance from the sample position to leave space for the reversible hydrogen reference electrode (Gaskatel Mini Hydroflex) in between, which is angled at 45° relative to the horizontal plane. The current collectors are connected to a 4-port banana plug terminal (separate voltage sensing and current carrying connections on each side) with Ni wire (1 mm Ø, 99.98 %, Alfa Aesar).

The cell lid can accommodate three PTFE tubes (1/16" OD) to dispense KOH, MilliQ water and 1M HCl into the cell as well as a thermocouple for measuring the electrolyte temperature close to the working electrode. The cell is drained through the conically shaped bottom of the cell with a peristaltic pump, which simultaneously acts as a pinch

valve. At the base of the cell assembly, an ultrasonic transducer (60 W, 40 kHz) is attached for cleaning the sample and the cell.

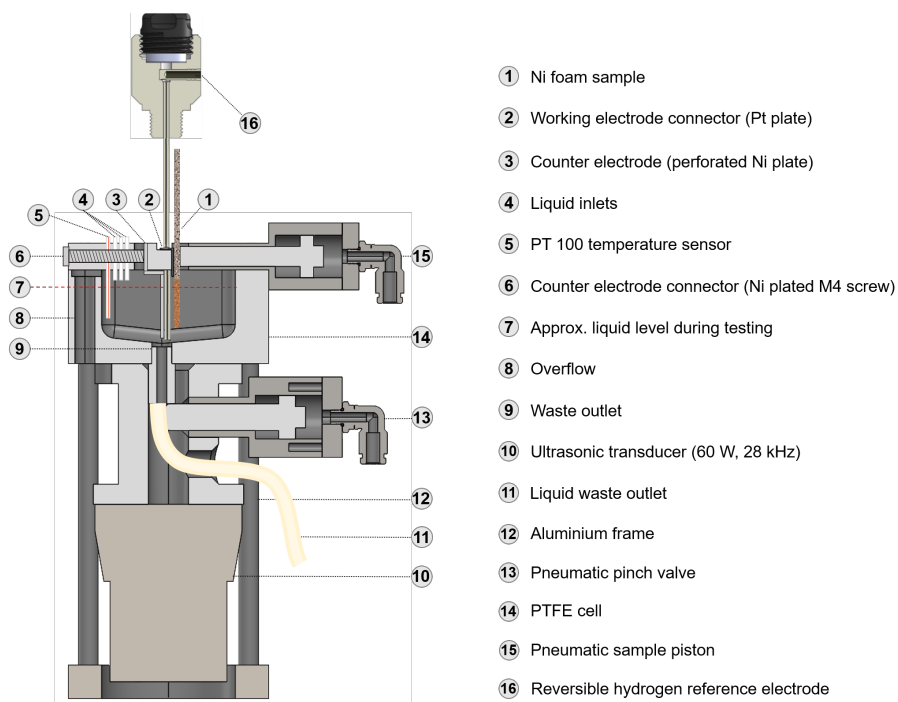


Figure 4. 3D model cross-section of the electrochemical test cell.

4.1.4 Periphery

The robotic arm and all other tools are controlled by the C9 unit, which also offers several electrical and pneumatic I/O connections for additional tools and is connected to the lab computer via USB 2.0. To ensure operational safety, the entire system is located in a fume hood.

In addition to the temperature measurement in the electrolyte, the ambient temperature and relative humidity inside the fume hood cabinet are recorded by means of an Arduino Uno microcontroller. A Gamry Reference 600 Potentiostat is connected to the reference electrode directly and the test cell via the banana plug terminal. The system can be operated through the North Robotics “North IDE” control program via a Python based script and can be tested in silico prior to running an experiment via a 3D digital twin simulator functionality within the North IDE. In the case of this study however, the system was run via Visual Studio Code (Microsoft). Three webcams allow monitoring the system remotely from different angles.

Detailed drawings, images and video recordings of the experimental system in operation can be found in the supporting information (SI).

5 RESULTS AND DISCUSSION

5.1 Data Quality

Figure 5 shows the general quality of the data obtained with the experimental setup on the example of an Fe sample (ID650). In a separator-less cell configuration as used in this study, the interference of oxygen evolved at the anode with the reference electrode (H/H^+) can be a concern. In our case however, both the fast (Figure 5A) and slow (Figure 5B) CV scans show only minimal amounts of noise across the entire potential range, even though high current densities of ca. 100 mA cm^{-2} are reached. Impedance spectroscopy results (Figure 5C) show a small amount of high-frequency inductance ($Z_{Im} < 0$) but otherwise also low noise levels that don't have an adverse effect on data analysis. The measured ohmic drop was typically between 0.6 and 0.9Ω . The

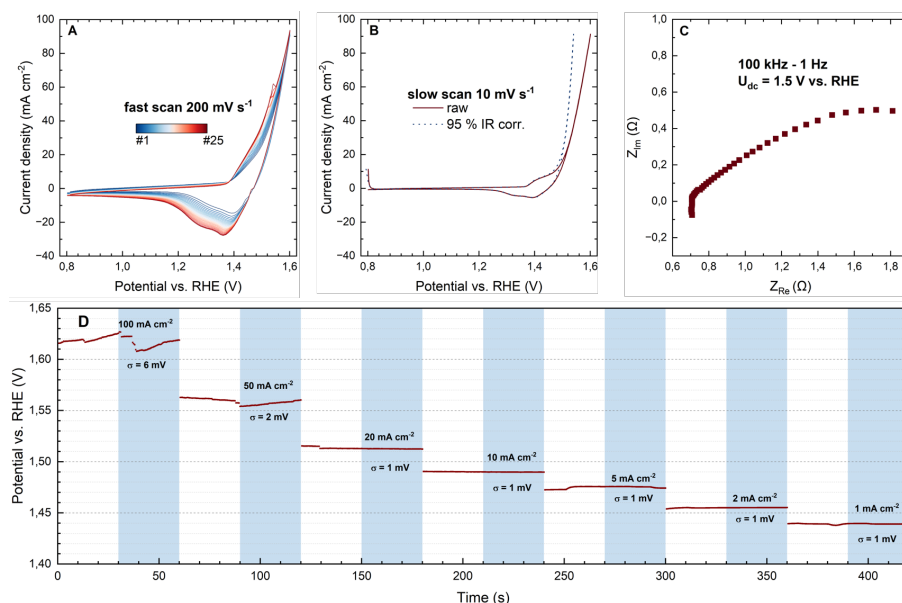


Figure 5. Data quality obtained with the experimental setup on the example of an Fe sample (ID650).

stepped chronopotentiometry (CP) data was evaluated by averaging the last 30 s of each measurement. As can be seen in Figure 5D, the respective standard deviation σ is reasonable at 100 mA cm^{-2} with 6 mV, drops to 1 mV already at 20 mA cm^{-2} and stays this low for the remaining measurements. The IR corrected overpotentials η_{10}

calculated from the CP measurement at 10 mA cm^{-2} were reproducible with a σ of 5 mV between experiments. For the presented study this is of particular importance, since η_{10} is used as the figure of merit for bayesian optimization. Its success depends to a large extent on whether incremental differences can be distinguished, which these results confirm.

In summary, the data quality obtained up to this point is extremely satisfactory and matches regular beaker-type cell setups. To gain information about the electrochemically

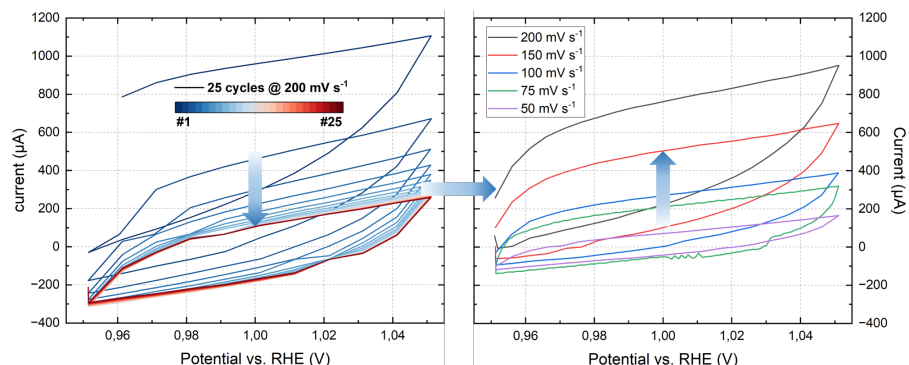


Figure 6. ECSA conditioning and measurement steps indicating technical issues with the potentiostat.

active surface area (ECSA), a series of CV scans with varying scan rate (50 mV s^{-1} - 200 mV s^{-1}) in a non-faradaic region (0.95 V - 1.05 V vs. RHE) were recorded. Prior to the actual measurement, the sample was conditioned by cycling at 200 mV s^{-1} in the same potential range. Figure 6 (left) shows that initially some oxidation occurs (positive current offset), which fades out during cycling. The scans stabilize around zero current, which is expected in a non-faradaic region. Surprisingly, however, the following scans show a current drift in the opposite direction. Additionally, the spread between the linear regions of the anodic and cathodic scan sections increases with the scan rate as expected, but the absolute values are notably larger than the ones recorded only seconds earlier during the conditioning step. The cause of this behaviour could not be conclusively explained within the framework of this study. A possible explanation could be that the potentiostat briefly applies a potential outside the scan interval between the measuring steps, at which the surface of the sample is slightly reduced.

5.2 Replication Study

Prior to multi metal optimization, the previously described synthesis route was used manually to screen single metal, binary and ternary compounds from the same eight metals by using the precursors individually or mixing them in a 1:1 ratio, resulting in

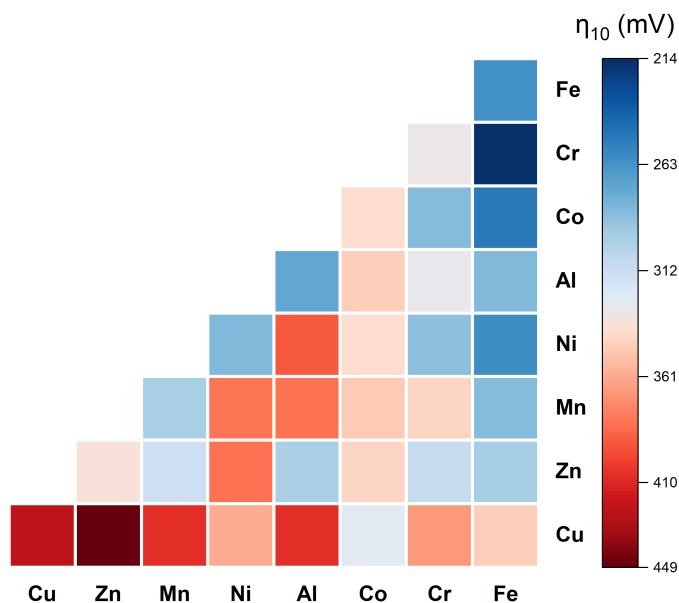


Figure 7. Heat map of linear grid screening results.

36 compositions. The samples are named according to the elements in the precursor solutions, i.e. “Al sample” if the synthesis was carried out using Aluminium nitrate solution or “MnCo sample” if the synthesis was carried out using a mixed Manganese and Cobalt nitrate solution.

It is noteworthy that in this case 0.8 M metal precursors were used and for practical reasons, the test conditions were considerably different. In the manual study, Zirfon PERL UTP 500 (Agfa) was used as a separator, whereas the robotic experiment does not use a separator at all. Additionally, the 1 M KOH used as the electrolyte was not pre-electrolysed as described in 2.1.

This screening matrix was replicated via the robotic experimental system in order to assess its reproducibility and data quality. Figure 7 shows a comparison of the results in the form of a heat map, visualizing the overpotential at 10 mA cm^{-2} . The general trends appear to be the same between the two experiments:

- Fe containing samples outperform those without
- FeCr is revealed as the most active compound among the Fe samples
- Fe and NiFe yield practically identical results
- Al achieves the best results among Fe free samples

- Cu is detrimental, and achieves the worst results across all samples

There are, however, several distinct differences between the manual and the automated study. The absolute range of overpotentials measured is significantly larger in the automated experiments (214 - 449 mV) than the manual counterpart (247 - 378 mV). At the lower end of the range, a possible cause for this could be the difference in cell and sample geometry. The missing separator removes a physical barrier for gas transport from the sample surface and hence can lead to a decrease in η_{10} . Conversely, the pre-electrolysis of the electrolyte removes the majority of Fe impurities that are present in the untreated KOH used in the manual study. Fe traces could increase the OER activities of samples that are nominally Fe free - whereas the corresponding samples in the robotic experiment have less Fe impurities and therefore show much higher η_{10} . Differences in solution molarity and potential HCl residue from the cleaning procedure are factors that might influence the results in either direction.

In addition, there are some outliers in the data set, for example Ni, which perform significantly better than one would expect from the manual screening data - Figure 8B shows a more than 2-fold increase in current density at 1.6 V vs. RHE. This discrepancy is most likely caused by the cleaning process of the E-cell. Operation of the sonicator introduced substantial electrical noise into the data line to the robot controller, such that commands could not be transmitted reliably. For this reason, the data presented in this study was recorded with the sonication steps in the experimental procedure switched off and cleaning of the cell was conducted using only flushing with 1 M HCl and water. The samples that show unreasonably good performance were recorded directly after Fe containing samples, indicating that Fe traces remaining in the cell led to the observed activation. For comparison, Figure 8A shows two nearly indistinguishable CVs of a bare Ni foam tested before and after testing an Fe sample in the E-cell with sonication, indicating that it is generally possible to avoid contamination successfully in this system. This issue is very unlikely to have any measurable effect on samples that deliberately contain Fe, since the impurities in the cell are relatively small. For Fe free samples however this is significant and requires to test Fe free samples separately, such that a clean cell free of Fe impurities can be ensured.

5.3 Multi-parameter Optimization

Figures 8C-F show the reproducibility of results on the example of five Fe samples, tested at different points in the experimental campaign, with several other sample compositions in between, as well as the effect of doping with different elements on Ni catalysts, starting with the addition of one, two and four dopants.

When adding a single dopant (Figure 8D), Fe is clearly superior to the other elements.

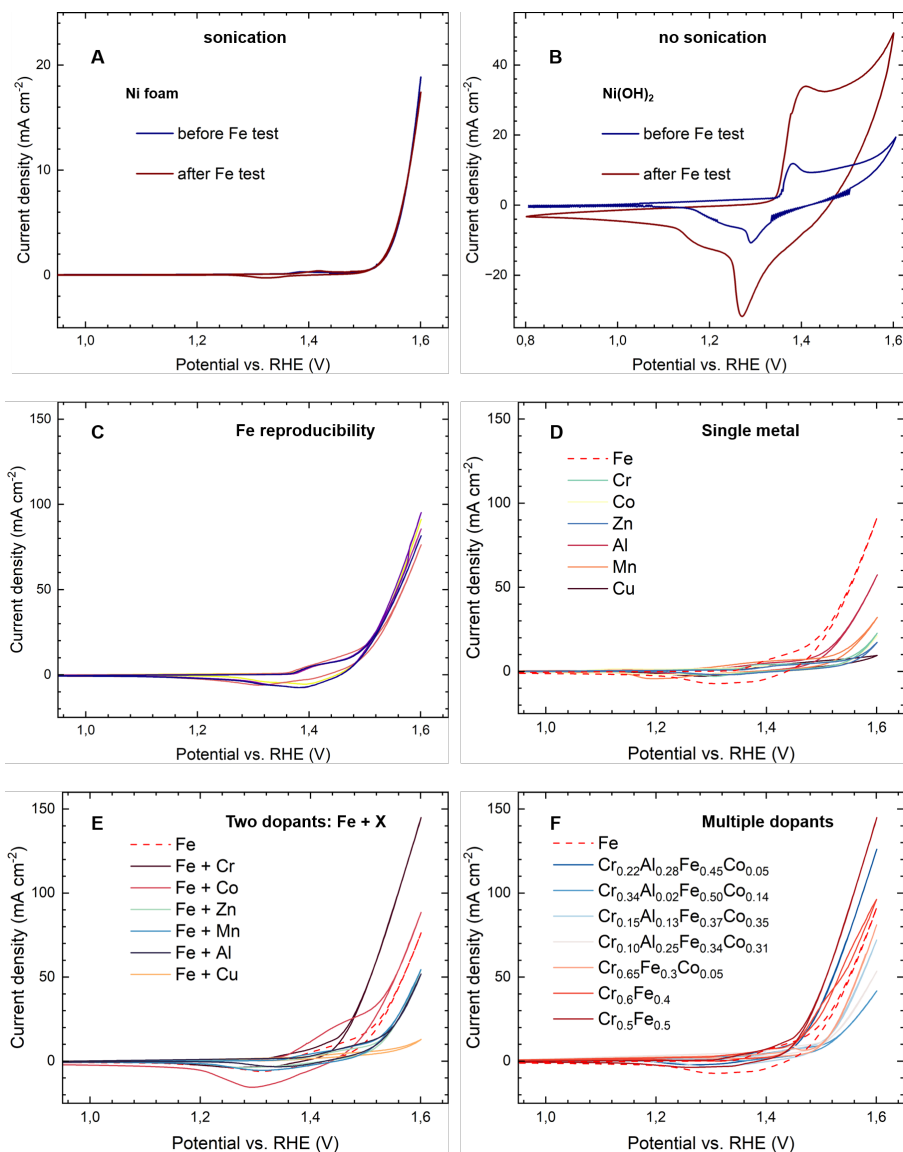


Figure 8. Bare Ni foam tested before and after testing an Fe sample with sonication during cleaning, showing no signs of contamination (A). For comparison, Ni sample tested in Fe contaminated environment and Fe free Ni sample (B). Reproducibility of results on the example of five Fe samples (C). Effect of adding one (D), two (E), and several dopants (F) to the Ni substrate. All CVs recorded with a scan rate of 10 mV s⁻¹.

Essentially the same picture arises when adding a secondary dopant in a 1:1 ratio, with Cr coming out on top with no serious competition (Figure 8E). To find the best doping ratio within a certain ternary compound (e.g. NiFeCr), one would probably iterate through a set of samples with varying ratios and try to recognise trends. Although time-consuming, this task can be accomplished manually, not least because a 3-dimensional phase space is visually conceivable for the researcher. In higher dimensional phase spaces, however, human intuition quickly fails, and finding local maxima becomes extremely difficult. Figure 8F illustrates this issue on the example of a five metal system (Ni + four dopants) with slightly changed doping levels, but massively different OER activities. It is not clear if the cause for the change in activity is the reduction of Al and Co content, the increase of Fe and Cr or a combination of both.

6 CONCLUSION AND OUTLOOK

In this work, we present an autonomous robotic platform for the synthesis, electrochemical investigation and machine-learning based optimization of multi-metal hydroxides for the alkaline OER. To the best of the authors knowledge, this is the first autonomous system for the development of alkaline water electrolysis catalysts reported in literature. The system enables the exploration of complex phase spaces that are inaccessible by means of conventional, manual approaches. In contrast to autonomous systems described in other fields of research, the compounds are tested under practical conditions in a beaker-type cell on Ni foam substrates. Including initial studies conducted during prototyping and for calibration, almost one thousand experiments have been conducted with this setup to date. Beyond pure optimization, we show that the obtained data quality and quantity in principle allows for analysis of redox features, charge-transfer processes and ECSA similar to conventional testing scenarios. We showcase excellent reproducibility on the example of NiFe LDH, and successfully reproduce a manual grid study that originally took several weeks to complete in little over one day. The trends that emerged in this study were the same as in the manual counterpart, confirming the feasibility of the platform for material screening and optimization. Several issues still remain, e.g. regarding the cleaning procedure, but appear to be of technical nature and generally solvable. First results of optimization in a four parameter phase space are presented, illustrating the sensitivity of the materials to small changes in the composition. This further suggests that there are likely complex compositions with improve activity outside of the scope of manual experimentation, which should be investigated in the future.

REFERENCES

- [1] S. A. Grigoriev, V. N. Fateev, D. G. Bessarabov, and P. Millet. Current status, research trends, and challenges in water electrolysis science and technology. *International Journal of Hydrogen Energy*, 45(49):26036–26058, 2020.
- [2] Martín David, Carlos Ocampo-Martínez, and Ricardo Sánchez-Peña. Advances in alkaline water electrolyzers: A review. *Journal of Energy Storage*, 23:392–403, jun 2019.
- [3] Xiaohong Xie, Lei Du, Litao Yan, Sehkyu Park, Yang Qiu, Joshua Sokolowski, Wei Wang, and Yuyan Shao. Oxygen Evolution Reaction in Alkaline Environment: Material Challenges and Solutions. *Advanced Functional Materials*, 32(21), 2022.
- [4] Gebrehiwet Abrham Gebreslase, Maria Victoria Martínez-Huerta, and Maria Jesus Lázaro. Recent progress on bimetallic NiCo and CoFe based electrocatalysts for alkaline oxygen evolution reaction: A review. *Journal of Energy Chemistry*, 67:101–137, apr 2022.
- [5] Yuan Feng, Haitao Yang, Xin Wang, Chaoquan Hu, Hailong Jing, and Jiaxin Cheng. Role of transition metals in catalyst designs for oxygen evolution reaction: A comprehensive review. *International Journal of Hydrogen Energy*, 47(41):17946–17970, may 2022.
- [6] Jamesh Mohammed-ibrahim and Harb Moussab. Tuning the electronic structure of the earth-abundant electrocatalysts for oxygen evolution reaction (OER) to achieve efficient alkaline water splitting – A review. *Journal of Energy Chemistry*, 56:299–342, may 2021.
- [7] Fabio Dionigi, Zhenhua Zeng, Ilya Sinev, Thomas Merzdorf, Siddharth Deshpande, Miguel Bernal Lopez, Sebastian Kunze, Ioannis Zegkinoglou, Hannes Sarodnik, Dingxin Fan, Arno Bergmann, Jakub Drnec, Jorge Ferreira de Araujo, Manuel Gliech, Detre Teschner, Jing Zhu, Wei Xue Li, Jeffrey Greeley, Beatriz Roldan Cuenya, and Peter Strasser. In-situ structure and catalytic mechanism of NiFe and CoFe layered double hydroxides during oxygen evolution. *Nature Communications*, 11(1), 2020.
- [8] Qiang Wang and Dermot O’Hare. Recent advances in the synthesis and application of layered double hydroxide (LDH) nanosheets. *Chemical Reviews*, 112(7):4124–4155, 2012.
- [9] Li Anne Cheah, G. V. Manohara, M. Mercedes Maroto-Valer, and Susana Garcia. Impact of Synthesis Method and Metal Salt Precursors on the CO₂ Adsorption Performance of Layered Double Hydroxides Derived Mixed Metal Oxides. *Frontiers in Energy Research*, 10(May):1–19, 2022.

- [10] Ge Gao, Zhi Zhu, Jia Zheng, Zhi Liu, Qiu Wang, and Yongsheng Yan. Ultrathin magnetic Mg-Al LDH photocatalyst for enhanced CO₂ reduction: Fabrication and mechanism. *Journal of Colloid and Interface Science*, 555:1–10, nov 2019.
- [11] Marco Etzi Collier Pascuzzi, Alex J.W. Man, Andrey Goryachev, Jan P. Hofmann, and Emiel J.M. Hensen. Investigation of the stability of NiFe-(oxy)hydroxide anodes in alkaline water electrolysis under industrially relevant conditions. *Catalysis Science and Technology*, 10(16):5593–5601, 2020.
- [12] Sarmad Iqbal, Bushra Safdar, Iftikhar Hussain, Kaili Zhang, and Christodoulos Chatzichristodoulou. Trends and Prospects of Bulk and Single-Atom Catalysts for the Oxygen Evolution Reaction. *Advanced Energy Materials*, 13(17), 2023.
- [13] Kai Yan, Todd Lafleur, Jiajue Chai, and Cody Jarvis. Facile synthesis of thin NiFe-layered double hydroxides nanosheets efficient for oxygen evolution. *Electrochemistry Communications*, 62:24–28, 2016.
- [14] Qiong Luo, Mingying Peng, Xuping Sun, Yonglan Luo, and Abdullah M. Asiri. Efficient electrochemical water splitting catalyzed by electrodeposited NiFe nanosheets film. *International Journal of Hydrogen Energy*, 41(21):8785–8792, jun 2016.
- [15] B M Hunter, W Hieringer, J R Winkler, H B Gray, and A M Mü. Effect of interlayer anions on [NiFe]-LDH nanosheet water oxidation activity. — *Energy Environ. Sci*, 9:1734, 2016.
- [16] Fabio Dionigi and Peter Strasser. NiFe-Based (Oxy)hydroxide Catalysts for Oxygen Evolution Reaction in Non-Acidic Electrolytes. *Advanced Energy Materials*, 6(23), 2016.
- [17] G. Młynarek, M. Paszkiewicz, and A. Radniecka. The effect of ferric ions on the behaviour of a nickelous hydroxide electrode. *Journal of Applied Electrochemistry*, 14(2):145–149, 1984.
- [18] Dennis A. Corrigan and Shyam P. Maheswari. Catalysis of the Oxygen Evolution Reaction By Trace Iron Impurities in Thin Film Nickel Oxide Electrodes. *Electrochemical Society Extended Abstracts*, 85-1:934–935, 1985.
- [19] Dennis A. Corrigan and Richard M. Bendert. Effect of Coprecipitated Metal Ions on the Electrochemistry of Nickel Hydroxide Thin Films: Cyclic Voltammetry in 1M KOH. *Journal of The Electrochemical Society*, 136(3):723–728, 1989.
- [20] Sengen Anantharaj, Subrata Kundu, and Suguru Noda. “The Fe Effect”: A review unveiling the critical roles of Fe in enhancing OER activity of Ni and Co based catalysts. *Nano Energy*, 80(February 2020):105514, 2021.
- [21] Shanshan Jiang, Yang Liu, Hao Qiu, Chao Su, and Zongping Shao. High Selectivity Electrocatalysts for Oxygen Evolution Reaction and Anti-Chlorine Corrosion Strategies in Seawater Splitting. *Catalysts*, 12(3):261, feb 2022.

- [22] Yuan Kong, Yi Wang, Wei Chu, and Zhongqing Liu. Tailoring surface and interface electronic structure of NiFe LDH via V doping for enhanced oxygen evolution reaction. *Journal of Alloys and Compounds*, 885:160929, dec 2021.
- [23] Mengzhou Yu, Jiqi Zheng, and Ming Guo. La-doped NiFe-LDH coupled with hierarchical vertically aligned MXene frameworks for efficient overall water splitting. *Journal of Energy Chemistry*, 70:472–479, jul 2022.
- [24] Gaiyun Zhao, Biao Wang, Qi Yan, and Xiaohong Xia. Mo-doping-assisted electrochemical transformation to generate CoFe LDH as the highly efficient electrocatalyst for overall water splitting. *Journal of Alloys and Compounds*, 902:163738, may 2022.
- [25] Jian Bao, Zhaolong Wang, Junfeng Xie, Li Xu, Fengcai Lei, Meili Guan, Yan Zhao, Yunpeng Huang, and Huaming Li. A ternary cobalt-molybdenum-vanadium layered double hydroxide nanosheet array as an efficient bifunctional electrocatalyst for overall water splitting †. *Chem. Commun*, 55:3521, 2019.
- [26] Yonghao Gan, Zhi Li, Ying Ye, Xiaoping Dai, Fei Nie, Xueli Yin, Ziteng Ren, Baoqiang Wu, Yihua Cao, Run Cai, Xin Zhang, and Weiyu Song. Doping Mo into NiFe LDH/NiSe Heterostructure to Enhance Oxygen Evolution Activity by Synergistically Facilitating Electronic Modulation and Surface Reconstruction. *ChemSusChem*, 15(20), 2022.
- [27] Mengjie Liu, Kyung Ah Min, Byungchan Han, and Lawrence Yoon Suk Lee. Interfacing or Doping? Role of Ce in Highly Promoted Water Oxidation of NiFe-Layered Double Hydroxide. *Advanced Energy Materials*, 11(33):1–11, 2021.
- [28] Xinxuan Duan, Pengsong Li, Daojin Zhou, Shiyuan Wang, Hai Liu, Zhaolei Wang, Xingheng Zhang, Guotao Yang, Zhuang Zhang, Guoying Tan, Yaping Li, Lijun Xu, Wen Liu, Zihao Xing, Yun Kuang, and Xiaoming Sun. Stabilizing single-atomic ruthenium by ferrous ion doped NiFe-LDH towards highly efficient and sustained water oxidation. *Chemical Engineering Journal*, 446:136962, oct 2022.
- [29] Enkhbayar Enkhtuvshin, Kang Min Kim, Young-Kwang Kim, Sungwook Mihn, So Jung Kim, Sun Young Jung, Nguyen Thi Thu Thao, Ghulam Ali, Muhammad Akbar, Kyung Yoon Chung, Keun Hwa Chae, Sukhyun Kang, Taeg Woo Lee, Hyung Giun Kim, Seunggun Choi, and HyukSu Han. Stabilizing oxygen intermediates on redox-flexible active sites in multimetallic Ni–Fe–Al–Co layered double hydroxide anodes for excellent alkaline and seawater electrolysis. *Journal of Materials Chemistry A*, 2021.
- [30] Fitri Nur Indah Sari, Gally Frenel, Alex Chinghuan Lee, Yan Jia Huang, Yen Hsun Su, and Jyh Ming Ting. Multi-high valence state metal doping in NiFe hydroxide toward superior oxygen evolution reaction activity. *Journal of Materials Chemistry*

- A, 11(6):2985–2995, 2023.
- [31] Rafael Gómez-Bombarelli, Jorge Aguilera-Iparraguirre, Timothy D. Hirzel, David Duvenaud, Dougal Maclaurin, Martin A. Blood-Forsythe, Hyun Sik Chae, Markus Einzinger, Dong Gwang Ha, Tony Wu, Georgios Markopoulos, Soonok Jeon, Hosuk Kang, Hiroshi Miyazaki, Masaki Numata, Sunghan Kim, Wenliang Huang, Seong Ik Hong, Marc Baldo, Ryan P. Adams, and Alán Aspuru-Guzik. Design of efficient molecular organic light-emitting diodes by a high-throughput virtual screening and experimental approach. *Nature Materials*, 15(10):1120–1127, 2016.
 - [32] Kisuk Kang, Ying Shirley Meng, Julien Bréger, Clare P. Grey, and Gerbrand Ceder. Electrodes with high power and high capacity for rechargeable lithium batteries. *Science*, 311(5763):977–980, 2006.
 - [33] Atsuto Seko, Atsushi Togo, and Isao Tanaka. Descriptors for machine learning of materials data. In *Nanoinformatics*, pages 3–23. Springer Nature, 2018.
 - [34] Haoxin Mai, Tu C. Le, Dehong Chen, David A. Winkler, and Rachel A. Caruso. Machine Learning for Electrocatalyst and Photocatalyst Design and Discovery. *Chemical Reviews*, 122(16):13478–13515, 2022.
 - [35] Gus L.W. Hart, Tim Mueller, Cormac Toher, and Stefano Curtarolo. Machine learning for alloys. *Nature Reviews Materials*, 6(8):730–755, 2021.
 - [36] Miao Zhong, Kevin Tran, Yimeng Min, Chuanhao Wang, Ziyun Wang, Cao Thang Dinh, Phil De Luna, Zongqian Yu, Armin Sedighian Rasouli, Peter Brodersen, Song Sun, Oleksandr Voznyy, Chih Shan Tan, Mikhail Askerka, Fanglin Che, Min Liu, Ali Seifitokaldani, Yuanjie Pang, Shen Chuan Lo, Alexander Ip, Zachary Ulissi, and Edward H. Sargent. Accelerated discovery of CO₂ electrocatalysts using active machine learning. *Nature*, 581(7807):178–183, 2020.
 - [37] Andrew F. Zahrt, Jeremy J. Henle, Brennan T. Rose, Yang Wang, William T. Darrow, and Scott E. Denmark. Prediction of higher-selectivity catalysts by computer-driven workflow and machine learning. *Science*, 363(6424), 2019.
 - [38] Teo Lombardo, Marc Duquesnoy, Hassna El-Bouysidy, Fabian Årén, Alfonso Gallo-Bueno, Peter Bjørn Jørgensen, Arghya Bhowmik, Arnaud Demortière, Elixabete Ayerbe, Francisco Alcaide, Marine Reynaud, Javier Carrasco, Alexis Grimaud, Chao Zhang, Tejs Vegge, Patrik Johansson, and Alejandro A. Franco. Artificial Intelligence Applied to Battery Research: Hype or Reality? *Chemical Reviews*, 122(12):10899–10969, 2022.
 - [39] James B. Gerken, Sarah E. Shaner, Robert C. Massé, Nicholas J. Porubsky, and Shannon S. Stahl. A survey of diverse earth abundant oxygen evolution electrocatalysts showing enhanced activity from Ni-Fe oxides containing a third metal. *Energy and Environmental Science*, 7(7):2376–2382, 2014.

- [40] Andrew Sparkes, Wayne Aubrey, Emma Byrne, Amanda Clare, Muhammed N. Khan, Maria Liakata, Magdalena Markham, Jem Rowland, Larisa N. Soldatova, Kenneth E. Whelan, Michael Young, and Ross D. King. Towards Robot Scientists for autonomous scientific discovery. *Automated Experimentation*, 2(1), 2010.
- [41] Ross D. King. Rise of the robo scientists. *Scientific American*, 304(1):73–77, 2011.
- [42] Hui Liu, Norbert Stoll, Steffen Junginger, and Kerstin Thurow. Mobile robot for life science automation. *International Journal of Advanced Robotic Systems*, 10:1–14, 2013.
- [43] Yunchao Xie, Kianoosh Sattari, Chi Zhang, and Jian Lin. Toward autonomous laboratories: Convergence of artificial intelligence and experimental automation. *Progress in Materials Science*, 132:101043, feb 2023.
- [44] Adarsh Dave, Jared Mitchell, Kirthevasan Kandasamy, Han Wang, Sven Burke, Biswajit Paria, Barnabás Póczos, Jay Whitacre, and Venkatasubramanian Viswanathan. Autonomous Discovery of Battery Electrolytes with Robotic Experimentation and Machine Learning. *Cell Reports Physical Science*, 1(12):100264, dec 2020.
- [45] Connor W. Coley, Natalie S. Eyke, and Klavs F. Jensen. Autonomous Discovery in the Chemical Sciences Part II: Outlook. *Angewandte Chemie - International Edition*, 59(52):23414–23436, 2020.
- [46] Connor W. Coley, Natalie S. Eyke, and Klavs F. Jensen. Autonomous Discovery in the Chemical Sciences Part I: Progress. *Angewandte Chemie - International Edition*, 59(51):22858–22893, 2020.
- [47] Katherine McCullough, Travis Williams, Kathleen Mingle, Pooyan Jamshidi, and Jochen Lauterbach. High-throughput experimentation meets artificial intelligence: A new pathway to catalyst discovery. *Physical Chemistry Chemical Physics*, 22(20):11174–11196, may 2020.
- [48] Martha M. Flores-Leonar, Luis M. Mejía-Mendoza, Andrés Aguilar-Granda, Benjamin Sanchez-Lengeling, Hermann Tribukait, Carlos Amador-Bedolla, and Alán Aspuru-Guzik. Materials Acceleration Platforms: On the way to autonomous experimentation. *Current Opinion in Green and Sustainable Chemistry*, 25:100370, oct 2020.
- [49] B. P. MacLeod, F. G.L. Parlane, T. D. Morrissey, F. Häse, L. M. Roch, K. E. Dettelbach, R. Moreira, L. P.E. Yunker, M. B. Rooney, J. R. Deeth, V. Lai, G. J. Ng, H. Situ, R. H. Zhang, M. S. Elliott, T. H. Haley, D. J. Dvorak, A. Aspuru-Guzik, J. E. Hein, and C. P. Berlinguette. Self-driving laboratory for accelerated discovery of thin-film materials. *Science Advances*, 6(20), 2020.
- [50] Benjamin Burger, Phillip M. Maffettone, Vladimir V. Gusev, Catherine M. Aitchi-

- son, Yang Bai, Xiaoyan Wang, Xiaobo Li, Ben M. Alston, Buyi Li, Rob Clowes, Nicola Rankin, Brandon Harris, Reiner Sebastian Sprick, and Andrew I. Cooper. A mobile robotic chemist. *Nature*, 583(7815):237–241, 2020.
- [51] Hongying Li, Xueliang Wang, Tao Wang, and Fengxia Xiao. A facile, green and time-saving method to prepare partially crystalline NiFe layered double hydroxide nanosheets on nickel foam for superior OER catalysis. *Journal of Alloys and Compounds*, 844:156224, 2020.
- [52] Seyedali Mirjalili. Dragonfly algorithm: a new meta-heuristic optimization technique for solving single-objective, discrete, and multi-objective problems. *Neural Computing and Applications*, 27(4):1053–1073, 2016.
- [53] Pengcheng Xu, Xiaobo Ji, Minjie Li, and Wencong Lu. Small data machine learning in materials science. *npj Computational Materials*, 9(1):42, 2023.

5.3 Experimental obstacles and learnings

While the workflow of the autonomous experimentation platform described in Chapter 5 seems very simple at first glance, the system consists of a large number of individual components: Among other things, there are 17 pumps (8 syringe and 9 peristaltic), temperature and humidity sensors, safety triggers, 12 different stock solutions, 75 easily damaged Ni foams, 152 vials, an intricate electrochemical test cell and a potentiostat - all of this in addition to the actual robotic platform. Over time,



Figure 5.9. The autonomous experimentation platform.

various chemicals, including both bases and acids, are handled, leading to the release of fumes or potential spills if something doesn't go according to plan. Despite the system being placed in a fume hood, all of its components are consistently exposed to a harsh environment. This was evident, for example, in the robot arm and carousel axes, which exhibited clear signs of corrosion.

Many system components are subject to possible human error such as misalignment

(e.g. samples, vials, caps, hoses, or the reference electrode), incorrect pretreatment, insufficient cleaning or empty stock solutions. Additionally, there are possible points of failure on the software side of the experiment: Time-out errors, compiler crashes, general code bugs, corrupted files, firmware incompatibilities and accumulating robot axis alignment errors have all been experienced during the this project. One could argue that while the individual factors might be different, a manual experiment is subject to a similar amount of problems. The key difference between manual and autonomous experimentation is that the human researcher can adapt to unexpected events (such as empty stock solutions, damaged substrates, misaligned vials etc.), while the autonomous system is deterministic: Every single event¹ that is *unexpected*, will either lead to the failure of the experiment or compromised data, because the system will not address the issue in any way. On the other hand, accounting for every possible problem in a deterministic system is not achievable.

In our case, we attempted to design the system as resilient as possible with respect to the failure modes we expected

to be relevant and the ones we ran into along the way. While ultimately the system can be run successfully like this, it is easy to fall into a rabbit hole in which the solution to one problem creates multiple new problems itself. For example, it showed that whenever the system was shut down, the syringe pump valves would allow air into the tubing, which resulted in an incorrect dispensed volume in the first subsequent experiments. This in turn would result in a false attribution of measurement results to metal composition, which made it necessary to prime the pumps when starting the system, prior to any experiments. However, any of the available solutions for priming came with its own set of problems, as Figure 5.11 exemplifies.



Figure 5.10. Assortment of (mostly 3D-printed) prototypes of sample holders, cell bases, lids and terminals, racks, caps, grippers, vials and others.

¹that has a tangible effect on the outcome of the experiment, or the system itself

The design and implementation of the project was based on trial and error as, to the best of the authors' knowledge, there are currently no comparable systems reported in the literature. Consequently, many design concepts were tried and discarded, dozens of prototypes designed and 3D printed (see Figure 5.10). The alternative could be to implement advanced machine learning techniques like computer vision as a means to give the autonomous system some form of situational awareness. In that case, it might be possible to avoid addressing individual failure modes one by one. This however comes at the price of incomparably higher complexity in the area of software development.

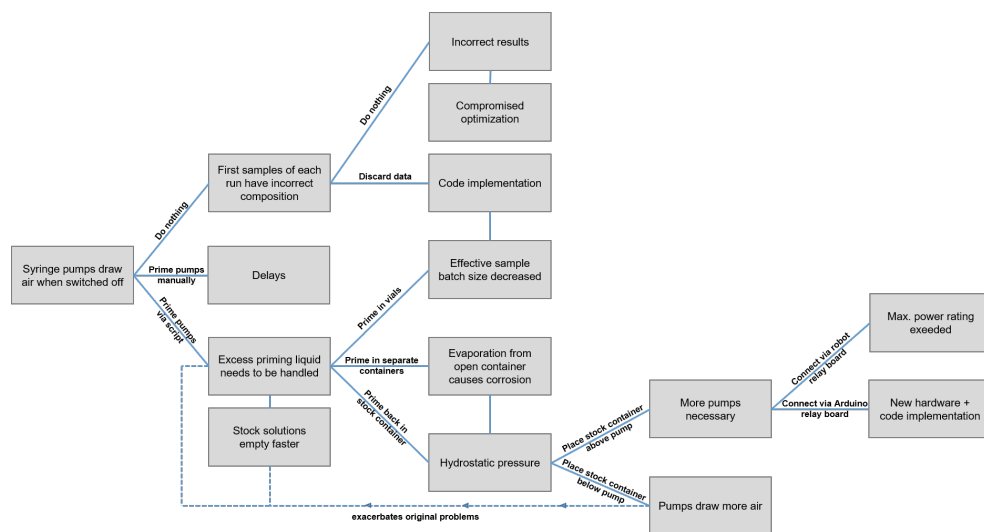


Figure 5.11. Decision tree based on a seemingly simply technical issue, illustrating the complexity of fail-proofing autonomous lab systems.

Design principles

The consideration of all these factors makes the experiment complex as is, despite the comparatively simple process it attempts to autonomize. It also implies that the requirements for autonomous experiments differ significantly from those for manual experiments in some respects. Based on our experiences to date, some general design principles for autonomous experimentation in a lab setting can be derived that might be useful for later projects:

Suitability Not every type of experiment or synthesis route are equally suitable for high-throughput applications and automation. Smaller sample sizes and liquid volumes are highly preferable, since they will reduce running costs and the effort needed for restocking, while also helping to increase the throughput. Precise synthesis methods, for which e.g. mass loading is well controlled, help to increase comparability between samples. The electrodeposition synthesis described in Chapter 6 is a good alternative example for this. On the other hand, certain pieces of knowledge about the sample might be dispensable for sake of increased throughput or simplicity: structural properties like crystal phase, exact composition, oxidation state and other properties can always be analysed manually for select samples of interest outside the bounds of the autonomous system.

Simplicity Once the experimental concept has been determined, the highest priority in the development of an autonomous experiment should be the simplicity of the workflow and the used instrumentation. Choosing the least complex experimental setup which allows obtaining the data quality and quantity needed for the specific project will help reduce the number of potential failure modes (which tend to get out of hand quickly, as visualized in Figure 5.11) and as a consequence the number of design decisions that have to be made further down the road. The implementation of the mixing of metal precursors in our project can be used as an example: the vials could be replaced by stationary, flushable mixing reactors similar to the E-cell, in which both dipping steps are carried out. A separate cell can be used for samples containing Fe, since it is the only cations known to have a significant effect on the OER activity even in ppm or ppb concentrations. In such a design, not only all vials, but also the vial clamp and the stepped gripper design are not necessary, reducing system complexity drastically, and freeing up the majority of space operable by the robot arm. In return, only 6 reliable and cheap peristaltic pumps (HCl, water and suction for cleaning of each cell) are added to the system.

Reliability When both the experimental concept and the corresponding workflow are decided on, the next priority should be to design the implementation with maximum reliability in mind. Unlike in manual experiments, every piece of equipment has to work as expected every single time it is used for an experiment to achieve usable results. Whenever possible, commercial instruments

that have been tried and tested should be preferred over custom parts. Everything that is in contact with corrosive chemicals or otherwise subject to wear should be designed to withstand those conditions for thousands of iterations without failure

CHAPTER 6

Machine Learning Guided Development of High-Performance Nano-Structured Nickel Electrodes for Alkaline Water Electrolysis

6.1 Introduction

The work described in the following manuscript was conducted in order to obtain high surface area Ni electrodes for the alkaline HER catalysis by means of an optimized electrodeposition method, in which deposition time, current density, temperature

and ligand concentration were varied. This was achieved by integrating a machine learning algorithm into a regular experimental procedure via a human-in-the-loop approach. Unlike the project described in Chapter 5, no complex, automated test setup was used, but rather ordinary instruments found in most chemistry labs. Remarkable results were achieved after only a short period of time, which encouraged us to undertake further experiments within a more complex parameter space.

This approach is of particular interest since it is achievable for the majority of researchers, since no expensive hardware or expert knowledge on machine learning techniques is necessary. The potential field of applications is very broad, since especially in the material sciences, time-consuming and laborious screening studies can often hardly be avoided, due to complex phase spaces and non intuitive relationships between synthesis parameters, resulting structures and performance metrics. We demonstrate that with this low-entry approach, optimization problems in the Lab can be efficiently tackled.

The work summarised in this manuscript was conducted by several participants in the context of special courses and a master's thesis. Veronica Humlebæk Jensen carried out the majority of experiments and data analysis of the three parameter study as part of a special course and her master's thesis under the supervision of Prof. Ragnar Kiebach and co-supervision of Mikkel R. Kraglund and Argyha Bowmik. She wrote the results section of the manuscript and provided all graphs, figures and tables. Sofie Skov, Emilie Jakobsen and Emil Howaldt Christiansen conducted the experiments on the four parameter study. Jonas Busk implemented the baysian optimization in the experimental workflow and wrote the corresponding section of the manuscript. The author of this thesis acted as the lab-supervisor, coordinated and guided the experimental work, provided support with data analysis and interpretation and carried out XPS measurements. He wrote the introduction, discussion and conclusion of the manuscript, as well as parts of the results.

6.2 Manuscript draft

Machine Learning Guided Development of High-Performance Nano-Structured Nickel Electrodes for Alkaline Water Electrolysis

Veronica Humlebæk Jensen^a, Enzo Raffaele Moretti^a, Jonas Busk^a, Emil Howaldt Christiansen^a, Sofie Marie Skov^a, Emilie Jacobsen^a, Mikkel Rykær Kraglund^a, Arghya Bhowmik^a, Ragnar Kiebach^a

a. Department of Energy Conversion and Storage, Technical University of Denmark, Lyngby Campus, Anker Engelunds Vej, 2800 Denmark

Corresponding authors: Ragnar Kiebach (woki@dtu.dk), Enzo Raffaele Moretti (enzomo@web.de)

Abstract:

Utilizing a human in the loop Bayesian optimisation paradigm based on Gaussian process regression, we optimized an Ni electrodeposition method to synthesize nano-structured, high-performance hydrogen evolution reaction electrodes. Via exploration-exploitation stages, the synthesis process variables current density, temperature, ligand concentration and deposition time are optimized influencing the deposition layer morphology and, consequently, hydrogen evolution reaction activity. The resulting structures range from micrometer-sized, star-shaped features to nano-sized sandpaper-like structures with very high specific surface areas and good hydrogen evolution reaction activity. Using the overpotential at 10 mA cm⁻² as the figure of merit, hydrogen evolution reaction overpotentials as low as -117 mV were reached, approaching the best known technical high surface area electrodes (e.g. Raney Ni). This is achieved with considerably fewer experiments than what would have been necessary with a linear grid search, as the machine learning model could capture the unintuitive interdependencies of the synthesis variables.

Keywords: water electrolysis, nano catalyst, hydrogen evolution reaction, bayesian optimization, technical electrodes, human in the loop

1 Introduction

In order to reduce global carbon emission it is not enough to switch from fossil fuels to renewable energy sources. The green transition will rely heavily on the availability of green hydrogen as an energy carrier. Both for energy storage applications, to counteract the inherently intermittent nature of wind and solar power, but also as a chemical precursor for e-fuels and to decarbonize industry sectors such as cement and steel production. [1], [2]

To reach the global goal of carbon neutrality, the demand for green hydrogen will increase substantially. The International Energy Agency's Net Zero Emissions Scenario for 2050 assumes that a total installed electrolyser capacity of 850 GW by 2030 and 3600 GW by 2050 will be needed - a roughly 7000-fold increase in less than three decades from the 0.5 GW that were operational by the end of 2021. [3] This implies that low cost materials, simple fabrication methods and TWh scalability are hard requirements for the industrial application of any new technology in this field. Irrespective of this, novel electrolyzers also need to operate more efficiently than current systems in order to be economically feasible. Highly active catalyst materials comprised of abundant elements present a pathway to achieve these objectives.

Alkaline water electrolysis (AWE) is the most mature commercialized electrolysis technology available. Nevertheless, AWE systems still struggle with corrosion and low operating current densities. [4]–[6] For the hydrogen evolution reaction (HER), noble metals such as platinum show good catalytic performance but remain unsuitable at large and industrial scales due to their prohibitive cost and scarcity. [5] Nickel (Ni) on the other hand, is relatively inexpensive, earth abundant, has been studied widely as an alkaline electrolysis catalyst and is often used in commercial electrolyzers due to its decent catalytic activity and stability in alkaline media. [5], [7] Its performance as a HER catalyst can be further improved by secondary elements such as cobalt and molybdenum or by increasing the amount of catalytic active sites via high surface area secondary Ni structures. [7] Raney-type Ni is a

well-known example of high surface area Ni catalysts with outstanding performance [8] yet is difficult to synthesise and suffers from deactivation under intermittent operation.

Electrodeposition is a facile, scalable, fast and in-expensive deposition method [5], [9] proven to be capable of creating different secondary Ni structures. [5], [10]–[14] The structure deposited through electrodeposition depends strongly on plating parameters such as current density, deposition time, solution temperature, concentration and pH, which creates a large parameter space. Developing well performing secondary Ni structures is a challenging and time consuming process, requiring numerous experiments guided by intuition, trials and errors. One way of speeding up such parameter optimization task is by applying machine learning (ML) techniques. ML models have been used to accelerate the computational communities discovery of energy materials, for example in batteries, solar cells and catalysts. [15]–[18] Being a data driven method, such an approach relies on the controlled generation of high fidelity large volume computational data. It is much more challenging with experimental data sources due to small data regime and noisy observations. Recently ML based “design of experiments” for materials optimization has increasingly attracted interest in experimental materials synthesis community from an accelerated discovery perspective as high throughput experiments become accessible. [19], [20]

Experimental search campaigns with AI guided design of experiments with a closed-loop feedback can outperform human intuition driven drastically as cognitive limitations of human researchers impede the optimal exploration of complex parameter spaces. Recent breakthroughs in AI driven experiment design have focused on organic reaction planning and optimization [21]–[23] but a handful of recent articles demonstrate the usefulness of AI guided optimization towards synthesis of solid state materials [24]–[27] as well.

In this work, we showcase the benefits of applying AI guided iterative optimization even outside of autonomous labs, where Ni based electrodes for the alkaline HER are optimized. Guided by an exploration-exploitation scheme we vary the process parameters of the Ni electrodeposition to

optimize the electrochemically active surface area (ECSA), using the HER overpotential at a given current density as the figure of merit for the underlying Gaussian process regression model. The Bayesian optimization in an iterative approach helps us choose the most promising parameter sets for the next synthesis batch based on the expected value of overpotential and the related uncertainty. This allowed us to obtain large improvements in catalytic performance and HER activities approaching the Raney-Ni domain in a complex search space with reduced experimental effort.

2. Material and Methods

2.1 Experimental

2.1.1 Materials

KOH (ACS reagent, $\geq 85\%$), $\text{NiCl}_2 \cdot 6\text{H}_2\text{O}$ ($\geq 98\%$), H_3BO_3 (ACS Reagent $\geq 99.8\%$), ethylenediamine dihydrochloride (EDA, 98%) and HCl (37 wt %) were supplied by Sigma Aldrich, while NH_4OH (25 %) was supplied by Alfa Aesar. Perforated Ni plate with a $300\ \mu\text{m}$ thickness, 1 mm hole size and 0.7 mm hole spacing was used as substrate. Ni plates (99.95 %) were supplied by Alfa Aesar.

2.1.2 Electrode Preparation

As electrode substrate, perforated Ni plates were cut to samples with a size of $2.5\ \text{cm} \cdot 2.5\ \text{cm}$. To ensure a clean and smooth surface, the samples went through a three step pre-treatment process. To remove organic substances the substrate was ultrasonicated in an acetone-ethanol (1:1) solution for 30 min whereafter the substrate was submerged in 3 M HCl for 30 s to remove Ni oxides. Lastly, to ensure good adhesion, a Ni coating was deposited. Between each step the substrate was rinsed with deionized water.

To deposit the nanostructured Ni we adopted a process from Zhou et al., [28] using a solution composed of $\text{NiCl}_2 \cdot 6\text{H}_2\text{O}$, H_3BO_3 and ethylenediamine dihydrochloride (EDA) as shown in Table 2. The reactants were dissolved in deionized water by stirring the solution while heating the solution slowly to $65\ ^\circ\text{C}$. Once the temperature had stabilized the pH was adjusted to 4 by dropwise addition of 10 % NH_4OH . To ensure even deposition on both sides of the substrate, two $10\ \text{cm} \cdot 2\ \text{cm} \cdot 0.16\ \text{cm}$ Ni plate

pieces were used as anodes. The exposed area of the anodes was limited to 2 cm · 2 cm with polyester tape (1280, 3M), while the distance to the Ni substrate was 3 cm (see step 1 in Figure 1). A wide neck bottle with a total solution volume of ca. 550ml was used as the synthesis reactor. The reactor was placed in a heated water bath on a hot plate for improved temperature stability. Current was supplied by an Elektro-Automatik EA-PS 5040-40A power supply, by connecting the electrodes with crocodile clamps. The deposition was started ca. 1 hour after the temperature had reached the target temperature by applying a constant current for a specified time. Detailed operating conditions are shown in Table 1.

Table 1: The composition and operating condition intervals of the solution used for electrodepositing nano-structured Ni.

Bath composition	Concentration
NiCl ₂ ·6H ₂ O	200 g L ⁻¹
H ₃ BO ₃	25 g L ⁻¹
EDA	200 g L ⁻¹
10% NH ₄ OH	-
Operating conditions	Value
Current density	4-160 mA cm ⁻²
Temperature	20-65 °C
Time	2-64 min
pH	4.0
Anodes	2 cm · 2 cm · 0.16 cm Ni
Stirring	60 rpm

The electrodeposition solution was reused for multiple samples. To ensure reproducibility the solution stability was monitored by synthesising control samples on a regular basis. For more information on the solution stability see Figure S1 in the supplementary information (SI).

2.1.3 Electrochemical characterization

The electrochemical measurements were conducted using a conventional three electrode setup connected to a Gamry Reference 600 Potentiostat. 1 M KOH was used as an electrolyte, a 2.5 cm · 2.5 cm perforated Ni plate as counter electrode and a reversible hydrogen electrode (RHE, Gaskatel mini-HydroFlex) as a reference electrode.

Before testing, the electrodes were preconditioned by potential sweeps from 200 to -400 mV vs. RHE (5x) using a scan rate of 20 mV s⁻¹.

Subsequently, 5 cyclic voltammetry (CV) scans were recorded in a region from +85 to -40 mV vs. RHE at different scan rates (10, 20, 50, 75 and 100 mV s⁻¹) to estimate the double layer capacitance. For each scan rate the respective charging current (i_c) is determined in a linear region according to Equation 1:

$$i_c = \sum_{n=1}^N \frac{1}{N} \left(\frac{|i_n^{forward} - i_n^{backward}|}{2} \right)$$

Where n are given datapoints across the linear region and N the total amount of datapoints. Plotting the scan rate vs. charging current yields a straight line with a slope equal to the specific double layer capacitance (C_{dl}), which is directly proportional to the electrochemical surface area (ECSA) and by association the roughness factor (R_f).

$$ECSA = A_{geo} \frac{C_{dl}}{C_s} = A_{geo} R_f$$

Where A_{geo} is the geometrical area of the electrode and C_s the specific capacitance, which according to P. Connor et al. [29] can be estimated to 20 μF cm⁻² for metallic surfaces.

The solution resistance was estimated using electrochemical impedance spectroscopy (EIS) performed at open circuit potential from 10⁻⁵-1 Hz using an AC amplitude of 10 mV, and later used for IR compensation (95 %).

To evaluate the electrode performance linear sweep voltammetry (LSV) was conducted using a scan rate of 1 mV s⁻¹ in the range 200 to -400 mV vs. RHE. From the compensated LSV curves the overpotential at 10 mA cm⁻² (η_{10}) was extracted.

2.1.4 Physical characterization

Images of the electrodeposited microstructure were acquired using a high resolution scanning electron microscope (SEM, Zeiss Merlin). X-ray photoelectron spectroscopy (XPS) was recorded with a Thermo Fischer Scientific ESCALAB 250Xi.

2.2 Machine Learning Methods

To guide the experiment towards optimal input parameters, we apply a human-in-the-loop Bayesian optimization (BO) approach. A Gaussian process (GP) regression model with the squared exponential covariance function (aka. RBF kernel) [30] is fitted with previous observations of the synthesis parameters and the corresponding output of interest. Given a good fit of the data, the GP model can provide mean (μ_{GP}) and uncertainty (σ_{GP}) predictions of the output for unobserved sets of synthesis parameters \mathbf{x} . These predictions can be used to identify new synthesis parameters that optimize the output by evaluating an acquisition function (f_{acq}) computed as μ_{GP} plus σ_{GP} , which is similar to the widely used GP-UCB algorithm [31]:

$$f_{acq}(\mathbf{x}) = \mu_{GP}(\mathbf{x}) + \sigma_{GP}(\mathbf{x})$$

Where typical BO algorithms are often designed to automatically identify a single set of input parameters with maximum potential, we instead apply a human-in-the-loop approach where a researcher uses a visualization of the f_{acq} to select a batch of new and interesting synthesis parameters (step 4 and 5 in Figure 1). This enables the selection of multiple sets of inputs in every iteration that are both diverse and interesting. Consequently, this allows the researcher to perform multiple lab experiments in each iteration, which is also more practical. For simplicity a grid size of 1 was used.

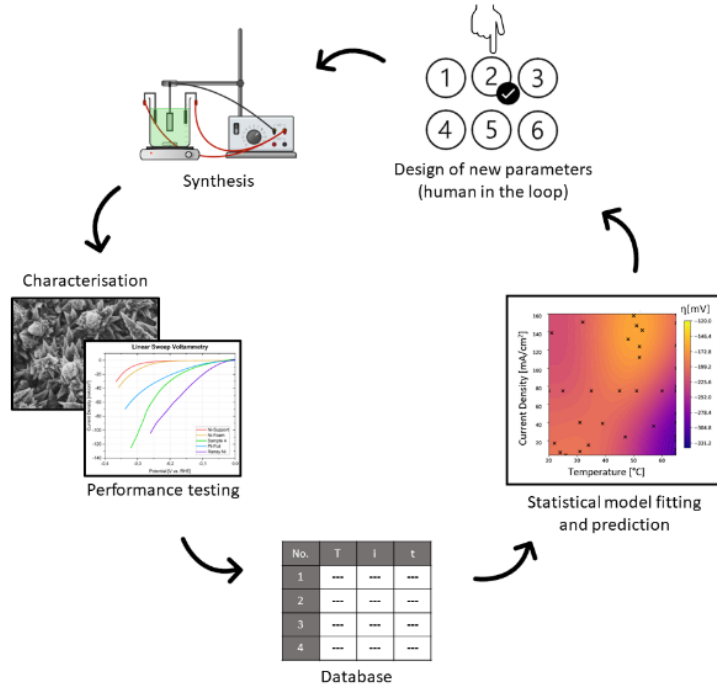


Figure 1: The optimization process can be described by an iterative loop of five steps. (1) Electrodes are synthesized in batches of 5-6 according to section 2.1.2. (2) Electrodes are tested and characterized using the method described in section 2.1.3 and 2.1.4. (3) The used synthesis parameters and performance metric (η at 10 mA cm^{-2}) are fed into a database. (4) Bayesian optimization, including a sensitivity analysis, is conducted using the database, resulting in a heat map of mean predicted overpotentials for any given combination of synthesis parameters. (5) Synthesis parameters for next batch are chosen manually based on the heat map (human in the loop). The drawing of the setup has been created with Chemix (<https://chemix.org>).

2.2.1 Sensitivity Analysis

Additionally, the fitted GP regression model can be utilized to identify the most important synthesis parameters by performing a global sensitivity analysis (SA). In this context, the input parameter sensitivity can be defined as the expected change of the output as a function of the input parameter [32]. We can compute this quantity empirically for each input parameter d with the GP as the mean squared derivative of the predicted output over a set of query points \mathbf{x}_i :

$$s_d^2(\mathbf{x}) = \frac{1}{N} \sum_{i=1}^N \left(\frac{\partial \mu_{GP}(\mathbf{x}_i)}{\partial x_{i,d}} \right)^2$$

The derivative in the above expression can be computed analytically or with automatic differentiation for a GP using the squared exponential covariance function. To enable direct comparison of input

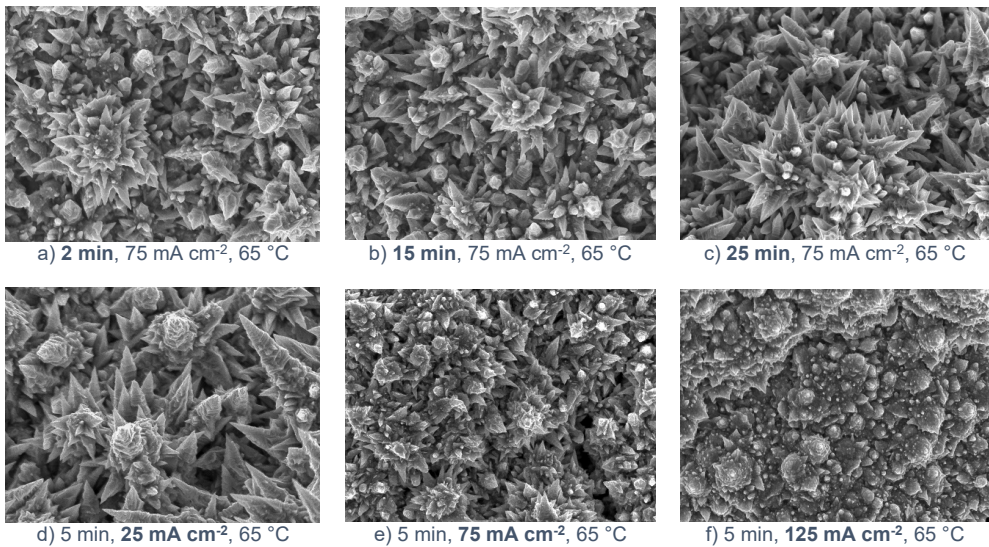
parameters with different scales, the inputs are normalized. In visual presentations of the sensitivities, we plot the square root of the sensitivity s_d .

3 Results

3.1 Linear Grid Study

Before applying AI guided optimization a linear grid study was conducted, where all but one parameter was kept constant. This to investigate how temperature (T), current density (i) and deposition time (t) affect the deposited nanostructure and its electrochemical performance individually and to establish a training data set for the optimization algorithm. For this study the parameter space was limited to cover 2-64 min, 5-160 mA cm⁻² and 20-65 °C. A t of 5 min, i of 75 mA cm⁻² and a T of 65 °C was used as standard parameters.

Figure 2 (a-c) shows that the microstructure visually does not vary as function of t . On the other hand, the i and T changes the microstructure significantly as shown in Figure 2 (d-f) and (g-i), respectively. At low current densities long spikes can be observed that become shorter and less pronounced when increasing the i . At low T the microstructure appears flat, a structure which coarsens with increasing T , until spikes start to form above 60 °C.



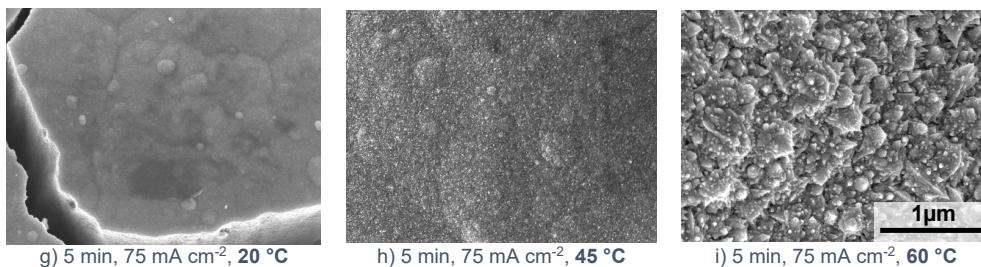


Figure 2: SEM images illustrating how the synthesis parameters; t (a-c), i (d-f) and T (g-i) changes the deposited microstructure. From a-c the microstructure visually does not change suggesting that t only creates a thicker layer. From d-f the spike length decreases with increasing i , while the microstructure from g-i changes drastically from almost flat and sandpaper-like at low and intermediate T to spiky at high T .

According to Figure 2 only two out of three investigated synthesis parameters change the deposited microstructure. It was therefore expected to observe changes in the electrochemical performance for variations in i and T . As shown in Figure 3, t and i changes the electrochemical performance significantly, while T , even though it changes the microstructure the most, does not affect the electrochemical performance much. For reference a bare perforated Ni plate on average requires an η_{10} of -321 mV, showing that almost all structures deposited in this study improve the substrates performance.

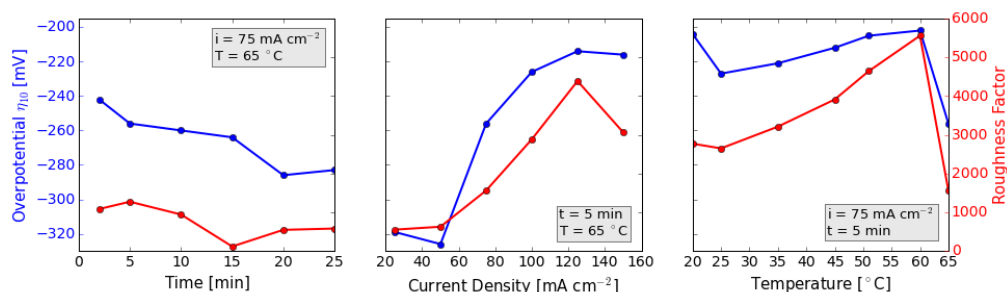


Figure 3: η_{10} (blue) and R_f (red) as function of t , i and T . With the chosen parameters the i appears to be the most sensitive synthesis parameter, followed by time and T . η_{10} generally decreases with increasing R_f .

Improvements in performance seen in Figure 3 scale with the measured R_f , indicating that the variations arise due to a change in active surface area.

3.2 Optimization

To make good predictions concerning the synthesis parameters, the training data must be large and randomly spread across the search space. Initially, the linear grid study data served as training data,

however, as shown in Figure S2, it was based on a linear search grid and thus there are many underrepresented areas of the search space, inducing a high σ_{GP} . Additional samples were therefore made using randomised parameters, creating a dataset with 31 samples significantly lowering σ_{GP} . Subsequently, 3 iterations of the Bayesian Optimisation (BO) loop were performed.

After fitting a GP regression model to the training data in step 4 of the BO loop (see Figure 1) a sensitivity analysis was conducted, to investigate how the μ_{GP} of η_{10} changes as function of either T , i or t (see Figure S3). Already the first iteration revealed that the mean η_{10} prediction only depends on two out of three investigated parameters: i and T . Since these two parameters were dominant, the optimisation problem reduced from a three- to two-dimensional problem. It was chosen to keep varying t randomly for the following iterations, however, since no time-sensitivity was found the t range was reduced after each iteration for practical reasons. This is a surprising finding and counter-intuitive, as one would expect the coating thickness to vary with t , and therefore also the availability of surface area obtained from porous coatings. For validation of this, sample 4 was synthesized again while reducing t from 30 min to 5 min, yielding practically identical results (see Figure S4).

Figure 4 shows heat maps of μ_{GP} and σ_{GP} , as well as f_{acc} . Two distinct areas with lower predicted η_{10} are found in all three iterations (brighter colours), centred approximately around (140 mA cm⁻², 55° C) and (< 10 mA cm⁻², 25° C). As the number of iterations and samples in the training data increases the model changes and σ_{GP} decreases. σ_{GP} for the first iteration is lowest around parameters frequently used in the linear grid study (75 mA cm⁻² and 65° C), and does not change significantly after iteration 2, indicating that a confident model has been established.

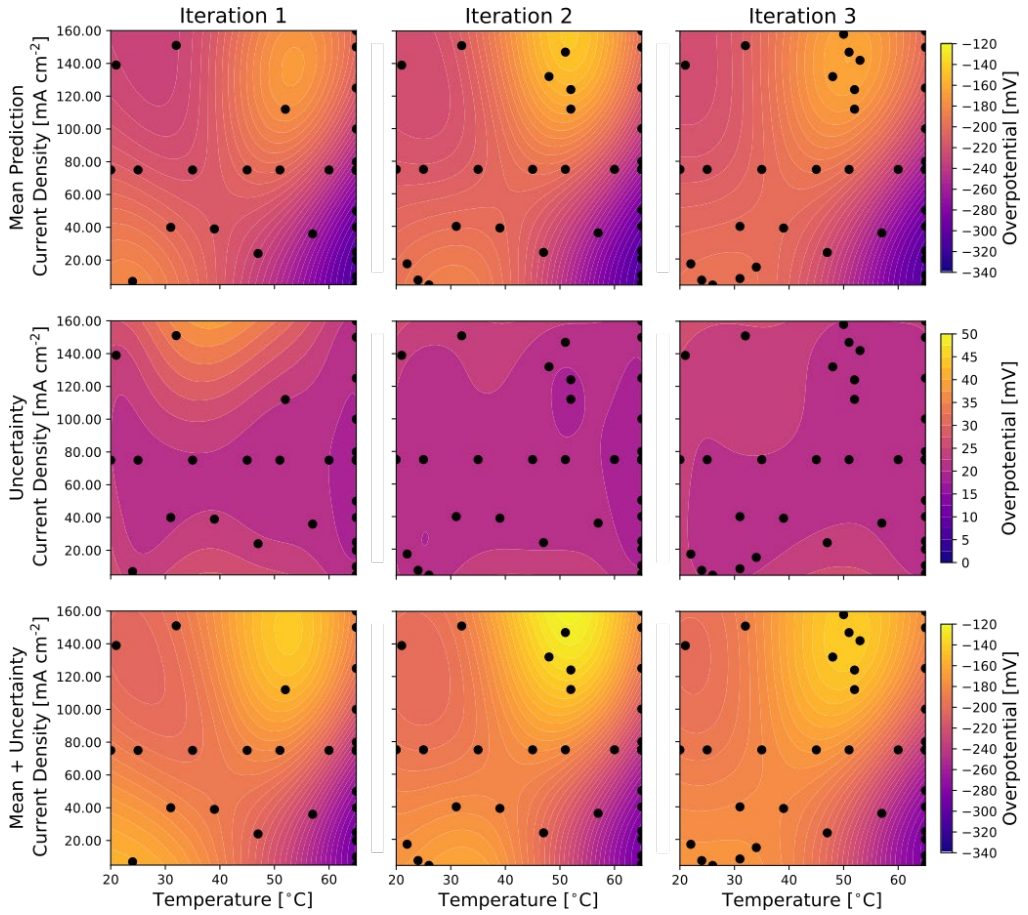


Figure 4: Illustration of the established μ_{GP} , σ_{GP} and a plot of f_{acq} , the ladder used to identify promising synthesis parameters. The model is based on known data points (31, 36 and 40 data points for iteration 1, 2 and 3 respectively) and shows the predicted η_{10} as function of T and i . Brighter colors indicate a low η_{10} and thus a good electrode performance. The figure shows that the prediction changes slightly and that the uncertainty is lowered with increasing number of iterations and samples.

Throughout iteration 1 and 2 exploration and exploitation were conducted, while the area with the lowest η_{10} were exploited in the third iteration. The results (synthesis parameters, η_{10} , R_f) of all three iterations are summarized in Table 2.

Iter.	No.	Synthesis Parameters			η_{10} [mV]	R_f
		T [°C]	i [mA cm ⁻²]	t [min]		
1	1	22	17	23	-210	3684
	2	26	4	39	-194	4428
	3	48	132	16	-168	7635
	4	51	147	30	-129	11836
	5	52	124	26	-144	5645
2	6	31	8	11	-220	3499

	7	34	15	24	-183	7903
	8	50	158	17	-180	6466
	9	53	142	8	-191	5249
	10	55	152	15	-180	5269
3	11	48	143	10	-166	7381
	12	49	126	4	-222	7513
	13	50	140	3	-241	3466
	14	51	146	7	-169	9358
	15	52	136	12	-178	6411
	16	52	170	6	-212	5061
	17	53	155	8	-211	4544

Table 2: Complete list of all the samples synthesized during the 3 iterations of the BO loop. In the table the measured η_{10} and R_f has been included as well.

As a general rule, samples synthesized with parameters in proximity to the μ_{GP} optima show the lowest η_{10} , indicating good agreement of experiment and prediction model.

Sample 4 showed the best performance in this study with $\eta_{10} = -129 \text{ mV}$. As expected, it also shows the highest R_f value (11836), even though there is essentially no structuring visible in the SEM image in Figure 5. This indicates that the porous, deposited layer exhibits features in the nanometer range, below the resolution limit of the microscope.

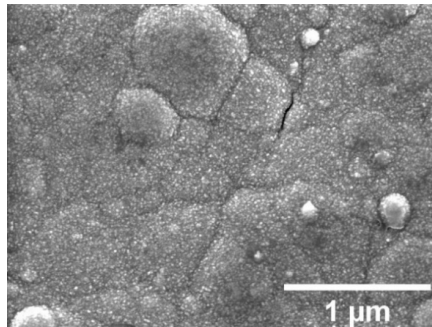


Figure 5: SEM image of sample 4's surface showing rough sandpaper-like features, which are hard to resolve further by SEM.

In Figure 6 the LSV curves of the best sample (sample 4, green) are compared to LSV curves of perforated Ni plate substrate, Ni foam, Pt-foil and Raney Ni (on perforated Ni plate). Sample 4 outperforms all materials except Raney Ni. As higher current densities are reached, the sample approaches the Raney Ni domain.

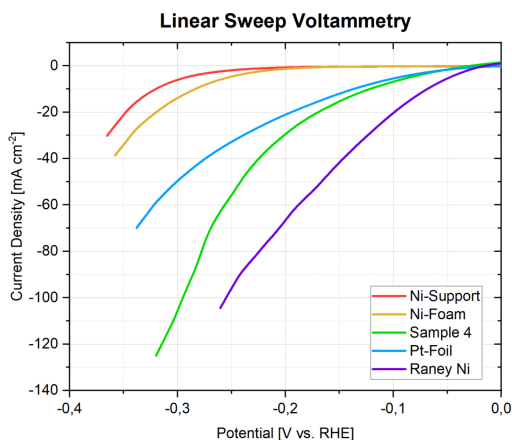


Figure 6: Smoothened LSV curves for the substrate (red), Ni foam (yellow), Pt-foil (blue), best performing sample (sample 4, green) and Raney NiMo (NiMo, purple).

Ni electroplating for HER catalysis has been exhaustively studied in the past. A comparison to several recent reports on such electrodes (Table 3) highlights the BO loops efficiency: a total of only 35 samples was sufficient to rival the best reported catalysts in this category, without prior knowledge of what a “good” set of parameters is for this specific synthesis route.

Electrode Type	Substrate	KOH Conc. [M]	η_{10} [mV]	Ref.
Ni Nano Particles	Ti	1	-197	[10]
Ni Nanocones	Cu	1	-215*	[5]
Ni Nanowire Array	Ti	1	-128	[11]
3D Ni Foams	Stainless Steel	8	-175*	[12]
Porous Ni	Ni	1	-243	[13]
Nanostructured Ni	Laser-treated Ni	1	-108	[14]
Sample 4	Perforated Ni	1	-129	This work

Table 3: Short overview of different state of the art Ni electrodes. All electrodes have been synthesised using an electrodeposition method. The electrodes listed in the table have been tested in KOH at room temperature. Values marked with * have been determined manually from LSV curves.

3.3 Four-Dimensional Parameter Space Optimization

Discovering the best sample after the first iteration in Section 3.2 can seem like a coincidence. To further explore the feasibility of the BO loop, a study using the method described in Section 2 was conducted with a modified setup and four parameters: in addition to i , t and T , the EDA concentration was varied in a range from 50 to 300 g L⁻¹. A sample with lower η_{10} than sample 4 (-117 mV @ 10 mA

cm^{-2}) was found after 1 iteration and 30 additional samples (see Table S2), proving that ML can steer the scientists into the right direction fast and efficiently, whereafter only fine tuning of the synthesis parameters is needed. The prediction model, even though progressing differently, ultimately finds t to remain a non-sensitive parameter (no substantial dependency between η_{10} and t , Figure 7). It also indicates that further improvement is possible e.g. by reducing the EDA concentration to approximately $220\text{--}230\text{ g L}^{-1}$ (Figure 7).

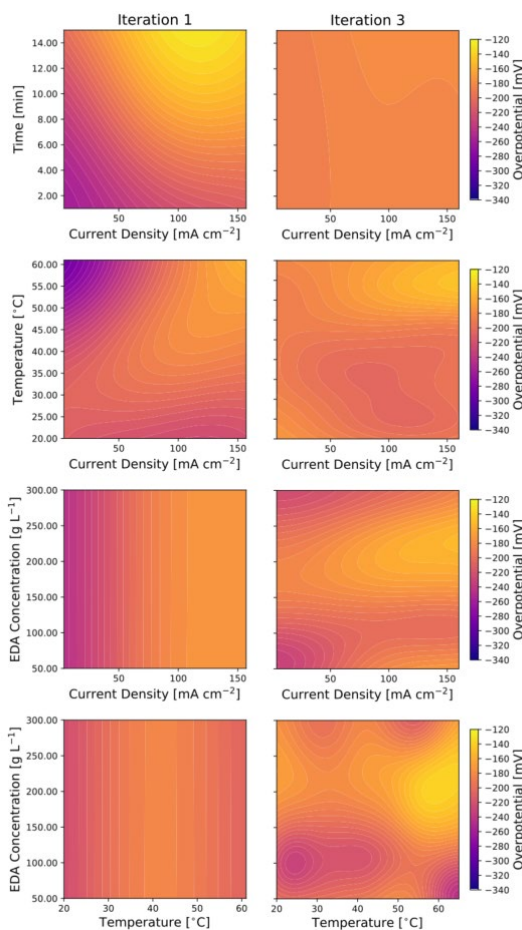


Figure 7: Illustration of $f_{\text{acquisition}}$ used to identify promising synthesis parameters. The model is based on known data points from Table S2 and shows the predicted η_{10} as function of four parameters, T , i , t and EDA concentration. Brighter colors indicate a low η_{10} and thus a good electrode performance.

4 Discussion

Over the course of this study, the application of ML for electrode development proved to be very effective: a substantial improvement of 204 mV over the performance of the Ni support was achieved iteratively in two separate instances, despite changes in the experimental setup.

In contrast to the linear grid study (section 3.1), the sensitivity analysis of the ML optimization finds T to be the most influential parameter for the synthesis. This discrepancy could be explained by the fact that for the linear grid study, only one parameter was varied while the others were kept constant. Therefore, only the T dependency along a straight line in the three-dimensional phase space is taken into account. This could lead one to investigate under false assumptions, whereas the sensitivity analysis utilizes all measured results.

When reducing the synthesis time of the best performing samples from 30 min down to 5 min (Figure S4), there is no significant reduction in performance nor any notable visual change of the sample surface. This indicates that the t mainly affects the layer thickness, while the microstructure stays the same. Also, it indicates that the porosity is homogeneous throughout the layer thickness and invariant to the synthesis time. Only the outermost part of the thicker layer is electrochemically active due to mass transport limitations. This effectively limits the maximum ECSA that can be achieved by this method and implies that even shorter deposition should be applicable while maintaining HER performance. This issue could potentially be bypassed by implementing a multi-step synthesis to achieve a pore size gradient throughout the layer to improve gas diffusion and allow deeper penetration of the layer.

Since there are no dopants added and XPS analysis revealed no residue from the precursors of the synthesis solution or contamination of iron from the temperature probe (see Figure S6) that could affect HER catalysis, it is reasonable to assume that the main factor for HER performance is the ECSA.

This is confirmed by double-layer capacitance measurements (see Figure S5) which show a logarithmic relationship between overpotential and surface roughness, as predicted by the Butler-Volmer equation.

While higher T and i typically yield more porous structures, it is not intuitive how these synthesis variables, as well as the EDA crystal modifier, impact the Ni nucleation and growth mechanism. Other studies such as [33]–[36] have tried to investigate how and why synthesis parameters such as i , T , pH and bath composition affect the deposits morphology and properties, yet findings sometimes conflict. For instance, Ebrahimi et al. [34] state that a high i should promote grain refinement due to a resulting higher overpotential promoting nucleation. Besides, he found that Cziraki et al. [37] experienced the opposite in their studies. Therefore, it can be difficult to predict which combination of synthesis parameters yields low η_{10} , high porosity and ECSA. Implementing a AI based optimization process enabled us to find a performance maximum in considerably less iterations and with higher confidence as compared to a linear grid search. With the used grid spacing (1 mA cm⁻², 1 min, 1 °C, 50 g L⁻¹) a full linear grid search in the defined range would comprise over 2 million parameter sets. It is clear that a in real manual study the researcher would rule out many combinations for impracticality or from scientific intuition and the actual number of experiments would be much smaller – however it is also evident that such a linear grid search would still be impossible. This work shows that computational guidance can enable us to explore far more complex search spaces than traditionally feasible, by pointing to their most promising regions and thus avoiding unnecessary experimental effort. This effect will be exacerbated as the number of parameters is increased, e.g. in the case of multi-metal coatings.

5 Conclusion

In this work it has been shown that an EDA modulated Ni electrodeposition method can be used to synthesize nano porous, high-performance HER electrodes. The method allows for precise control over the layer thickness and morphology, ranging from micrometer-sized, star-shaped features to

sandpaper-like structures with specific surface areas and overpotentials (-129 and -117 mV @ 10 mA cm⁻²) approaching the best known technical high surface area electrodes such as Raney Ni. Implementation of a ML assisted optimization process enabled us to find a performance-maximum twice in considerably less experimental iterations than what would have been necessary with a linear grid search, due to the unintuitive interdependencies of the synthesis variables.

6 Funding

The financial support from the Independent Research Fund of Denmark through the “Hydrogen in demand – (H2Now)” project (grant number 9041-00334B) and the DTU Alliance project “SeaCat” are gratefully acknowledged.

7 Data Availability

The raw data required to reproduce these findings are available to download from <https://sciedata.dk/shared/dtu.dk/1bd88f16a9c8efb0d4d3a583bc75cc26>. The processed data required to reproduce these findings cannot be shared at this time due to time limitations.

8 References

- [1] T. Skoczkowski, E. Verdolini, S. Bielecki, M. Kochański, K. Korczak, and A. Węglarz, “Technology innovation system analysis of decarbonisation options in the EU steel industry,” *Energy*, vol. 212, 2020, doi: 10.1016/j.energy.2020.118688.
- [2] A. Nurdawati and F. Urban, “Towards deep decarbonisation of energy-intensive industries: A review of current status, technologies and policies,” *Energies (Basel)*, vol. 14, no. 9, 2021, doi: 10.3390/en14092408.
- [3] International Energy Agency (IEA), “Global Hydrogen Review 2021,” 2021. doi: 10.1787/a15b8442-en.
- [4] Y. Guo, G. Li, J. Zhou, and Y. Liu, “Comparison between hydrogen production by alkaline water electrolysis and hydrogen production by PEM electrolysis,” *IOP Conf Ser Earth Environ Sci*, vol. 371, no. 4, p. 042022, Dec. 2019, doi: 10.1088/1755-1315/371/4/042022.
- [5] Gh. Barati Darband, M. Aliofkhaeaei, and A. Sabour Rouhaghdam, “Nickel nanocones as efficient and stable catalyst for electrochemical hydrogen evolution reaction,” *Int J Hydrogen Energy*, vol. 42, no. 21, pp. 14560–14565, May 2017, doi: 10.1016/j.ijhydene.2017.04.120.

- [6] P. Frink, "Hydrogen Energy Storage Study." IDC Clean Energy Project Preparation Advisory Services, 2018.
- [7] C. González-Buch, I. Herraiz-Cardona, E. Ortega, J. García-Antón, and V. Pérez-Herranz, "Synthesis and characterization of macroporous Ni, Co and Ni–Co electrocatalytic deposits for hydrogen evolution reaction in alkaline media," *Int J Hydrogen Energy*, vol. 38, no. 25, pp. 10157–10169, Aug. 2013, doi: 10.1016/j.ijhydene.2013.06.016.
- [8] A. Kam Cheong, A. Lasia, and J. Lessard, "Study of the Mechanism of the Hydrogen Evolution Reaction at Raney Nickel Electrodes in the Presence of Organic Compounds," *J Electrochem Soc*, vol. 141, no. 4, pp. 975–982, Apr. 1994, doi: 10.1149/1.2054867.
- [9] E. Hatami, A. Toghraei, and G. Barati Darband, "Electrodeposition of Ni–Fe micro/nano urchin-like structure as an efficient electrocatalyst for overall water splitting," *Int J Hydrogen Energy*, vol. 46, no. 14, pp. 9394–9405, Feb. 2021, doi: 10.1016/j.ijhydene.2020.12.110.
- [10] S. Tao, F. Yang, J. Schuch, W. Jaegermann, and B. Kaiser, "Electrodeposition of Nickel Nanoparticles for the Alkaline Hydrogen Evolution Reaction: Correlating Electrocatalytic Behavior and Chemical Composition," *ChemSusChem*, vol. 11, no. 5, pp. 948–958, Mar. 2018, doi: 10.1002/cssc.201702138.
- [11] X. Feng *et al.*, "Nickel Nanowire Arrays with Preferential Orientation for Boosting Hydrogen Evolution Reaction Capability," *J Electrochem Soc*, vol. 167, no. 10, p. 106501, Jun. 2020, doi: 10.1149/1945-7111/ab9756.
- [12] K. I. Siwek, S. Eugénio, D. M. F. Santos, M. T. Silva, and M. F. Montemor, "3D nickel foams with controlled morphologies for hydrogen evolution reaction in highly alkaline media," *Int J Hydrogen Energy*, vol. 44, no. 3, pp. 1701–1709, Jan. 2019, doi: 10.1016/j.ijhydene.2018.11.070.
- [13] C. Xu *et al.*, "Porous nickel electrodes with controlled texture for the hydrogen evolution reaction and sodium borohydride electrooxidation," *CrystEngComm*, vol. 22, no. 25, pp. 4228–4237, 2020, doi: 10.1039/D0CE00344A.
- [14] I. A. Poimenidis *et al.*, "Electrodeposited laser – nanostructured electrodes for increased hydrogen production," *Int J Hydrogen Energy*, vol. 47, no. 16, pp. 9527–9536, Feb. 2022, doi: 10.1016/j.ijhydene.2022.01.062.
- [15] T. W. David, H. Anizelli, T. J. Jacobsson, C. Gray, W. Teahan, and J. Kettle, "Enhancing the stability of organic photovoltaics through machine learning," *Nano Energy*, vol. 78, p. 105342, Dec. 2020, doi: 10.1016/j.nanoen.2020.105342.
- [16] C. Chen, Y. Zuo, W. Ye, X. Li, Z. Deng, and S. P. Ong, "A Critical Review of Machine Learning of Energy Materials," *Adv Energy Mater*, vol. 10, no. 8, p. 1903242, Feb. 2020, doi: 10.1002/aenm.201903242.
- [17] A. Bhowmik *et al.*, "Implications of the BATTERY 2030+ AI-Assisted Toolkit on Future Low-TRL Battery Discoveries and Chemistries," *Adv Energy Mater*, vol. 12, no. 17, p. 2102698, May 2022, doi: 10.1002/aenm.202102698.
- [18] Z. Wang, H. Zhang, and J. Li, "Accelerated discovery of stable spinels in energy systems via machine learning," *Nano Energy*, vol. 81, p. 105665, Mar. 2021, doi: 10.1016/j.nanoen.2020.105665.

- [19] Monika Vogler *et al.*, "Brokering between tenants for an international materials acceleration platform," *ChemRxiv*, 2022.
- [20] Z. Yao *et al.*, "Machine learning for a sustainable energy future," *Nat Rev Mater*, vol. 8, no. 3, pp. 202–215, Oct. 2022, doi: 10.1038/s41578-022-00490-5.
- [21] C. J. Taylor *et al.*, "A Brief Introduction to Chemical Reaction Optimization," *Chem Rev*, vol. 123, no. 6, pp. 3089–3126, Mar. 2023, doi: 10.1021/acs.chemrev.2c00798.
- [22] B. J. Shields *et al.*, "Bayesian reaction optimization as a tool for chemical synthesis," *Nature*, vol. 590, no. 7844, pp. 89–96, Feb. 2021, doi: 10.1038/s41586-021-03213-y.
- [23] N. H. Angello *et al.*, "Closed-loop optimization of general reaction conditions for heteroaryl Suzuki-Miyaura coupling," *Science (1979)*, vol. 378, no. 6618, pp. 399–405, Oct. 2022, doi: 10.1126/science.adc8743.
- [24] Z. Liu *et al.*, "Machine learning with knowledge constraints for process optimization of open-air perovskite solar cell manufacturing," *Joule*, vol. 6, no. 4, pp. 834–849, Apr. 2022, doi: 10.1016/j.joule.2022.03.003.
- [25] D. Bash *et al.*, "Multi-Fidelity High-Throughput Optimization of Electrical Conductivity in P3HT-CNT Composites," *Adv Funct Mater*, vol. 31, no. 36, p. 2102606, Sep. 2021, doi: 10.1002/adfm.202102606.
- [26] Y. Zhao *et al.*, "Machine Learning Assisted Design of Experiments for Solid State Electrolyte Lithium Aluminum Titanium Phosphate," *Front Mater*, vol. 9, Feb. 2022, doi: 10.3389/fmats.2022.821817.
- [27] C. H. Liow *et al.*, "Machine learning assisted synthesis of lithium-ion batteries cathode materials," *Nano Energy*, vol. 98, p. 107214, Jul. 2022, doi: 10.1016/j.nanoen.2022.107214.
- [28] W. Zhou, Z. Zheng, C. Wang, Z. Wang, and R. An, "One-Step Fabrication of 3D Nanohierarchical Nickel Nanomace Array to Sinter with Silver NPs and the Interfacial Analysis," *ACS Appl Mater Interfaces*, vol. 9, no. 5, pp. 4798–4807, Feb. 2017, doi: 10.1021/acsami.6b13031.
- [29] P. Connor, J. Schuch, B. Kaiser, and W. Jaegermann, "The Determination of Electrochemical Active Surface Area and Specific Capacity Revisited for the System MnOx as an Oxygen Evolution Catalyst," *Zeitschrift für Physikalische Chemie*, vol. 234, no. 5, pp. 979–994, May 2020, doi: 10.1515/zpch-2019-1514.
- [30] C. E. Rasmussen and K. I. Williams, *Gaussian processes for machine learning*, ISBN 026218253X. MIT Press, 2006.
- [31] Niranjan Srinivas, Andreas Krause, Sham M. Kakade, and Matthias Seeger, "Gaussian Process Optimization in the Bandit Setting: No Regret and Experimental Design," *Proceedings of the 27th International Conference on Machine Learning*, pp. 1015–1022, 2010.
- [32] W. A. Appiah, J. Busk, T. Vegge, and A. Bhowmik, "Sensitivity analysis methodology for battery degradation models," *Electrochim Acta*, vol. 439, p. 141430, Jan. 2023, doi: 10.1016/j.electacta.2022.141430.

- [33] A. Boukhouiete, S. Boumendjel, and N. E. H. Sobhi, "Effect of current density on the microstructure and morphology of the electrodeposited nickel coatings," *Turk J Chem*, vol. 45, no. 5, pp. 1599–1608, 2021, doi: 10.3906/kim-2102-46.
- [34] F. Ebrahimi and Z. Ahmed, "The effect of current density on properties of electrodeposited nanocrystalline nickel," *J Appl Electrochem*, vol. 33, no. 8, pp. 733–739, 2003, doi: 10.1023/A:1025049802635.
- [35] J. M. Lee, K. K. Jung, and J. S. Ko, "Effect of NaCl in a nickel electrodeposition on the formation of nickel nanostructure," *J Mater Sci*, vol. 51, no. 6, pp. 3036–3044, Mar. 2016, doi: 10.1007/s10853-015-9614-8.
- [36] X. Yu, J. Yang, X. Ren, and Z. Sui, "Influences of pH and EDTA Additive on the Structure of Ni Films Electrodeposited by Using Bubble Templates as Electrocatalysts for Hydrogen Evolution Reaction," *Membranes (Basel)*, vol. 11, no. 3, p. 165, Feb. 2021, doi: 10.3390/membranes11030165.
- [37] Á. Cziráki, B. Fogarassy, I. Geröcs, E. Tóth-Kádár, and I. Bakonyi, "Microstructure and growth of electrodeposited nanocrystalline nickel foils," *J Mater Sci*, vol. 29, no. 18, pp. 4771–4777, Sep. 1994, doi: 10.1007/BF00356522.

Supplementary Information: ML Guided Development of High-Performance Nano-Structured Ni Electrodes for Alkaline Water Electrolysis

Veronica Humlebæk Jensen^a, Enzo Raffaele Moretti^a, Jonas Busk^a, Emil Howaldt Christiansen^a, Sofie Marie Skov^a, Emilie Jacobsen^a, Mikkel Rykær Kraglund^a, Arghya Bhowmik^a, Ragnar Kiebach^{a,*}

a. Department of Energy Conversion and Storage, Technical University of Denmark, Lyngby Campus, Anker Engelunds Vej, 2800, Denmark

Solution Stability and Sample Reproducibility

For practical purposes, the deposition bath was reused multiple times in this study. To ensure reproducibility, a control sample was synthesized regularly using the parameters; 5 min, 25 mA cm⁻² and 65 °C and tested using the procedure described in section 2.1.2. As shown in Figure S1, the control samples performance is stable and within the expected measurement uncertainties up until sample 31, where a 20 mV increase in performance can be observed at 10mA cm⁻². This investigation thus indicates that the solution was stable for the first 25 samples.

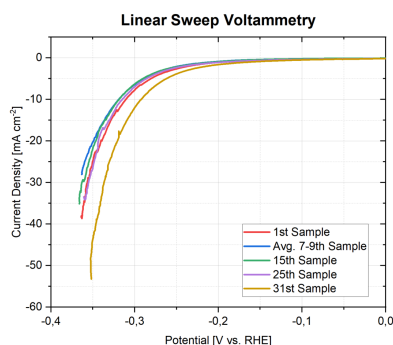


Figure S1: Recorded control sample LSV curves.

Overview of All Synthesized Samples

	t [min]	i [mA/cm ²]	T [°C]	η_{10} [mV]	R_f
Time Var.	2	75	65	-242	1083
	5			-232	1271
	10			-260	941
	15			-264	116
	20			-286	545
	25			-283	579
Current Density Var.	5	25	65	-319	551
		50		-326	625
		75		-280	1851
		100		-226	2883
		125		-214	4386
		150		-216	3063
Temperature Var.	5	75	20	-256	2769
			25	-268	2648
			35	-264	3209
			45	-256	3910
			51	-253	4643
			60	-249	5556
Constant Charge	2	160	65	-196	-
	4	80		-246	-
	8	40		-300	-
	16	20		-269	-
	32	10		-316	-
	64	5		-313	-
Random Parameter Study	26	139	21	-226	3198
	41	7	24	-173	9213
	32	40	31	-197	4651
	13	151	32	-209	4445
	22	39	39	-179	5056
	45	24	47	-227	2760
	20	112	52	-166	7225
	30	36	57	-269	1564
Iter. 1	See article				
Iter. 2	See article				
Iter. 3	See article				

Table S1: Summary of all samples synthesised. In the table the synthesis parameters have been included together with the individual sample's η_{10} and R_f .

*Note in the linear grid study the same sample was synthesized twice (5 min, 75 mA cm⁻², 65 °C). An average of these two samples have been used in Figure 2 and for the BO.

Coverage of Parameter Space

In the parameter study a linear grid search was conducted to investigate the influence of the individual parameters. In total 24 samples were made, and as seen in Figure S2 their synthesis parameters do not cover the entire parameter space, while many of the synthesis parameters have been repeated or used frequently (minimum 6 times).

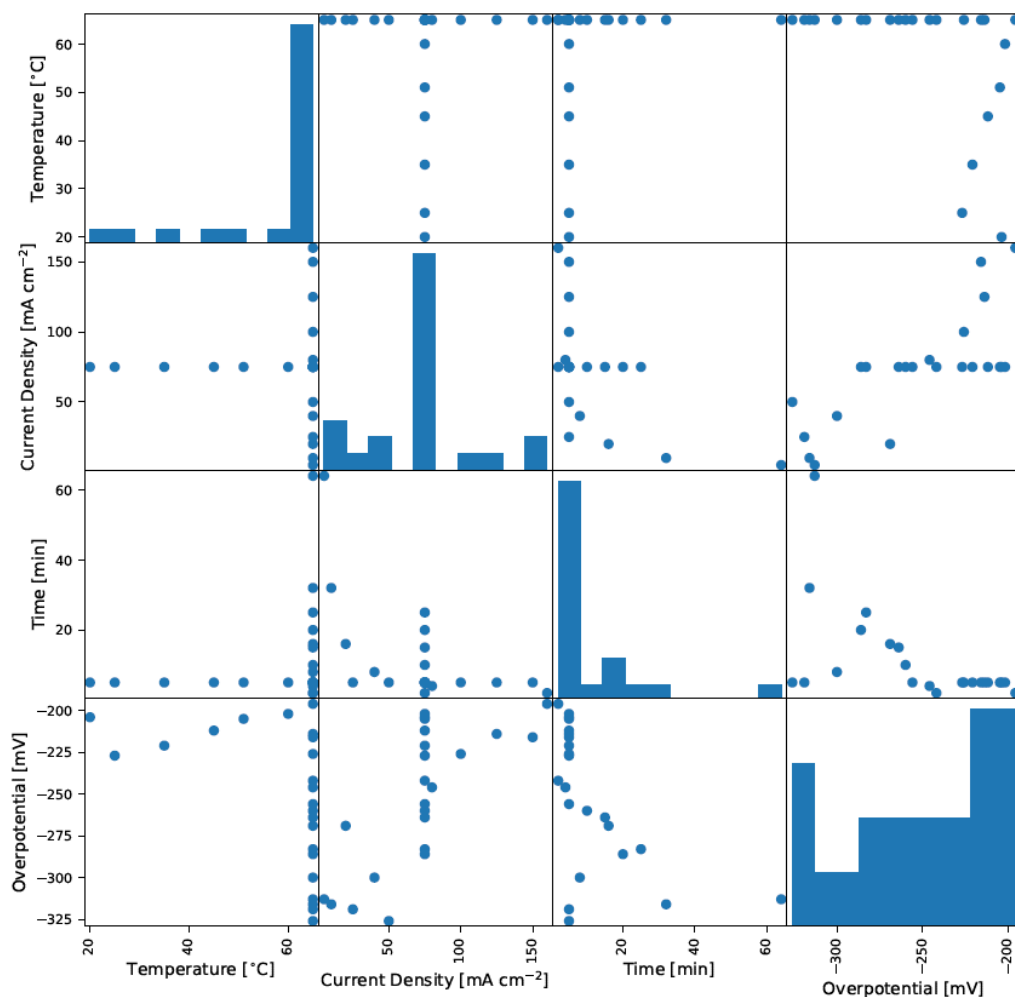


Figure S2: Parameter distribution. The parameter space consists of many repeated values and do not cover the entire parameter space.

Sensitivity Analysis and Deposition Time

In the sensitivity analysis, the GP regression model is used to evaluate how sensitive the electrode performance is towards synthesis parameter changes. To conduct this analysis all but one parameter is kept constant to investigate how the mean prediction of the overpotential changes as function of either T , i or t . As shown in Figure S.3 t as the only parameter does not affect the electrode performance/ η_{10} .

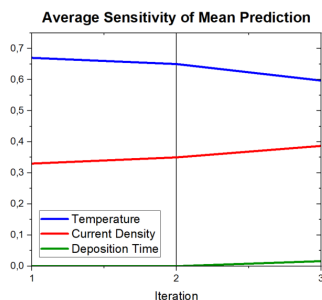


Figure S3: Summary of the sensitivity analysis. The values in the plot have been normalized. Unlike the parameter study T has been identified as the most sensitive synthesis parameter, while t is an insignificant parameter.

Considering that no visual change was observed in Figure 2 and that only minor changes to η_{10} was found in Figure 3 when varying t , the best sample (sample 4, 30 min, 147 mA cm^{-2} and 51 $^{\circ}\text{C}$) was synthesized using a shorter deposition time. As seen in Figure S4, the sample performance at 10 mA cm^{-2} is largely independent of t .

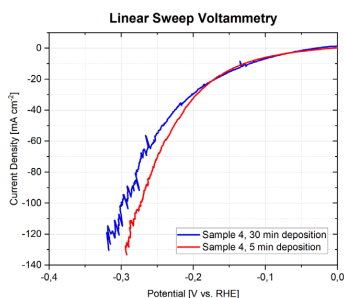


Figure S4: Two samples synthesised using the same i and T during deposition but different t . The performance of the two samples at 10 mA cm^{-2} is practically the same.

Roughness Factor vs. Overpotential

As seen in Table 2 generally a high R_f can be related to a low η_{10} . This is in line with the Butler-Volmer equation, which requires a logarithmic relationship between surface roughness and overpotential. To investigate if such a relationship exists the R_f and the measured η_{10} from Table 3 and Table S1 have been plotted in a semi-logarithmic plot in Figure S5.

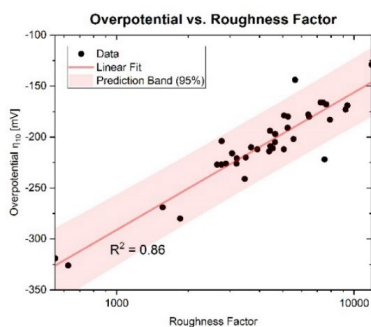


Figure S5: The R_f vs. η_{10} at 10 mA cm^{-2} in a semi-logarithmic plot. The data have been fitted and a prediction band added. The Figure illustrates that a linear relationship between the R_f and η_{10} must exist.

As seen in Figure S1, η_{10} decreases logarithmically with R_f . A confidence bound has been added to the fit.

Four-Dimensional Parameter Space Optimisation

No.	T [°C]	i [mA/cm ²]	t [min]	EDA Concentration [g/L]	η_{10} [mV]
1st iteration					
1	51	147	5	200	-176
2	20	35	7	200	-248
3	45	27	10	200	-217
4	50	157	15	200	-182
5	61	142	13	200	-149
6	51	147	5	50	-174
7	33	94	14	50	-148
8	41	30	5	50	-252
9	55	4	10	50	-322
10	56	12	5	50	-302
11	51	147	5	100	-226
12	24	108	6	100	-271
13	37	61	2	100	-255
14	41	52	4	100	-236
15	48	144	2	100	-249
16	51	147	5	300	-240
17	31	28	3	300	-263
18	56	109	1	300	-252
19	58	4	2	300	-335
20	60	78	14	300	-220
2nd iteration					
21	65	160	15	50	-221
22	65	120	15	50	-282
23	65	160	5	50	-266
24	45	160	15	50	-214
25	45	160	5	50	-260
26	65	160	15	300	-117
27	65	120	15	300	-189
3rd iteration					
28	50	120	5	50	-198
29	60	160	5	200	-149

Table S2: Summary of all samples synthesised in the additional study (section 3.3) with four parameters. In the table the synthesis parameters have been included together with the individual sample's η_{10} and R_f .

X-Ray Photoelectron Spectroscopy

XPS was conducted on 8 samples to examine if other species from the precursors in the solution (Cl, H, O, B, N, C) were deposited apart from Ni.

As seen on the example in Figure S6, no apparent peaks from the above-mentioned elements have been found with the exception of carbon, which can be attributed to adsorbed species from ambient air during sample handling.

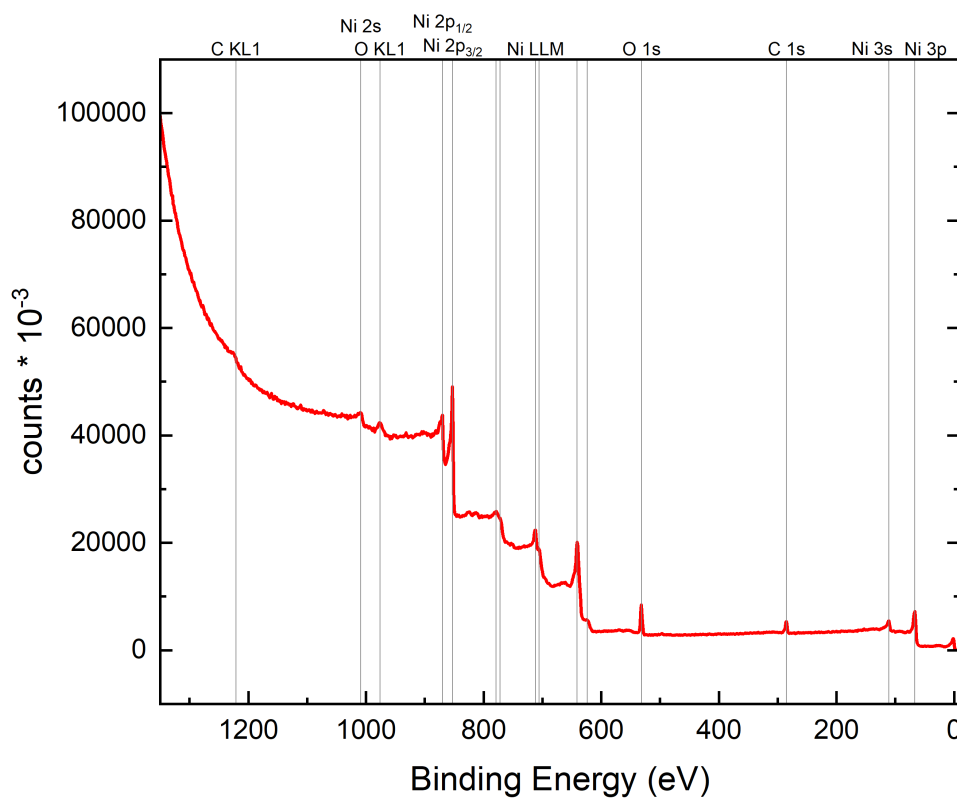


Figure S6: Example of an XPS survey scan from an electrodeposited sample ($T = 57\text{ }^{\circ}\text{C}$, $t = 30\text{ min}$, $i = 36\text{ mA/cm}^2$). There is no evidence for any impurity phases from the deposition process in the samples.

Conclusion

In this thesis, noble metal free catalysts for alkaline water electrolysis have been investigated. The main focus was put on the reduction of the reaction overpotential by optimizing the material composition and micro structure.

In the first project presented in this work, a screening study of Ni based transition metal hydroxide compounds as catalysts for the OER in alkaline conditions was conducted. A co-precipitation synthesis method was used to coat the active layer directly onto a Ni foam substrate. In total 36 compositions with either one or two dopants comprised from 8 different metals (Fe, Cr, Al, Co, Ni, Mn, Zn, Cu) were investigated. Electrochemical test were carried out in 1 M KOH and in 1 M KOH + 0.5 M NaCl. The latter served as a first indication on the feasibility of these catalysts for direct seawater electrolysis.

Fe containing compounds performed by far the best in terms of OER overpotential. Cr, Co and Al doping resulted in further improvement of the NiFe-LDH, achieving 247 mV overpotential at 10 mA cm^{-2} in the case of NiFeCr-LDH. Cu on the other hand had a detrimental effect on the OER performance. Although some Fe-free samples show good OER activity, the best of them (Al, Co) still trail behind the Fe compounds by about 60 mV. For the Fe containing samples, XRD measurements confirmed that the deposition layer is present in LDH crystal structure. In the case of FeCu, EDX and XPS showed that significant amounts of CuO were formed, and further indicated that the presence of Cu hindered LDH formation. FTIR and XPS showed that the LDH materials were carbonate intercalated. While most compositions perform very similarly in both electrolytes, some samples, e.g. Mn, show noteworthy differences in the overpotential. The exact causes of this behaviour could be the starting point for further studies.

The fast synthesis procedure and good reproducibility, paired with OER activity comparable with some of the best reported OER electrodes to date, rendered this method feasible for a larger screening study considering multi metal compositions. To accel-

erate the search for high performance catalysts in complex phase spaces, the second project is therefore concerned with the design of an autonomous robotic platform for the synthesis, electrochemical investigation and machine-learning based optimization of multi-metal hydroxides for the alkaline OER, based on the same co-precipitation approach. The first results that were obtained with this novel setup show very good data quality in terms of reproducibility and signal to noise ratio. Since the system is designed to carry out standard electrochemical investigations, this allows not only for basic analysis concerning only a specific figure of merit, for example the overpotential at a given current density, but to acquire full data sets for every composition, including impedance spectroscopy, electrochemically active surface area and full CVs. Trends that were seen in the grid study performed previously by hand were also reproduced by the autonomous system. Although some technical issues regarding contamination must still be overcome, the first results are promising and all requirements necessary for a successful optimization in a multi parameter phase space appear to be fulfilled.

Lastly, it has been shown that an EDA modulated Ni electrodeposition method can be used to synthesize nano porous, high-performance HER electrodes. The method allows for precise control over the layer thickness and morphology, ranging from micrometer-sized, star-shaped features to sandpaper-like structures with specific surface areas and overpotentials (-129 and -117 mV @ 10 mA cm⁻²) approaching the best known technical high surface area electrodes such as Raney Ni. Implementation of a ML assisted optimization process enabled us to find a performance-maximum twice in considerably less experimental iterations than what would have been necessary with a linear grid search, due to the unintuitive interdependencies of the synthesis variables. What makes this work particularly interesting is that it can be applied to a wide variety of problems in material design, and no special equipment is necessary. Future work could extend this study to co-deposition of NiCo or NiMo bimetallics, which are known to exhibit exceptional HER activity.

Appendices

APPENDIX **A**

Journal articles

Cite this: DOI: 00.0000/xxxxxxxxxx

Lab scale 3-electrode holder for zero/controlled-gap electrode configuration fabricated using 3D printing[†]

Fabian Luca Buchauer,^{*a} Andrea Russo,^a Enzo Raffaele Moretti,^a Sarmad Iqbal,^a Mikkel Rykær Kraglund,^a and Christodoulos Chatzichristodoulou^aReceived Date
Accepted Date

DOI: 00.0000/xxxxxxxxxx

Electrochemistry is key for green fuel and chemical production. In order to achieve low production costs required for large-scale deployment of e.g. electrolyzers, more active and stable catalyst materials for both anode and cathode are necessary. While extensive research efforts are devoted to this, most lab scale catalyst testing is performed in either rotating disk electrodes or beaker-type cells that hardly reflect the operating conditions in a technological electrolyzer. While there are more realistic test setups available commercially, they are usually expensive and complex. In this work, we provide a 3D-printable cell holder design that allows for lab-scale testing under zero-gap or controlled-gap electrode configuration, while supporting the placement of a reference electrode at the middle of the separator. The customizable design can accommodate electrodes of various sizes and geometries (foam, mesh, foil, etc.). Polypropylene (PP) or high-performance thermoplastics like polyetheretherketone (PEEK) can be used as filaments, depending on the application. 3D-printing of the herein presented cell results in material savings of 70%, thereby reducing material waste and environmental impact. We demonstrate the holder in both zero-gap and non-zero gap configurations, assessing data quality and reproducibility, using Fe-free Ni electrodes in alkaline electrolysis as test case. The design is freely available for download as a CAD file.

Introduction

Electrocatalysis, and electrolytic green hydrogen production in particular, are critical in enabling the decarbonization of heavy transport and the chemical industry, while facilitating storage and recovery of intermittent electricity. Several electrolysis technologies are currently being developed, each with its advantages and disadvantages. These include solid oxide electrolysis (SOEL), proton exchange membrane electrolysis (PEMEL), anion exchange membrane electrolysis (AEMEL), and alkaline electrolysis (AEL). While each technology has its strengths and weaknesses, AEL is considered the most mature and well-established option.

Commercial alkaline electrolysis stack designs fundamentally differ from lab-scale electrolysis cells and testing. In commercial electrolysis stacks, electrodes and membranes are stacked on top of each other without significant space in between in a so-called zero-gap configuration, resulting in the blocking of the electrode surface of both anode and cathode by the separator¹. Blockade of the electrode surface significantly impacts the gas transport away from the catalytically active surface and, therefore, substantially

impacts the measured activities of the investigated electrodes².

As Kraglund et al. show, zero gap test setups have been developed³. However, such setups are typically complex to establish in-house and expensive due to their high acquisition cost. Furthermore, most commercial setups provide limited customizability for specific needs. Therefore, most lab-scale testing of catalysts and 3-dimensional electrodes is done in either rotating disk electrode setups or beaker cells. These setups are model cases that do not represent the actual use case, as mass transport phenomena occurring in zero-gap are not considered.

Alternative materials should be used for the experimental setup to avoid potential issues, such as chemical leaching and breakage, associated with using glassware in a strongly alkaline environment. Recent advancements in 3D printing have led to impressive breakthroughs. State-of-the-art printers now offer exceptional accuracy, reaching a few micrometers while enabling the use of complex, chemically resistant thermoplastics. Notably, materials like Polypropylene (PP), Polysulfone (PS), and the more recent Polyetheretherketone (PEEK) are commercially available for 3D printing⁴. These developments have created exciting opportunities for producing components designed to withstand the harsh environment in alkaline electrolysis cells (concentrated KOH with pH14-15), opening up new possibilities for scientific research and experimentation. 3D printing facilitates rapid and cheap proto-

^a Department of Energy Conversion and Storage, Technical University of Denmark, Fysikvej Building 310, 2800 Kgs. Lyngby, Denmark. E-mail: falubu@dtu.dk

[†] Electronic Supplementary Information (ESI) available: [details of any supplementary information available should be included here]. See DOI: 10.1039/cXsm00000x/

typing, allowing the iteration of cell designs and customization of cells for specific use cases. Additionally, complex, unfeasible cell geometries for other production methods become possible. This makes 3D printing a viable option in designing electrolysis cells for lab-scale testing without purchasing an expensive third-party setup or machining a custom cell.

This paper introduces a novel, customizable 3D printable alkaline electrolysis cell design. The cell can be printed using Polypropylene (PP) using commonly available printers or, if a suitable printer is available, printed with Polyetheretherketone (PEEK). Other materials with appropriate chemical resistance may also be feasible but have yet to be evaluated. The study focuses on assessing the reproducibility and stability of the 3D printed cell and its accompanying components, explicitly investigating the performance of Nickel-mesh as an Oxygen-Evolution-Reaction (OER) catalyst. The experiments are conducted in Fe-free 1M KOH solution, utilizing a zero gap configuration and a 3mm gap between the separator and electrode. The findings showcase the excellent suitability of 3D-printed cells as electrolysis cells, providing more realistic test conditions for future research. The SolidWorks files and drawings of the project are freely available to all interested individuals.

Experimental section

Materials

For the experiments KOH \geq 85% pellets (ACS reagent), HCl 37% w/w (reagent grade), and $\text{Ni}(\text{NO}_3)_2 \cdot 6\text{H}_2\text{O} \geq 94.5\%$ from Sigma Aldrich were used. The utilized Ni wires have $\geq 99.98\%$ purity and are from Alfa Aesar. For 3D printing, PEEK filament from CreatBot and PP filament from Ultimaker were utilized. PEEK screws and nuts (M3) were supplied by NBK America. Banana plugs (8mm diameter, gold-plated brass) were purchased from Hirschmann Test and Measurement. As a working electrode material, Ni-mesh 1250 with an open area of 9.4% from Hebei Aegis Metal Materials was used. The counter electrode was a Nickel perforated plate from Veco Precision, and Zirfon PERL UTP 500 (Agfa) served as the separator material.

Cell printing and design

The cell design is modular, offering easy customization. All drawings are created using Solidworks and are available for download free of charge. The initial prototype of the cell was printed in PP, which can be easily 3D printed using conventional printers from different brands (e.g. Ultimaker S3) since it only requires extrusion temperatures similar to conventional 3D printing materials such as Polylactic Acid (PLA). The results shown in this work were obtained with a cell printed in PEEK. For this, a CreatBot PEEK300 printer was utilized, as the high-temperature properties of PEEK necessitate elevated printing temperatures.

KOH Electrolyte purification

To prepare Fe-free electrolytes, we followed a preparation method similar to the one used in Trotochaud et al.'s study⁵. In short, HCl cleaned 200ml PP centrifuge bottles were filled with 8 g of $\text{Ni}(\text{NO}_3)_2 \cdot 6\text{H}_2\text{O}$, which was dissolved in 16 ml of 18.2MΩcm wa-

ter and 80ml of 1M KOH. This results in the precipitation of $\text{Ni}(\text{OH})_2$. The mixture was vigorously shaken for 5 min followed by 10 min of centrifuging at 8000rpm. The supernatant was decanted and discarded. Afterwards, the $\text{Ni}(\text{OH})_2$ was washed two times using a mixture of 80ml of 18.2MΩcm water and 8ml of 1M KOH. The solid was re-dispersed by vigorous shaking prior to each washing cycle and the supernatant was decanted and discarded at the end of each washing cycle. Finally, HCl cleaned 200ml PP centrifuge bottles (containing the $\text{Ni}(\text{OH})_2$) were filled with 200ml of 1M KOH pre-electrolyzed at 2.0V for 24h using Ni foam electrodes (Alantum). The solution was mechanically agitated for 5 min followed by vigorous shaking for 5 min. After a 3h resting period the solution was sonicated for 10 min at 8000rpm and the supernatant was decanted into a HCl cleaned PP bottle.

Cell preparation

The cell and all its components were washed for 1h in 1M HCl. Nickel mesh (16mm x 5mm) as working electrode and Nickel perforated plate (16mm x 25mm) as counter electrode were cut and sonicated for 10 min in 1M HCl. Afterwards, the assembly, electrodes, and separator were thoroughly washed three times with 18.2MΩcm water and dried using lint-free paper. The cell was assembled by placing the Ni-mesh, separator, and Ni-perforated plate on/in the respective holder section and tightening the PEEK screws and nuts hand tight. Subsequently, the cell was filled until 2/3 full with Fe-free electrolyte. A Mini-HydroFlex reversible hydrogen electrode (RHE) from Gaskatel was used as reference electrode.

Electrochemical characterization

The electrochemical measurements were conducted using a Biologic SP-240. The electrochemically active surface area (ECSA) was measured, after 10 min of continuous bubbling with N_2 , using potential cycling at various scan rates (10, 20, 50, 100, 200, 300 and 400mV/s) from 0.65V to 0.75V vs. RHE. The ohmic resistance was determined using potentiostatic impedance spectroscopy at 1.2V vs. RHE. Thereafter, the sample was conditioned using chronopotentiometry at 10mA/cm² for 10 min. This was followed by 250 cycles of cyclic voltammetry from 1V to 1.7V vs. RHE at 100 mV/s. Then linear sweep voltammetry at ?? mV/s was measured in the same range. Finally, chronopotentiometries were recorded at current densities of 50, 20, 10, 5 and 1mA/cm² for 5 min each, followed by galvanostatic impedance spectroscopy at the same current density. The presented data is iR-corrected to compensate for the solution resistance, the separator, and the wires. The reported working electrode area corresponds to the entire geometric area of the electrode, although this is partly covered by the contact wires.

Holder description

The holder is designed as a modular cell, offering the flexibility to explore different electrode geometries through the use of customizable accessory designs. This unique feature allows for the testing of 3-dimensional porous electrodes (e.g. Ni-foam, mesh, etc.), dense materials (e.g. metal plates, oxide pellets, etc.), or

soft porous materials that require structural support for stability (e.g. nanofibers, carbon cloth/paper, etc.), all within the same test setup. In this study, we demonstrate two accessories that enable testing of porous electrodes (Figure 1B/C), and dense plates (Figure 1D).

The different accessories and possible assemblies can be seen in Figure 1. The holder was first prototyped in PLA and then printed in PP and PEEK. PEEK is mechanically robust, chemically stable in both acidic and alkaline environment, and temperature-resilient allowing for use of the printed holder at temperatures above 100 °C⁶.

A schematic of the cell components can be seen in Figure 2. It includes the working electrode, a membrane/separator, and the counter electrode. The design of the holder segments accommodates Ni-wires for electrical interfacing, with separate connections for current carrying and voltage sensing leads. To minimize the contribution of the Ni-wires to the electrochemical performance, the Ni-wires are wrapped in PTFE tape, to block their surface, except where the wires press against the working electrode. In zero-gap configuration (Figure 1B), the membrane electrode assembly (MEA) is placed in a 2-piece accessory, which is secured by up to 6 M3 bolts and nuts. The distance between the electrodes/current collectors and separator/membrane/MEA is $d=0\text{mm}$; the distance between the working and counter electrode is therefore equal to the separator thickness (e.g. $500\mu\text{m}$ in the case of the Zirfon Perl 500 separator employed here). In case dense materials are the focus of the investigation, the non-zero gap configuration, Figure 1D, can be used. This configuration introduces a well-defined gap between the working electrode and the separator ($d=3\text{mm}$ in this example) allowing for gas evolution at the front surface of the electrode while blocking the back side.

The reservoir holder (Figure 1A) accommodates the slide-in accessories, ensuring their fixed placement, and incorporates separate compartments specifically designed for the placement of reference electrodes. The use or not of a reference electrode (RE) is what differentiates 3-electrode measurements from single-cell experiments. Especially in zero-gap configuration, implementing a RE is not straightforward. The current design allows for the placement of the RE next to the MEA, or in a separate compartment which interfaces to the edge of the separator (approximately 2.5cm away from the MEA).

3D printing presents a multitude of advantages over conventional machining, primarily due to its superior material utilization and adaptability. If the reservoir was instead machined out of solid blocks of PEEK (80mmx80mmx58mm) with a total volume of 371.2cm^3 , 70% of the material would have to be removed. To make matters worse, PEEK blocks are typically only available in certain geometries, further reducing actual material utilization. The option of printing the device with partial infill (in our case 15%) instead of solid walls allows further material savings. Furthermore, conventional machining is challenged by internal hole drilling, while 3D printing excels at creating complex structures in any orientation. Overall, 3D printing avoids material waste by adding material only where necessary, resulting in cost savings and an eco-friendly approach. The advent of 3D printing with

durable, chemically resistant materials (e.g. PP or PEEK) allows serving applications that involve aggressive environments, overcoming contamination from conventional glassware that beakers and RDE containers are often made of.

Figure 3 shows images of the 3D-printed holder and its different slide-in accessories. The Ni-wires, used for contacting the electrodes, are welded to banana plugs (Gold-coated) to ensure a secure and stable connection.

The reservoir can be easily adapted for different volumes. The slide-in accessory design allows for a rapid exchange of samples as well as customization for sample type and size, while ensuring fixed, reproducible and customizable placement. When using common materials like PP, no specialized equipment (i.e. a high-temperature 3D printer) is needed, which makes the design useful for a wide audience of researchers.

Results and discussion

In this paper, we present the results of a comprehensive effort to assess the reproducibility of measurements achieved through our novel 3D-printed holder. We examine the influence of RE placement as well as the use of zero-gap and non-zero gap configurations. All measurements are conducted using the same experimental protocol and are preceded by a meticulous cleaning procedure of the cell assembly to ensure the same status quo. Each accessory was evaluated by three independent users following the same procedure (see section "Cell preparation").

The OER activity of NiOOH in alkaline environment has been selected as a test case because of its sensitivity to Fe impurities, local KOH concentration, and conditioning procedure. The incorporation of small amounts of Fe into the $\text{Ni}(\text{OH})_2$ structure leads to a substantial enhancement in OER activity and makes the reproduction of results difficult as reported in Corrigan et al.⁷. Trotochaud et al. demonstrated that even traces of Fe impurities in electrolytes have a remarkable impact on the OER activity⁵. This enhancement is evident through a lowered onset potential and significantly improved conductivity following Fe incorporation.

Zero gap configuration

Initially, the Ni-mesh was subjected to a constant current of $10\text{mA}/\text{cm}^2$ for a duration of 10min, followed by 250 cycles of cyclic voltammetry (CV) for conditioning. The results of the CV cycling are illustrated in Figure 4A1). Notably, the oxidation and reduction features of the Ni-mesh exhibit a gradual increase. In a Fe-free electrolyte, the oxidation peak typically exhibits a main peak with a shoulder, similar to the LSV plot shown in Figure 4C. However, due to the fast scan rate of $100\text{mV}/\text{s}$, this characteristic peak structure could not be resolved. Additionally, there is a noticeable jump in the recorded current at the peak maximum, which is likely caused by a switch in the current range of the potentiostat.

The OER activity improves during the first few cycles, followed by a decline in subsequent cycles. This is highlighted in Figure 4A2, where the current density at 1.69 V vs RHE is reported. Notably, after several cycles, a new oxidation peak emerges at 1.56 V vs RHE. This has been previously observed by Corrigan et al. and

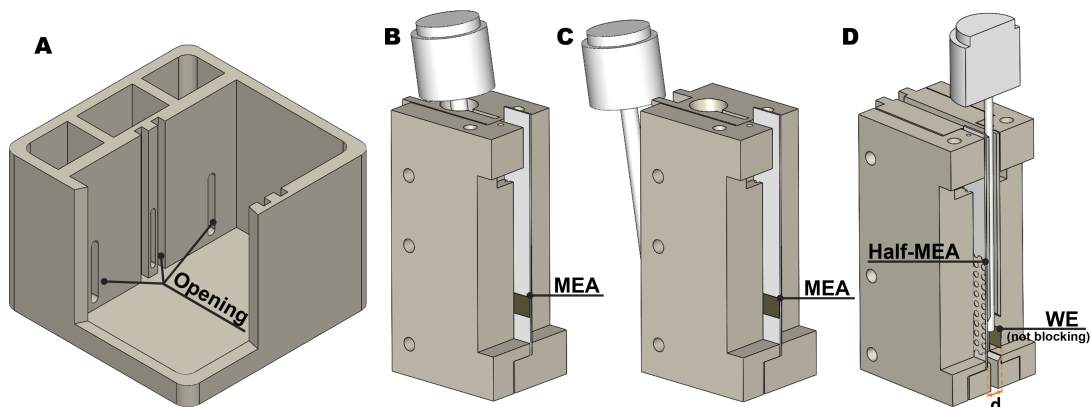


Fig. 1 A) Reservoir holder illustration showing how side compartments are electrolytically connected to the main compartments. B) Zero-gap accessory with reference electrode placement right next to the MEA. C) Zero-gap accessory with reference electrode placement in the side compartment. D) Fixed gap accessory with reference electrode placement in between the working and counter electrode.

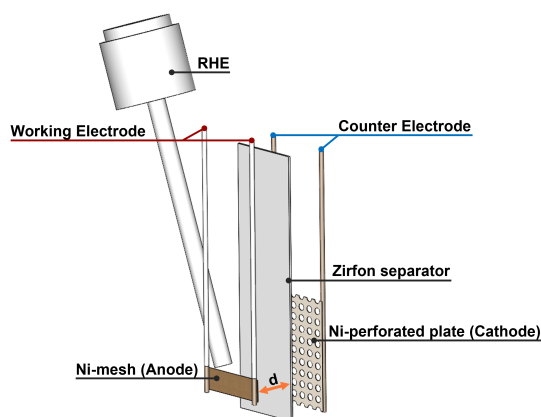


Fig. 2 Schematic of the test setup.

Trotochaud et al., who speculated that it may be caused by the presence of a small amount of Ni^{4+} at the edges of $\alpha\text{-Ni}(\text{OH})_2$ or $\gamma\text{-NiOOH}$ sheets⁷⁵. The appearance of this oxidation peak coincides with the downturn in OER activity. Furthermore, the intensity of the oxidation peak at 1.56 V vs. RHE increases with cycle number, along with the continuing decline of the OER activity. Interestingly, the decrease in activity is solely reflected in the onset-potential, as the Tafel slope remains constant across all cycles, again similar to Corrigan et al. and Trotochaud et al. As the number of cycles increases, the oxidation peak shifts towards higher potentials, while the reduction peak shifts towards lower potentials. This shift seems to be constant with an increasing number of cycles.

One of the desirable characteristics of a test setup is its ability to prevent deviations in measurements performed by different users, often associated with differences in mounting of the sam-

ple and/or the electrical connections. For this reason, the sample is rigidly fixed from both sides at a specific distance from the separator/membrane and the potentiostat is attached via stable banana plugs in our holder design. To assess the reproducibility of the setup in this regard, measurements were conducted by three different users (U1, U2, and U3) employing identical protocols, cells, and materials (see Figure 4). It is noteworthy that all measurements exhibited the previously described behavior consistently throughout the 250 CV cycles. Moreover, the LSV plots in Figure 4C demonstrate near identical results in terms of reduction features, with virtually no discernible difference in OER activity; the overpotential at $10\text{mA}/\text{cm}^2$ varies by only XY mV. Furthermore, the LSV measurements were identical for the two RE positions explored by all three users. For improved visibility, only a single anodic scan is shown as a representation for all users. This remarkable consistency further underscores the reproducibility achievable with the experimental setup.

To determine the double-layer capacitance of the electrochemically active surface, CV cycling at various scan rates was performed. Figure 4B displays the CVs obtained at different scan rates. The CVs exhibit an almost perfect capacitor-like behavior, characterized by nearly rectangular shapes similar to the Morales et al., where perfect capacitors were modeled and measured⁸.

The plot in Figure 4E illustrates the capacitive current density as a function of the scan rate as measured by all three users. Notably, all three measurements exhibit similar capacitance per area of around $0.2\text{mF}/\text{cm}^2$, a value that lies at the lower end of typical electrodes. In comparison, high surface area samples typically display capacitance values ranging from $20\text{mF}/\text{cm}^2$ to $70\text{mF}/\text{cm}^2$ ^{9,10}. Therefore, the spread obtained between users is considered satisfactory.

Figure 4D depicts the overpotential at various current densities obtained from chronopotentiometry. All measurements - including different users and different RE placements - show practically no difference in overpotential over the entire current den-

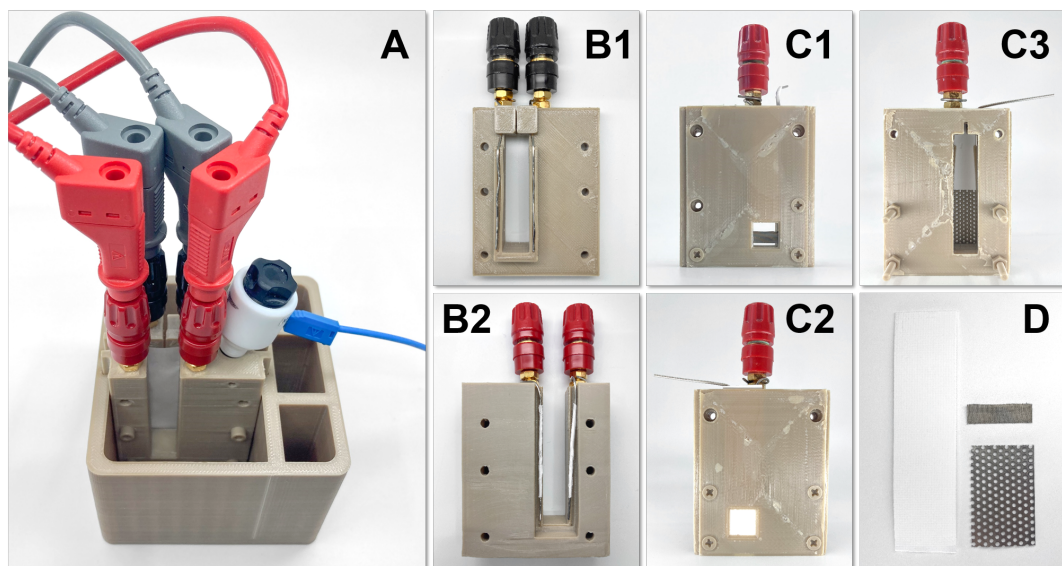


Fig. 3 A) Fully assembled cell setup (Zero-gap) B) Zero-gap accessories C) Fixed gap accessories D) Zirfon separator, Ni perforated plate CE, and Ni mesh WE.

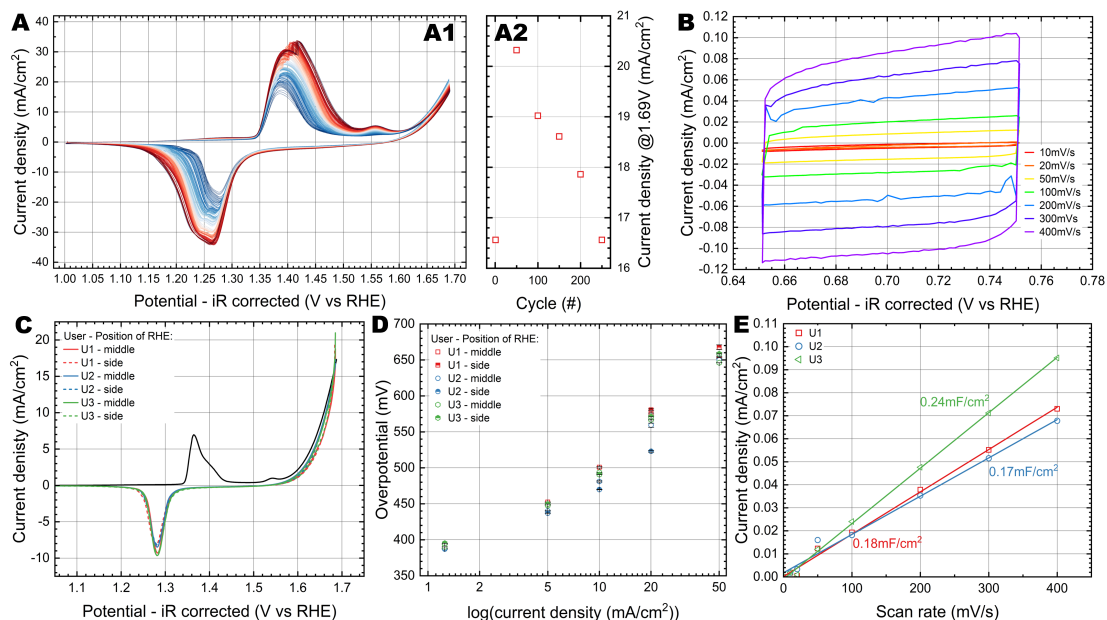


Fig. 4 All data has been recorded in Fe-free 1M KOH A1) Cyclic voltammetry (CV) for 250 cycles at a scan rate of 100mV/s A2) Evolution of current density at 1.69V vs. RHE with respect to cycle number B) Representative Cv recorded by U1 at different scan rates after 10min of constant N₂ bubbling for ECSA determination C) CV of cycle #50 and #250 by different users D) Linear sweep voltammetry recorded at 10mV/s by different users and different RE positions E) Plots of capacitive current density as a function of scan rate by different users.

sity range. The datapoint measured by U2 at 20 mA/cm² with the side placement of the RE seems to constitute an outlier with a recorded overpotential of approx. 50 mV lower.

Overall, these meticulous comparisons highlight the consistency and robustness of the designed holder.

Non zero gap configuration

Figure 5A displays the Linear Sweep Voltammetry (LSV) at 10 mV/s recorded by the three different users with a 3 mm gap between WE and separator. The cathodic scans exhibit similar onset potentials but display slight variations in their Tafel slope. This divergence may be attributed to differences in exposed wire area during the measurements, resulting in slightly higher surface areas for the first two measurements compared to the third. Nonetheless, the overall results are strikingly similar, featuring a prominent oxidation peak at 1.56 V vs RHE, akin to the zero gap configuration.

Upon comparing U3 results in the zero-gap and non-zero gap configurations (Figure 5B), a strong resemblance in the LSV profiles can be observed. Both configurations display similar oxidation/reduction peaks, albeit with a small penalty in activity for the non-zero-gap configuration. This is likely associated with i) increased electrolyte concentration polarization resulting in decreased pH at the WE and thereby reduced OER activity, and ii) sub-compensated iR contribution due to the bubble induced increased ohmic resistance of the electrolyte within the gap.

Moving to Figure 4C, we analyze the capacitive current density as a function of scan rate measured by all three users in the non-zero gap configuration. All three measurements exhibit comparable capacitance per area values of approx. 0.24 mF/cm², in line with the capacitance measured in the zero gap configuration.

The close resemblance between the non-zero gap and zero gap configurations suggests that the electrochemical behavior remains consistent, regardless of the gap setting. However, small deviations from the zero-gap behavior and a larger variance can be discerned when using the gap configuration. This finding is particularly noteworthy as it suggests that the zero-gap measurements are more reproducible and robust and should be preferred. It should be noted that the results are fully IR corrected and the resistance in the zero gap configuration is 50% lower (0.75 Ω) than in the non-zero gap configuration (1.5 Ω). The higher resistance in the non-zero gap setup is primarily due to the solution resistance scaling with the distance between the separator and the anode, as well as the inherent resistance of the separator material.

Conclusions

In conclusion, this paper introduces a customizable 3D-printable 3-electrode holder for use in zero-gap or controlled-gap configuration. It is exemplified for the case of OER on NiOOH in alkaline environment. This user-friendly holder demonstrates excellent reproducibility, consistent measurements amongst different users, and negligible influence from the placement of the reference electrode. The possibility of 3D printing with thermally and chemically resistant materials like PP and PEEK offers researchers a cost-effective, environmentally friendly, and adaptable holder,

facilitating exploration of new catalysts, electrodes, and cell geometries.

Author Contributions

We strongly encourage authors to include author contributions and recommend using CRediT for standardised contribution descriptions. Please refer to our general author guidelines for more information about authorship.

Conflicts of interest

There are no conflicts to declare.

Acknowledgements

The Acknowledgements come at the end of an article after Conflicts of interest and before the Notes and references.

Notes and references

- 1 R. Phillips and C. W. Dunnill, *RSC Advances*, 2016, **6**, 100643–100651.
- 2 J. W. Haverkort and H. Rajaei, *Journal of Power Sources*, 2021, **497**, 229864.
- 3 M. R. Kraglund, D. Aili, K. Jankova, E. Christensen, Q. Li and J. O. Jensen, *Journal of The Electrochemical Society*, 2016, **163**, F3125–F3131.
- 4 R. Dua, Z. Rashad, J. Spears, G. Dunn and M. Maxwell, *Polymers*, 2021, **13**, 1–15.
- 5 L. Trotochaud, S. L. Young, J. K. Ranney and S. W. Boettcher, *Journal of the American Chemical Society*, 2014, **136**, 6744–6753.
- 6 CreatBot, 2022, 2022.
- 7 D. A. Corrigan and S. P. Maheswari, *Electrochemical Society Extended Abstracts*, 1987, **85-1**, 934–935.
- 8 D. M. Morales and M. Risch, *JPhys Energy*, 2021, **3**, year.
- 9 Y. Cui, Y. Xue, R. Zhang, J. Zhang, X. Li and X. Zhu, *Journal of Materials Chemistry A*, 2019, **7**, 21911–21917.
- 10 X. Han, C. Yu, S. Zhou, C. Zhao, H. Huang, J. Yang, Z. Liu, J. Zhao and J. Qiu, *Advanced Energy Materials*, 2017, **7**, year.

1 Supplementary Information

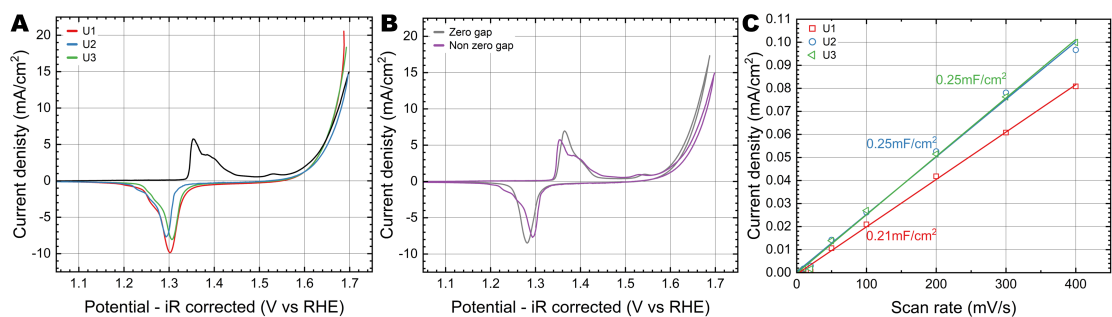


Fig. 5 All data has been recorded in Fe-free 1M KOH A) Linear sweep voltammetry recorded at 10mV/s by different users A) Linear sweep voltammetry recorded at 10mV/s comparing the two electrode configurations C) Plots of capacitive current density as a function of scan rate by different users.

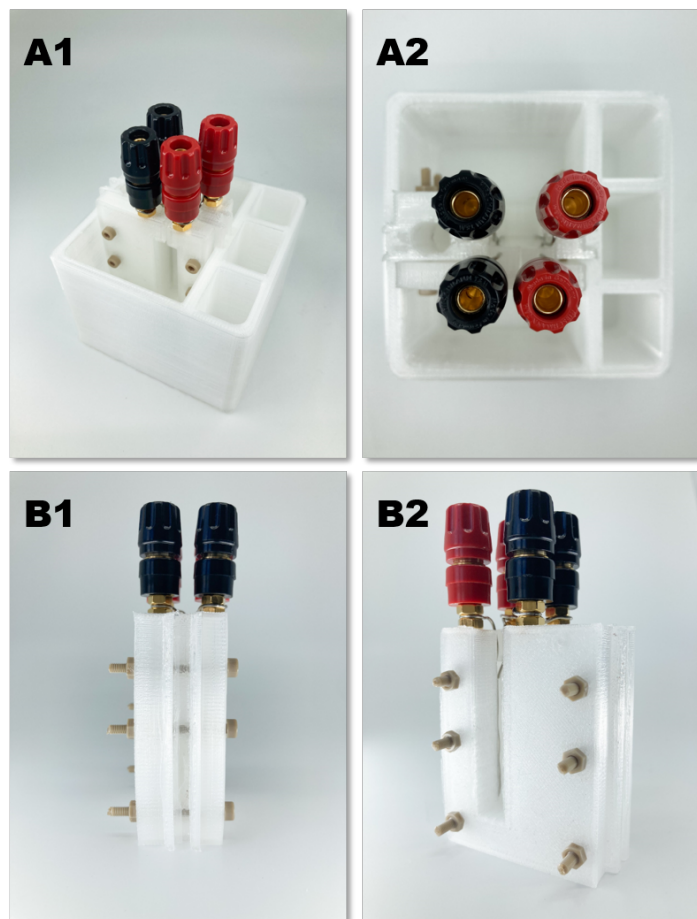


Fig. 6 A) Fully assembled cell setup (Zero-gap) B) Zero-gap accessories printed from polypropylene filament.

APPENDIX B

Drawings and pictures

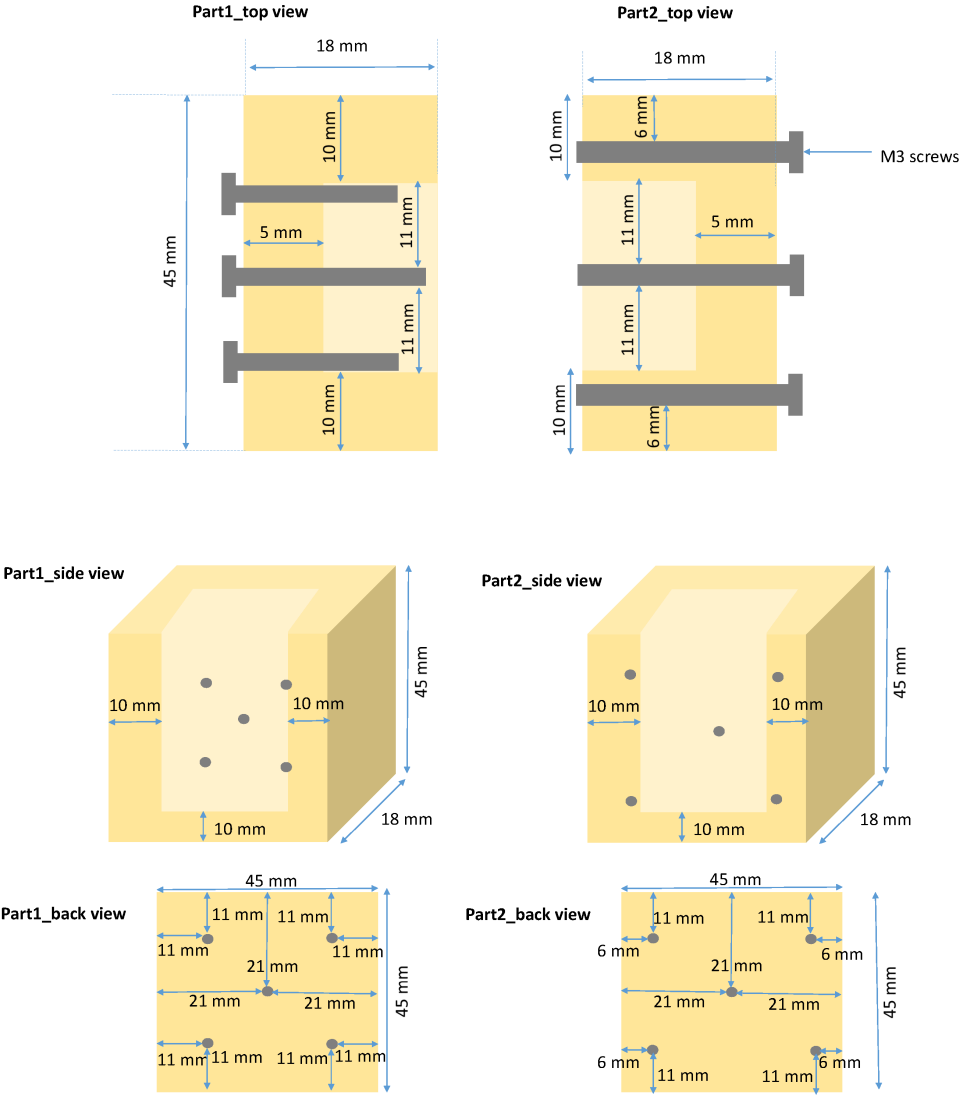
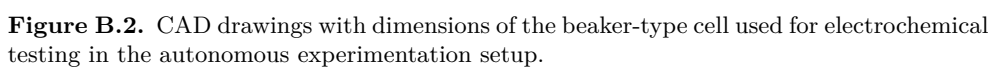
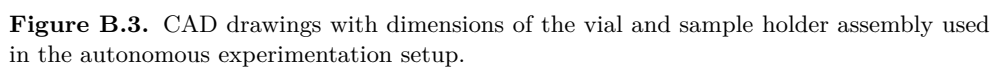


Figure B.1. Drawings with dimensions of planar near-zero-gap cell for electrochemical testing.





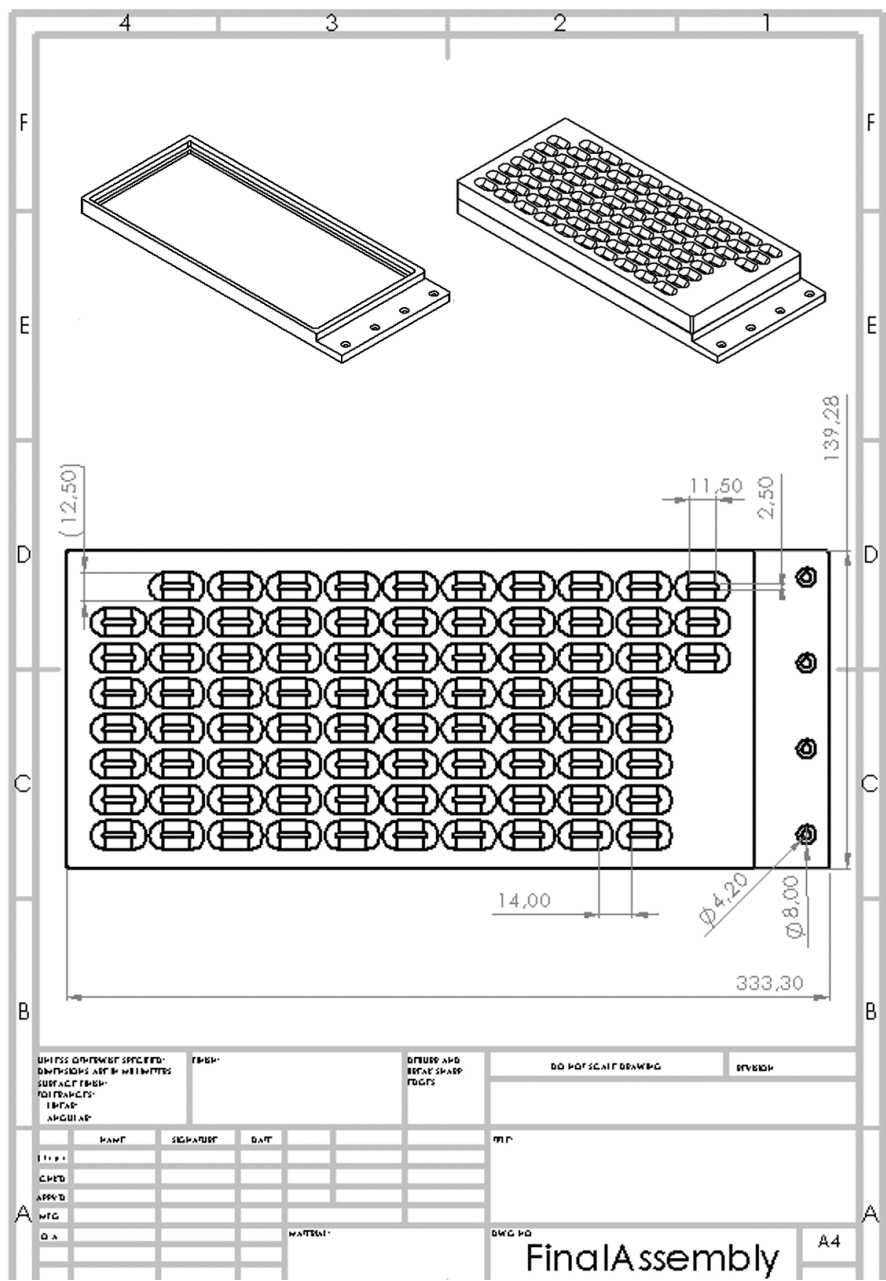
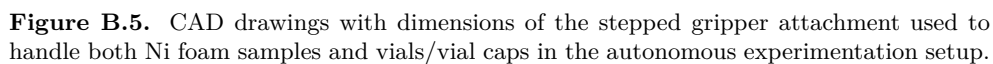


Figure B.4. CAD drawings with dimensions of the sample holder used in the autonomous experimentation setup.



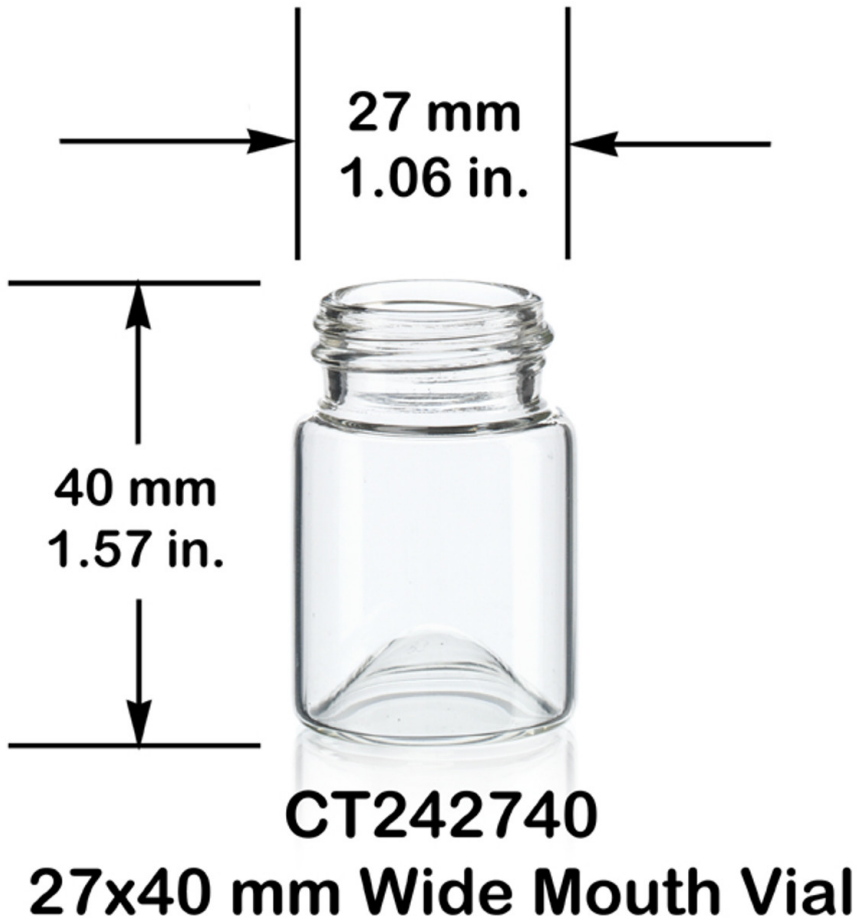


Figure B.6. Dimensions of glass vials used in autonomous experimentation setup. From <https://www.discountvials.com/wide-mouth-glass-vial-w-cap-27-x-40-mm/>.

List of Figures

1.1	Top: Historic data (1850-2020) showing the increase in atmospheric greenhouse gas concentrations caused by human activities and the resulting increase global surface temperature; Bottom: Vulnerability of countries with respect to effects of climate change vs. the respective national CO ₂ emissions per capita in 2019. Adapted from [2]	2
1.2	A: Global net addition of renewable energy sources (GW) (empirical for 2017-2022, projected for 2023-2024). B: Global energy supply by source (EJ) for 1971-2019. C: Relative contribution of renewable energy sources to the global energy supply for 2010-2022 and required contributions by 2030 according to the IEA's net zero scenario. Adapted from [6–8]	3
1.3	Relative curtailment of renewable energy in relation to their variable renewable energy (VRE) share for several countries (data from 2010-2022). Adapted from [6–8]	4
1.4	Comparison of different energy storage technologies in terms of discharge time, power rating and round-trip efficiency. From [12]	5
2.1	Schematic working principle of an alkaline electrolyzer.	10
2.2	Schematic working principle of an PEM electrolyzer.	13
2.3	Performance comparison of AEM, PEM and SOEC water electrolysis technologies. Thermoneutral voltages for splitting of steam ($E_{tn,steam} = 1.29$ V) and water ($E_{tn,water} = 1.47$ V) highlighted with dashed lines. Adapted from [23]	14
2.4	Schematic working principle of an solid oxide electrolyzer.	16
2.5	Global dryland areas with the coastal arid zones - potentially suitable for cheap hydrogen production from seawater - highlighted in red. From [44]	17

2.6	Pourbaix diagram for an artificial seawater model (aqueous electrolyte with 0.5M NaCl), showing the chlorine reactions competing with the OER in dependance of the pH. From [48]	19
2.7	Bode diagram illustrating the different crystal phases of Ni(OH) ₂ /NiOOH.	28
2.8	Autonomous robotic system for the investigation of yeast growth as described in [143]. Adapted from [144]	31
2.9	Batch screening of alkaline OER catalysts by means of laser-induced fluorescence of a stainless steel mesh coated with oxygen-sensitive paint. Adapted from [145]	32
2.10	Liquid handling organic synthesis robot for autonomous reactivity prediction. Adapted from [149]	33
2.11	Modified 3D-printer for the automated synthesis of ibuprofen. Adapted from [163]	34
2.12	Thin-film characterization and optimization by means of a multi-axis robotic arm. Adapted from [154]	35
2.13	Free-roaming multi-axis robotic platform for autonomous HER photocatalyst optimization. Adapted from [155]	36
3.1	Planar near-zero-gap cell.	39
3.2	3D rendering of N9 platform consisting of an aluminium table base (1), robotic arm (2) including gripper tool (3), liquid dispensing carousel (4) and vial clamp (5). Electrochemical test cell (6) and sample and vial holder (7) are custom parts developed in house. C9 controller not displayed.	40
3.3	Beaker-type electrochemical test cell for the automated test setup.	41
3.4	Cross-section of the electrochemical test cell.	42
3.5	Sample and vial holder assembly.	43
3.6	Stepped gripper machined from Aluminium.	44
3.7	Pump assemblies used in autonomous experimentation setup.	46
4.1	Schematic depiction of the co-precipitation synthesis process.	54
4.2	Heatmaps visualizing the overpotential at 10 mA cm ² (η_{10}) of all investigated compounds tested in 1 M KOH and 1 M KOH + 0.5 M NaCl (left). Comparison of the respective overpotential difference between the two electrolytes (right).	57

4.3	Overview of OER overpotential at 10 mA cm ² of Ni foam, Fe and the best Fe-free and Fe-containing samples in both electrolytes (A) as well as the corresponding anodic LSV scans (B). Comparison of the effect of the dopant on the overpotential of Fe compounds (C).	58
4.4	Surface layer composition measured by means of XPS analysis.	59
4.5	Ni foam surface after synthesis (A) and SEM-EDX image with elemental maps (B), indicating an even coating of the surface and homogeneous dispersion of the dopant in the deposition layer on the example of the FeCo sample. C-F: SEM images of Fe, FeCo, FeZn (250kx magnification) and FeAl (500kx magnification) samples. All samples show the petal-shaped surface structure characteristic for LDH-type materials, although the feature size is substantially smaller for the FeAl sample. G-H: SEM image and layered EDX maps of the FeCu sample showing phase separation of CuOx species decorating a NiFe surface.	61
4.6	FTIR spectra showing the intercalation of CO ₃ ²⁻ when 3+ ions are present in the deposition layer, indicating LDH formation.	62
4.7	XPS spectra of Ni2p and Fe2p from Fe sample; 2p spectra of the other metals from the respective Fe containing samples.	63
4.8	XRD patterns of Fe compounds. All samples show the characteristic NiFe-LDH peaks (PDF no. 40-0215).	64
5.1	Schematic illustration of the NiFe LDH structure. The divalent (Ni) and trivalent (Fe) ions as well as the interlayer anions can be replaced by a wide range of different elements. Adapted from [7].	77
5.2	Illustration of the synthesis procedure used for the autonomous experiment.	80
5.3	Schematic of the setup used for the autonomous catalyst development experiment.	83
5.4	3D model cross-section of the electrochemical test cell.	85
5.5	Data quality obtained with the experimental setup on the example of an Fe sample (ID650).	86
5.6	ECSA conditioning and measurement steps indicating technical issues with the potentiostat.	87
5.7	Heat map of linear grid screening results.	88

5.8	Bare Ni foam tested before and after testing an Fe sample with sonication during cleaning, showing no signs of contamination (A). For comparison, Ni sample tested in Fe contaminated environment and Fe free Ni sample (B). Reproducibility of results on the example of five Fe samples (C). Effect of adding one (D), two (E), and several dopants (F) to the Ni substrate. All CVs recorded with a scan rate of 10 mV s ⁻¹	90
5.9	The autonomous experimentation platform.	98
5.10	Assortment of (mostly 3D-printed) prototypes of sample holders, cell bases, lids and terminals, racks, caps, grippers, vials and others.	99
5.11	Decision tree based on a seemingly simply technical issue, illustrating the complexity of fail-proofing autonomous lab systems.	100
6.1	The optimization process can be described by an iterative loop of five steps. (1) Electrodes are synthesized in batches of 5-6 according to section 2.1.2. (2) Electrodes are tested and characterized using the method described in section 2.1.3 and 2.1.4. (3) The used synthesis parameters and performance metric (η at 10 mA cm ⁻²) are fed into a database. (4) Bayesian optimization, including a sensitivity analysis, is conducted using the database, resulting in a heat map of mean predicted overpotentials for any given combination of synthesis parameters. (5) Synthesis parameters for next batch are chosen manually based on the heat map (human in the loop). The drawing of the setup has been created with Chemix (https://chemix.org).	113
6.2	SEM images illustrating how the synthesis parameters; t (a-c), i (d-f) and T (g-i) changes the deposited microstructure. From a-c the microstructure visually does not change suggesting that t only creates a thicker layer. From d-f the spike length decreases with increasing i, while the microstructure from g-i changes drastically from almost flat and sandpaper-like at low and intermediate T to spiky at high T.	114
6.3	η_{10} (blue) and R_f (red) as function of t, i and T. With the chosen parameters the i appears to be the most sensitive synthesis parameter, followed by time and T. η_{10} generally decreases with increasing R_f	115

6.4	Illustration of the established G_P , σ_{GP} and a plot of f_{acq} , the ladder used to identify promising synthesis parameters. The model is based on known data points (31, 36 and 40 data points for iteration 1, 2 and 3 respectively) and shows the predicted η_{10} as function of T and i. Brighter colors indicate a low η_{10} and thus a good electrode performance. The figure shows that the prediction changes slightly and that the uncertainty is lowered with increasing number of iterations and samples.	117
6.5	SEM image of sample 4's surface showing rough sandpaper-like features, which are hard to resolve further by SEM.	118
6.6	Smoothened LSV curves for the substrate (red), Ni foam (yellow), Pt-foil (blue), best performing sample (sample 4, green) and Raney NiMo (NiMo, purple).	119
6.7	Illustration of f_{acq} used to identify promising synthesis parameters. The model is based on known data points from Table S2 and shows the predicted η_{10} as function of four parameters, T, i, t and EDA concentration. Brighter colors indicate a low η_{10} and thus a good electrode performance.	120
6.8	Recorded control sample LSV curves.	127
6.9	Parameter distribution. The parameter space consists of many repeated values and do not cover the entire parameter space.	129
6.10	Summary of the sensitivity analysis. The values in the plot have been normalized. Unlike the parameter study T has been identified as the most sensitive synthesis parameter, while t is an insignificant parameter.	130
6.11	Two samples synthesised using the same i and T during deposition but different t The performance of the two samples at 10 mA cm ⁻² is practically the same.	130
6.12	The R_f vs. η_{10} at 10 mA cm ⁻² in a semi-logarithmic plot. The data have been fitted and a prediction band added. The Figure illustrates that a linear relationship between the R_f and η_{10} must exist.	131
6.13	Example of an XPS survey scan from an electrodeposited sample (T = 57 °C, t = 30 min, i = 36 mA cm ⁻²). There is no evidence for any impurity phases from the deposition process in the samples.	133
B.1	Drawings with dimensions of planar near-zero-gap cell for electrochemical testing.	148

B.2	CAD drawings with dimensions of the beaker-type cell used for electrochemical testing in the autonomous experimentation setup.	149
B.3	CAD drawings with dimensions of the vial and sample holder assembly used in the autonomous experimentation setup.	150
B.4	CAD drawings with dimensions of the sample holder used in the autonomous experimentation setup.	151
B.5	CAD drawings with dimensions of the stepped gripper attachment used to handle both Ni foam samples and vials/vial caps in the autonomous experimentation setup.	152
B.6	Dimensions of glass vials used in autonomous experimentation setup. From https://www.discountvials.com/wide-mouth-glass-vial-w-cap-27-x-40-mm/	153

List of Tables

2.1	Typical operation conditions of state-of-the-art alkaline, PEM and SOEC electrolyzers [21–23]. Values marked with * are estimated from Figure 2.3.	11
2.2	Reversible E_{rev} , and thermoneutral E_{tn} cell potentials for various temperatures at standard pressure.	21
2.3	List of representative non-noble metal-based electrocatalysts for the alkaline HER at room temperature (η_{10} = overpotential at 10 mA cm ⁻² , RT = room temperature, C_{dl} = double layer capacitance). CC = carbon cloth, GCE = glassy carbon electrode, CMF = carbon micro flowers, NS = nanosheets, DG = defective graphene, CNT = carbon nano tube, PP = pressed powder, SP = sintered powder. ^a η measured at 20 mA cm ⁻² , ^b η measured at 250 mA cm ⁻²	25
2.4	List of representative non-noble metal-based electrocatalysts for the alkaline OER at room temperature (η_{10} = overpotential at 10 mA cm ⁻² , RT = room temperature, C_{dl} = double layer capacitance).	30
5.1	Electrochemical test sequence used in this study.	82

6.1	The composition and operating condition intervals of the solution used for electrodepositing nano-structured Ni.	110
6.2	Complete list of all the samples synthesized during the 3 iterations of the BO loop. In the table the measured η_{10} and R_f has been included as well.	117
6.3	Short overview of different state of the art Ni electrodes. All electrodes have been synthesised using an electrodeposition method. The electrodes listed in the table have been tested in KOH at room temperature. Values marked with * have been determined manually from LSV curves.	119
6.4	Summary of all samples synthesised. In the table the synthesis parameters have been included together with the individual sample's η_{10} and R_f . . .	128
6.5	Summary of all samples synthesised in the additional study (section 3.3) with four parameters. In the table the synthesis parameters have been included together with the individual sample's η_{10} and R_f	132

Bibliography

- [1] U. Nations, “What is climate change?” <https://www.un.org/en/climatechange/what-is-climate-change>. Accessed: 2023-09-06.
- [2] IPCC, “SYNTHESIS REPORT OF THE IPCC SIXTH ASSESSMENT REPORT (AR6),” tech. rep., Intergovernmental Panel on Climate Change, 2023.
- [3] P. Malanima, “World Energy Consumption: A Database. 1820–2018,” tech. rep., Harvard University, 2020.
- [4] F. Birol, “Key World Energy Statistics 2021 – Statistics Report,” tech. rep., International Energy Agency, 2021.
- [5] W. H. Organization, “Ambient (outdoor) air pollution.” [https://www.who.int/news-room/fact-sheets/detail/ambient-\(outdoor\)-air-quality-and-health](https://www.who.int/news-room/fact-sheets/detail/ambient-(outdoor)-air-quality-and-health). Accessed: 2023-09-11.
- [6] I. E. Agency, “Net renewable electricity capacity additions by technology, 2017-2024.” <https://www.iea.org/data-and-statistics/charts/net-renewable-electricity-capacity-additions-by-technology-2017-2024>. Accessed: 2023-09-17.
- [7] I. E. Agency, “World total energy supply by source, 1971-2019.” <https://www.iea.org/data-and-statistics/charts/world-total-energy-supply-by-source-1971-2019>. Accessed: 2023-09-17.
- [8] I. E. Agency, “Renewables share of total energy supply in the net zero scenario, 2010-2030.” <https://www.iea.org/data-and-statistics/charts/renewables-share-of-total-energy-supply-in-the-net-zero-scenario-2010-2030-2>. Accessed: 2023-09-17.

- [9] I. E. Agency, “Vre shares in generation and technical curtailment for selected countries.” <https://www.iea.org/data-and-statistics/charts/vre-shares-in-generation-and-technical-curtailment-for-selected-countries>. Accessed: 2023-09-17.
- [10] D. Jefferies, “Pumped storage,” in *Pumped storage* (T. Douglas, ed.), Institution of Civil Engineers, Thomas Telford Ltd, 1990.
- [11] I. E. Agency, “Grid-scale storage.” <https://www.iea.org/energy-system/electricity/grid-scale-storage>. Accessed: 2023-09-17.
- [12] B. Decourt, B. Lajoie, R. Debarre, and O. Soupa, “Hydrogen-Based Energy Conversion More than storage: System flexibility,” Tech. Rep. February, SBC Energy Institute, 2014.
- [13] A. Nurdiawati and F. Urban, “Towards deep decarbonisation of energy-intensive industries: A review of current status, technologies and policies,” *Energies*, vol. 14, no. 9, p. 2408, 2021.
- [14] A. Escamilla, D. Sánchez, and L. García-Rodríguez, “Assessment of power-to-power renewable energy storage based on the smart integration of hydrogen and micro gas turbine technologies,” *International Journal of Hydrogen Energy*, vol. 47, pp. 17505–17525, may 2022.
- [15] T. Gül, U. Remme, and J. M. Bermudez Menendez, “Global Hydrogen Review 2021,” tech. rep., International Energy Agency (IEA), 2021.
- [16] G. F. Swiegers, A. L. Hoang, A. Hodges, G. Tsekouras, C. Y. Lee, K. Wagner, and G. Wallace, “Current status of membraneless water electrolysis cells,” *Current Opinion in Electrochemistry*, vol. 32, p. 100881, 2022.
- [17] K. Zeng and D. Zhang, “Recent progress in alkaline water electrolysis for hydrogen production and applications,” *Progress in Energy and Combustion Science*, vol. 36, pp. 307–326, jun 2010.
- [18] R. Chaubey, S. Sahu, O. O. James, and S. Maity, “A review on development of industrial processes and emerging techniques for production of hydrogen from renewable and sustainable sources,” *Renewable and Sustainable Energy Reviews*, vol. 23, pp. 443–462, 2013.

- [19] M. David, C. Ocampo-Martínez, and R. Sánchez-Peña, “Advances in alkaline water electrolyzers: A review,” *Journal of Energy Storage*, vol. 23, pp. 392–403, jun 2019.
- [20] I. R. E. Agency, “Hydrogen production overview.” <https://www.irena.org/Energy-Transition/Technology/Hydrogen>. Accessed: 2023-09-04.
- [21] J. C. Ehlers, A. A. Feidenhans'l, K. T. Therkildsen, and G. O. Larrazábal, “Affordable Green Hydrogen from Alkaline Water Electrolysis: Key Research Needs from an Industrial Perspective,” *ACS Energy Letters*, vol. 8, no. 3, pp. 1502–1509, 2023.
- [22] M. Carmo, D. L. Fritz, J. Mergel, and D. Stolten, “A comprehensive review on PEM water electrolysis,” *International Journal of Hydrogen Energy*, vol. 38, pp. 4901–4934, apr 2013.
- [23] A. Hauch, R. Küngas, P. Blennow, A. B. Hansen, J. B. Hansen, B. V. Mathiesen, and M. B. Mogensen, “Recent advances in solid oxide cell technology for electrolysis,” *Science*, vol. 370, no. 6513, 2020.
- [24] L. P. Allen, J. Baez, M. E. C. Stern, K. Takahashi, and F. George, “Trends and the economic effect of asbestos bans and decline in asbestos consumption and production worldwide,” *International Journal of Environmental Research and Public Health*, vol. 15, no. 3, 2018.
- [25] J. Brauns, J. Schönebeck, M. R. Kraglund, D. Aili, J. Hnát, J. Žitka, W. Mues, J. O. Jensen, K. Bouzek, and T. Turek, “Evaluation of Diaphragms and Membranes as Separators for Alkaline Water Electrolysis,” *Journal of The Electrochemical Society*, vol. 168, no. 1, p. 014510, 2021.
- [26] P. Vermeiren, R. Leysen, H. Beckers, J. P. Moreels, and A. Claes, “The influence of manufacturing parameters on the properties of macroporous Zirfon® separators,” *Journal of Porous Materials*, vol. 15, no. 3, pp. 259–264, 2008.
- [27] A. Hauch, S. D. Ebbesen, S. H. Jensen, and M. Mogensen, “Highly efficient high temperature electrolysis,” *Journal of Materials Chemistry*, vol. 18, no. 20, pp. 2331–2340, 2008.
- [28] J. C. Ganley, “High temperature and pressure alkaline electrolysis,” *International Journal of Hydrogen Energy*, vol. 34, no. 9, pp. 3604–3611, 2009.

- [29] F. Allebrod, C. Chatzichristodoulou, and M. B. Mogensen, "Alkaline electrolysis cell at high temperature and pressure of 250 °c and 42 bar," *Journal of Power Sources*, vol. 229, pp. 22–31, 2013.
- [30] S. D. Ebbesen, S. H. Jensen, A. Hauch, and M. B. Mogensen, "High temperature electrolysis in alkaline cells, solid proton conducting cells, and solid oxide cells," *Chemical Reviews*, vol. 114, no. 21, pp. 10697–10734, 2014.
- [31] I. Vincent and D. Bessarabov, "Low cost hydrogen production by anion exchange membrane electrolysis: A review," *Renewable and Sustainable Energy Reviews*, vol. 81, pp. 1690–1704, jan 2018.
- [32] Y. Leng, G. Chen, A. J. Mendoza, T. B. Tighe, M. A. Hickner, and C. Y. Wang, "Solid-state water electrolysis with an alkaline membrane," *Journal of the American Chemical Society*, vol. 134, no. 22, pp. 9054–9057, 2012.
- [33] Verdagycy, "Industrial hydrogen electrolyzers that scale." <https://verdagy.com/edynamic/>. Accessed: 2023-09-23.
- [34] U. Babic, M. Suermann, F. N. Büchi, L. Gubler, and T. J. Schmidt, "Critical Review—Identifying Critical Gaps for Polymer Electrolyte Water Electrolysis Development," *Journal of The Electrochemical Society*, vol. 164, no. 4, pp. F387–F399, 2017.
- [35] P. C. Vesborg and T. F. Jaramillo, "Addressing the terawatt challenge: scalability in the supply of chemical elements for renewable energy," *Rsc Advances*, vol. 2, no. 21, pp. 7933–7947, 2012.
- [36] W. Dönitz and E. Erdle, "High-temperature electrolysis of water vapor-status of development and perspectives for application," *International Journal of Hydrogen Energy*, vol. 10, no. 5, pp. 291–295, 1985.
- [37] E. D. Wachsman and K. T. Lee, "Lowering the temperature of solid oxide fuel cells," *Science*, vol. 334, no. 6058, pp. 935–939, 2011.
- [38] P. Hjalmarsson, X. Sun, Y.-L. Liu, and M. Chen, "Durability of high performance ni–yttria stabilized zirconia supported solid oxide electrolysis cells at high current density," *Journal of Power Sources*, vol. 262, pp. 316–322, 2014.

- [39] A. Ploner, A. Hauch, S. Pylypko, S. D. Iorio, G. Cubizolles, and J. Mougin, “Optimization of solid oxide cells and stacks for reversible operation,” *ECS Transactions*, vol. 91, p. 2517, jul 2019.
- [40] R. Tichler, H. Böhm, A. Zauner, S. Goers, and P. Kroon, “Innovative large-scale energy storage technologies and Power-to-Gas concepts after optimization Report on experience curves and economies of scale (M32) Deliverable Number D7.5 WP Number WP7: Reducing Barriers Responsible Report on experience curves and ,” Tech. Rep. 691797, STORE&GO, 2018.
- [41] J. Brauns and T. Turek, “Alkaline water electrolysis powered by renewable energy: A review,” *Processes*, vol. 8, no. 2, 2020.
- [42] O. Schmidt, A. Gambhir, I. Staffell, A. Hawkes, J. Nelson, and S. Few, “Future cost and performance of water electrolysis: An expert elicitation study,” *International journal of hydrogen energy*, vol. 42, no. 52, pp. 30470–30492, 2017.
- [43] S. Siegemund, M. Trommler, P. Schmidt, W. Weindorf, W. Zittel, T. Raksha, and J. Zerhusen, “The potential of electricity-based fuels for low-emission transport in the EU - An expertise by LBST and dena,” tech. rep., German Energy Agency, 2017.
- [44] S. Dresp, F. Dionigi, M. Klingenhof, and P. Strasser, “Direct electrolytic splitting of seawater: Opportunities and challenges,” *ACS Energy Letters*, vol. 4, no. 4, pp. 933–942, 2019.
- [45] T. Younos and K. E. Tulou, “Overview of Techniques Overview of Desalination Techniques,” *JOURNAL OF CONTEMPORARY WATER RESEARCH & EDUCATION*, vol. 132, no. 1, pp. 3–10, 2005.
- [46] M. A. Khan, T. Al-Attas, S. Roy, M. M. Rahman, N. Ghaffour, V. Thangadurai, S. Larter, J. Hu, P. M. Ajayan, and M. G. Kibria, “Seawater electrolysis for hydrogen production: A solution looking for a problem?,” *Energy and Environmental Science*, vol. 14, no. 9, pp. 4831–4839, 2021.
- [47] J. N. Hausmann, R. Schlögl, P. W. Menezes, and M. Driess, “Is direct seawater splitting economically meaningful?,” *Energy and Environmental Science*, vol. 14, no. 7, pp. 3679–3685, 2021.

- [48] F. Dionigi, T. Reier, Z. Pawolek, M. Gliech, and P. Strasser, "Design Criteria, Operating Conditions, and Nickel-Iron Hydroxide Catalyst Materials for Selective Seawater Electrolysis," *ChemSusChem*, vol. 9, no. 9, pp. 962–972, 2016.
- [49] S. Dresch, T. Ngo Thanh, M. Klingenhof, S. Brückner, P. Hauke, and P. Strasser, "Efficient direct seawater electrolyzers using selective alkaline NiFe-LDH as OER catalyst in asymmetric electrolyte feeds," *Energy and Environmental Science*, vol. 13, no. 6, pp. 1725–1729, 2020.
- [50] M. L. Frisch, T. N. Thanh, A. Arinchtin, L. Hager, J. Schmidt, S. Brückner, J. Kerres, and P. Strasser, "Seawater Electrolysis Using All-PGM-Free Catalysts and Cell Components in an Asymmetric Feed," *ACS Energy Letters*, vol. 8, no. 5, pp. 2387–2394, 2023.
- [51] T. Okada, H. Abe, A. Murakami, T. Shimizu, K. Fujii, T. Wakabayashi, and M. Nakayama, "A Bilayer Structure Composed of Mg|Co-MnO₂ Deposited on a Co(OH)₂ Film to Realize Selective Oxygen Evolution from Chloride-Containing Water," *Langmuir*, vol. 36, no. 19, pp. 5227–5235, 2020.
- [52] H. Xie, Z. Zhao, T. Liu, Y. Wu, C. Lan, W. Jiang, L. Zhu, Y. Wang, D. Yang, and Z. Shao, "A membrane-based seawater electrolyser for hydrogen generation," *Nature*, vol. 612, no. 7941, pp. 673–678, 2022.
- [53] J. Guo, Y. Zheng, Z. Hu, C. Zheng, J. Mao, K. Du, M. Jaroniec, S. Z. Qiao, and T. Ling, "Direct seawater electrolysis by adjusting the local reaction environment of a catalyst," *Nature Energy*, vol. 8, no. 3, pp. 264–272, 2023.
- [54] F. Safizadeh, E. Ghali, and G. Houlachi, "Electrocatalysis developments for hydrogen evolution reaction in alkaline solutions - A Review," *International Journal of Hydrogen Energy*, vol. 40, no. 1, pp. 256–274, 2015.
- [55] L. Birry and A. Lasia, "Studies of the hydrogen evolution reaction on Raney nickel-molybdenum electrodes," *Journal of Applied Electrochemistry*, vol. 34, no. 7, pp. 735–749, 2004.
- [56] Y. Zheng, Y. Jiao, A. Vasileff, and S. Z. Qiao, "The Hydrogen Evolution Reaction in Alkaline Solution: From Theory, Single Crystal Models, to Practical Electrocatalysts," *Angewandte Chemie - International Edition*, vol. 57, no. 26, pp. 7568–7579, 2018.

- [57] J. K. Nørskov, T. Bligaard, A. Logadottir, J. R. Kitchin, J. G. Chen, S. Pandelov, and U. Stimming, "Trends in the Exchange Current for Hydrogen Evolution," *Journal of The Electrochemical Society*, vol. 152, no. 3, p. J23, 2005.
- [58] Y. Wang, G. Zhang, W. Xu, P. Wan, Z. Lu, Y. Li, and X. Sun, "A 3d nanoporous ni-mo electrocatalyst with negligible overpotential for alkaline hydrogen evolution," *ChemElectroChem*, vol. 1, no. 7, pp. 1138–1144, 2014.
- [59] T.-K. Yang, D.-S. Lee, and J. Haas, "Raney nickel," *Encyclopedia of Reagents for Organic Synthesis*, 2001.
- [60] P. Los, A. Rami, and A. Lasia, "Hydrogen evolution reaction on ni-al electrodes," *Journal of applied electrochemistry*, vol. 23, pp. 135–140, 1993.
- [61] X. Yang, A.-Y. Lu, Y. Zhu, M. N. Hedhili, S. Min, K.-W. Huang, Y. Han, and L.-J. Li, "Cop nanosheet assembly grown on carbon cloth: A highly efficient electrocatalyst for hydrogen generation," *Nano Energy*, vol. 15, pp. 634–641, 2015.
- [62] H. Vrubel and X. Hu, "Molybdenum boride and carbide catalyze hydrogen evolution in both acidic and basic solutions," *Angewandte Chemie International Edition*, vol. 51, no. ARTICLE, pp. 12703–12706, 2012.
- [63] Y. Huang, Q. Gong, X. Song, K. Feng, K. Nie, F. Zhao, Y. Wang, M. Zeng, J. Zhong, and Y. Li, "Mo2c nanoparticles dispersed on hierarchical carbon microflowers for efficient electrocatalytic hydrogen evolution," *ACS nano*, vol. 10, no. 12, pp. 11337–11343, 2016.
- [64] S. Gupta, N. Patel, R. Fernandes, S. Hanchate, A. Miotello, and D. Kothari, "Co-mo-b nanoparticles as a non-precious and efficient bifunctional electrocatalyst for hydrogen and oxygen evolution," *Electrochimica Acta*, vol. 232, pp. 64–71, 2017.
- [65] Z. Peng, S. Yang, D. Jia, P. Da, P. He, A. M. Al-Enizi, G. Ding, X. Xie, and G. Zheng, "Homologous metal-free electrocatalysts grown on three-dimensional carbon networks for overall water splitting in acidic and alkaline media," *Journal of Materials Chemistry A*, vol. 4, no. 33, pp. 12878–12883, 2016.
- [66] Y. Jia, L. Zhang, G. Gao, H. Chen, B. Wang, J. Zhou, M. T. Soo, M. Hong, X. Yan, G. Qian, *et al.*, "A heterostructure coupling of exfoliated ni-fe hydroxide

- nanosheet and defective graphene as a bifunctional electrocatalyst for overall water splitting,” *Advanced Materials*, vol. 29, no. 17, p. 1700017, 2017.
- [67] Y. Jin, X. Yue, C. Shu, S. Huang, and P. K. Shen, “Three-dimensional porous moni 4 networks constructed by nanosheets as bifunctional electrocatalysts for overall water splitting,” *Journal of Materials Chemistry A*, vol. 5, no. 6, pp. 2508–2513, 2017.
- [68] C. Tang, N. Cheng, Z. Pu, W. Xing, and X. Sun, “Nise nanowire film supported on nickel foam: an efficient and stable 3d bifunctional electrode for full water splitting,” *Angewandte Chemie*, vol. 127, no. 32, pp. 9483–9487, 2015.
- [69] R. Zhang, X. Wang, S. Yu, T. Wen, X. Zhu, F. Yang, X. Sun, X. Wang, and W. Hu, “Ternary nico2px nanowires as ph-universal electrocatalysts for highly efficient hydrogen evolution reaction,” *Advanced materials*, vol. 29, no. 9, p. 1605502, 2017.
- [70] G.-F. Chen, T. Y. Ma, Z.-Q. Liu, N. Li, Y.-Z. Su, K. Davey, and S.-Z. Qiao, “Efficient and stable bifunctional electrocatalysts ni/nixmy (m= p, s) for overall water splitting,” *Advanced Functional Materials*, vol. 26, no. 19, pp. 3314–3323, 2016.
- [71] S. A. Abbas, M. I. Iqbal, S.-H. Kim, and K.-D. Jung, “Catalytic activity of urchin-like ni nanoparticles prepared by solvothermal method for hydrogen evolution reaction in alkaline solution,” *Electrochimica Acta*, vol. 227, pp. 382–390, 2017.
- [72] J. Luo, J.-H. Im, M. T. Mayer, M. Schreier, M. K. Nazeeruddin, N.-G. Park, S. D. Tilley, H. J. Fan, and M. Grätzel, “Water photolysis at 12.3% efficiency via perovskite photovoltaics and earth-abundant catalysts,” *Science*, vol. 345, no. 6204, pp. 1593–1596, 2014.
- [73] L. Birry and A. Lasia, “Studies of the hydrogen evolution reaction on raney nickel—molybdenum electrodes,” *Journal of applied electrochemistry*, vol. 34, pp. 735–749, 2004.
- [74] J. O. Bockris, “Kinetics of Activation Controlled Consecutive Electrochemical Reactions: Anodic Evolution of Oxygen,” *The Journal of Chemical Physics*, vol. 24, pp. 817–827, apr 1956.

- [75] J. O. Bockris and T. Otagawa, "The electrocatalysis of oxygen evolution on perovskites," *Journal of The Electrochemical Society*, vol. 131, no. 2, p. 290, 1984.
- [76] M. W. Breiter, *Proceedings of the Symposium on Electrocatalysis*. Physical Electrochemistry Division, Electrochemical Society, 1974.
- [77] J. Rossmeisl, A. Logadottir, and J. Nørskov, "Electrolysis of water on (oxidized) metal surfaces," *Chemical Physics*, vol. 319, no. 1, pp. 178–184, 2005. Molecular Charge Transfer in Condensed Media - from Physics and Chemistry to Biology and Nanoengineering in honour of Alexander M. Kuznetsov on his 65th birthday.
- [78] J. Rossmeisl, Z.-W. Qu, H. Zhu, G.-J. Kroes, and J. K. Nørskov, "Electrolysis of water on oxide surfaces," *Journal of Electroanalytical Chemistry*, vol. 607, no. 1-2, pp. 83–89, 2007.
- [79] I. C. Man, H. Y. Su, F. Calle-Vallejo, H. A. Hansen, J. I. Martínez, N. G. Inoglu, J. Kitchin, T. F. Jaramillo, J. K. Nørskov, and J. Rossmeisl, "Universality in Oxygen Evolution Electrocatalysis on Oxide Surfaces," *ChemCatChem*, vol. 3, no. 7, pp. 1159–1165, 2011.
- [80] S. Iqbal, B. Safdar, I. Hussain, K. Zhang, and C. Chatzichristodoulou, "Trends and Prospects of Bulk and Single-Atom Catalysts for the Oxygen Evolution Reaction," *Advanced Energy Materials*, vol. 13, no. 17, 2023.
- [81] E. Guerrini, H. Chen, and S. Trasatti, "Oxygen evolution on aged irO_x/Ti electrodes in alkaline solutions," *Journal of Solid State Electrochemistry*, vol. 11, pp. 939–945, 2007.
- [82] Y. Tong, P. Chen, T. Zhou, K. Xu, W. Chu, C. Wu, and Y. Xie, "A bifunctional hybrid electrocatalyst for oxygen reduction and evolution: Cobalt oxide nanoparticles strongly coupled to b,n-decorated graphene," *Angewandte Chemie International Edition*, vol. 56, no. 25, pp. 7121–7125, 2017.
- [83] Z. Wu, Z. Zou, J. Huang, and F. Gao, "Fe-doped NiO mesoporous nanosheets array for highly efficient overall water splitting," *Journal of Catalysis*, vol. 358, pp. 243–252, 2018.

- [84] Y. Duan, S. Sun, Y. Sun, S. Xi, X. Chi, Q. Zhang, X. Ren, J. Wang, S. J. H. Ong, Y. Du, *et al.*, “Mastering surface reconstruction of metastable spinel oxides for better water oxidation,” *Advanced materials*, vol. 31, no. 12, p. 1807898, 2019.
- [85] T. Ma, C. Li, X. Chen, F. Cheng, and J. Chen, “Spinel cobalt–manganese oxide supported on non-oxidized carbon nanotubes as a highly efficient oxygen reduction/evolution electrocatalyst,” *Inorganic Chemistry Frontiers*, vol. 4, no. 10, pp. 1628–1633, 2017.
- [86] W. Liu, J. Bao, L. Xu, M. Guan, and Y. Lei, “Chromium-modulated multifunctional electrocatalytic activities of spinel oxide for zn-air batteries and overall water splitting,” *Journal of Power Sources*, vol. 479, p. 229099, 2020.
- [87] H. Xu, J. Yuan, G. He, and H. Chen, “Current and future trends for spinel-type electrocatalysts in electrocatalytic oxygen evolution reaction,” *Coordination Chemistry Reviews*, vol. 475, p. 214869, 2023.
- [88] S. Peng, F. Gong, L. Li, D. Yu, D. Ji, T. Zhang, Z. Hu, Z. Zhang, S. Chou, Y. Du, *et al.*, “Necklace-like multishelled hollow spinel oxides with oxygen vacancies for efficient water electrolysis,” *Journal of the American Chemical Society*, vol. 140, no. 42, pp. 13644–13653, 2018.
- [89] Y. Sun, R. Li, X. Chen, J. Wu, Y. Xie, X. Wang, K. Ma, L. Wang, Z. Zhang, Q. Liao, *et al.*, “A-site management prompts the dynamic reconstructed active phase of perovskite oxide oer catalysts,” *Advanced Energy Materials*, vol. 11, no. 12, p. 2003755, 2021.
- [90] T. X. Nguyen, Y.-C. Liao, C.-C. Lin, Y.-H. Su, and J.-M. Ting, “Advanced high entropy perovskite oxide electrocatalyst for oxygen evolution reaction,” *Advanced Functional Materials*, vol. 31, no. 27, p. 2101632, 2021.
- [91] J. Xiong, H. Zhong, J. Li, X. Zhang, J. Shi, W. Cai, K. Qu, C. Zhu, Z. Yang, S. P. Beckman, *et al.*, “Engineering highly active oxygen sites in perovskite oxides for stable and efficient oxygen evolution,” *Applied Catalysis B: Environmental*, vol. 256, p. 117817, 2019.
- [92] Y. Da, L. Zeng, C. Wang, C. Gong, and L. Cui, “A simple approach to tailor oer activity of $\text{Sr}_{1-x}\text{Co}_x\text{O}_{3-\delta}$ perovskite catalysts,” *Electrochimica Acta*, vol. 300, pp. 85–92, 2019.

- [93] H. Jo, Y. Yang, A. Seong, D. Jeong, J. Kim, S. H. Joo, Y. J. Kim, L. Zhang, Z. Liu, J.-Q. Wang, *et al.*, "Promotion of the oxygen evolution reaction via the reconstructed active phase of perovskite oxide," *Journal of Materials Chemistry A*, vol. 10, no. 5, pp. 2271–2279, 2022.
- [94] J. Balej, "Electrocatalysts for oxygen evolution in advanced water electrolysis," *International journal of hydrogen energy*, vol. 10, no. 2, pp. 89–99, 1985.
- [95] L. A. Cheah, G. V. Manohara, M. M. Maroto-Valer, and S. Garcia, "Impact of Synthesis Method and Metal Salt Precursors on the CO₂ Adsorption Performance of Layered Double Hydroxides Derived Mixed Metal Oxides," *Frontiers in Energy Research*, vol. 10, no. May, pp. 1–19, 2022.
- [96] G. Gao, Z. Zhu, J. Zheng, Z. Liu, Q. Wang, and Y. Yan, "Ultrathin magnetic Mg-Al LDH photocatalyst for enhanced CO₂ reduction: Fabrication and mechanism," *Journal of Colloid and Interface Science*, vol. 555, pp. 1–10, nov 2019.
- [97] M. Etzi Coller Pascuzzi, A. J. Man, A. Goryachev, J. P. Hofmann, and E. J. Hensen, "Investigation of the stability of NiFe-(oxy)hydroxide anodes in alkaline water electrolysis under industrially relevant conditions," *Catalysis Science and Technology*, vol. 10, no. 16, pp. 5593–5601, 2020.
- [98] D. Tyndall, M. J. Craig, L. Gannon, C. McGuinness, N. McEvoy, A. Roy, M. García-Melchor, M. P. Browne, and V. Nicolosi, "Demonstrating the source of inherent instability in NiFe LDH-based OER electrocatalysts," *Journal of Materials Chemistry A*, vol. 11, no. 8, pp. 4067–4077, 2023.
- [99] K. Yan, T. Lafleur, J. Chai, and C. Jarvis, "Facile synthesis of thin NiFe-layered double hydroxides nanosheets efficient for oxygen evolution," *Electrochemistry Communications*, vol. 62, pp. 24–28, 2016.
- [100] Q. Luo, M. Peng, X. Sun, Y. Luo, and A. M. Asiri, "Efficient electrochemical water splitting catalyzed by electrodeposited NiFe nanosheets film," *International Journal of Hydrogen Energy*, vol. 41, pp. 8785–8792, jun 2016.
- [101] B. M. Hunter, W. Hieringer, J. R. Winkler, H. B. Gray, and A. M. Mü, "Effect of interlayer anions on [NiFe]-LDH nanosheet water oxidation activity †," *Energy Environ. Sci*, vol. 9, p. 1734, 2016.

- [102] F. Dionigi and P. Strasser, “NiFe-Based (Oxy)hydroxide Catalysts for Oxygen Evolution Reaction in Non-Acidic Electrolytes,” *Advanced Energy Materials*, vol. 6, no. 23, 2016.
- [103] Q. Wang and D. O’Hare, “Recent advances in the synthesis and application of layered double hydroxide (LDH) nanosheets,” *Chemical Reviews*, vol. 112, no. 7, p. 4124–4155, 2012.
- [104] J. A. Carrasco, R. Sanchis-Gual, A. Seijas-Da Silva, G. Abellan, and E. Coronado, “Influence of the interlayer space on the water oxidation performance in a family of surfactant-intercalated NiFe-layered double hydroxides,” *Chemistry of Materials*, vol. 31, no. 17, pp. 6798–6807, 2019.
- [105] D. Zhou, Z. Cai, Y. Bi, W. Tian, M. Luo, Q. Zhang, Q. Xie, J. Wang, Y. Li, Y. Kuang, X. Duan, M. Bajdich, S. Siahrostami, and X. Sun, “Effects of redox-active interlayer anions on the oxygen evolution reactivity of NiFe-layered double hydroxide nanosheets,” *Nano Research*, vol. 11, no. 3, pp. 1358–1368, 2018.
- [106] F. Dionigi, Z. Zeng, I. Sinev, T. Merzdorf, S. Deshpande, M. B. Lopez, S. Kunze, I. Zegkinoglou, H. Sarodnik, D. Fan, A. Bergmann, J. Drnec, J. F. de Araujo, M. Gliech, D. Teschner, J. Zhu, W. X. Li, J. Greeley, B. Roldan Cuenya, and P. Strasser, “In-situ structure and catalytic mechanism of NiFe and CoFe layered double hydroxides during oxygen evolution,” *Nature Communications*, vol. 11, no. 1, 2020.
- [107] Y. Kong, Y. Wang, W. Chu, and Z. Liu, “Tailoring surface and interface electronic structure of NiFe LDH via V doping for enhanced oxygen evolution reaction,” *Journal of Alloys and Compounds*, vol. 885, p. 160929, dec 2021.
- [108] M. Rosa, D. Marani, G. Perin, S. B. Simonsen, P. Zielke, A. Glisenti, R. Kiebach, A. Lesch, and V. Esposito, “Impact of cation redox chemistry on continuous hydrothermal synthesis of 2D-Ni(Co/Fe) hydroxides,” *Reaction Chemistry and Engineering*, vol. 4, no. 12, pp. 2060–2073, 2019.
- [109] L. Dang, H. Liang, J. Zhuo, B. K. Lamb, H. Sheng, Y. Yang, and S. Jin, “Direct Synthesis and Anion Exchange of Noncarbonate-Intercalated NiFe-Layered Double Hydroxides and the Influence on Electrocatalysis,” *Chemistry of Materials*, vol. 30, no. 13, pp. 4321–4330, 2018.

- [110] S. Klaus, M. W. Louie, L. Trotochaud, and A. T. Bell, "Role of catalyst preparation on the electrocatalytic activity of $\text{Ni}_{1-x}\text{Fe}_x\text{OOH}$ for the oxygen evolution reaction," *The Journal of Physical Chemistry C*, vol. 119, no. 32, pp. 18303–18316, 2015.
- [111] M. W. Louie and A. T. Bell, "An investigation of thin-film Ni-Fe oxide catalysts for the electrochemical evolution of oxygen," *Journal of the American Chemical Society*, vol. 135, no. 33, pp. 12329–12337, 2013.
- [112] H. Li, X. Wang, T. Wang, and F. Xiao, "A facile, green and time-saving method to prepare partially crystalline NiFe layered double hydroxide nanosheets on nickel foam for superior OER catalysis," *Journal of Alloys and Compounds*, vol. 844, p. 156224, 2020.
- [113] C. Morcos, A. Seron, N. Maubec, I. Ignatiadis, and S. Betelu, "Comprehension of the Route for the Synthesis of Co/Fe LDHs via the Method of Coprecipitation with Varying pH," *Nanomaterials*, vol. 12, no. 9, 2022.
- [114] X. Yang, C. J. Wang, C. C. Hou, W. F. Fu, and Y. Chen, "Self-Assembly of Ni-Fe Layered Double Hydroxide on Fe Foam as 3D Integrated Electrocatalysts for Oxygen Evolution: Dependence of the Catalytic Performance on Anions under in Situ Condition," *ACS Sustainable Chemistry and Engineering*, vol. 6, no. 3, pp. 2893–2897, 2018.
- [115] G. Młynarek, M. Paszkiewicz, and A. Radniecka, "The effect of ferric ions on the behaviour of a nickelous hydroxide electrode," *Journal of Applied Electrochemistry*, vol. 14, no. 2, pp. 145–149, 1984.
- [116] D. A. Corrigan and S. P. Maheswari, "Catalysis of the Oxygen Evolution Reaction By Trace Iron Impurities in Thin Film Nickel Oxide Electrodes.," *Electrochemical Society Extended Abstracts*, vol. 85-1, pp. 934–935, 1987.
- [117] D. A. Corrigan and R. M. Bendert, "Effect of Coprecipitated Metal Ions on the Electrochemistry of Nickel Hydroxide Thin Films: Cyclic Voltammetry in 1M KOH," *Journal of The Electrochemical Society*, vol. 136, no. 3, pp. 723–728, 1989.
- [118] S. Anantharaj, S. Kundu, and S. Noda, "“The Fe Effect”: A review unveiling the critical roles of Fe in enhancing OER activity of Ni and Co based catalysts," *Nano Energy*, vol. 80, no. February 2020, p. 105514, 2021.

- [119] J. Bao, Z. Wang, J. Xie, L. Xu, F. Lei, M. Guan, Y. Zhao, Y. Huang, H. Li, R. Li, . Chemcomm, and C. Communication, "A ternary cobalt-molybdenum-vanadium layered double hydroxide nanosheet array as an efficient bifunctional electrocatalyst for overall water splitting \dagger ," *Chem. Commun.*, vol. 55, p. 3521, 2019.
- [120] Y. Gan, Z. Li, Y. Ye, X. Dai, F. Nie, X. Yin, Z. Ren, B. Wu, Y. Cao, R. Cai, X. Zhang, and W. Song, "Doping Mo into NiFe LDH/NiSe Heterostructure to Enhance Oxygen Evolution Activity by Synergistically Facilitating Electronic Modulation and Surface Reconstruction," *ChemSusChem*, vol. 15, no. 20, 2022.
- [121] Y. Yu, S. Chen, L. Yu, L. Wu, B. Mcelhenny, S. Song, D. Luo, F. Zhang, and Z. Ren, "Ultrafast room-temperature synthesis of porous S-doped Ni/Fe (oxy)hydroxide electrodes for oxygen evolution catalysis in seawater splitting \dagger ," *Energy Environ. Sci.*, vol. 13, p. 3439, 2020.
- [122] M. Liu, K. A. Min, B. Han, and L. Y. S. Lee, "Interfacing or Doping? Role of Ce in Highly Promoted Water Oxidation of NiFe-Layered Double Hydroxide," *Advanced Energy Materials*, vol. 11, no. 33, pp. 1–11, 2021.
- [123] Z. Cai, D. Zhou, M. Wang, S. M. Bak, Y. Wu, Z. Wu, Y. Tian, X. Xiong, Y. Li, W. Liu, S. Siahrostami, Y. Kuang, X. Q. Yang, H. Duan, Z. Feng, H. Wang, and X. Sun, "Introducing Fe²⁺ into Nickel–Iron Layered Double Hydroxide: Local Structure Modulated Water Oxidation Activity," *Angewandte Chemie - International Edition*, vol. 57, no. 30, pp. 9392–9396, 2018.
- [124] L. Wu, L. Yu, F. Zhang, D. Wang, D. Luo, S. Song, C. Yuan, A. Karim, S. Chen, and Z. Ren, "Facile synthesis of nanoparticle-stacked tungsten-doped nickel iron layered double hydroxide nanosheets for boosting oxygen evolution reaction," *Journal of Materials Chemistry A*, vol. 8, no. 16, pp. 8096–8103, 2020.
- [125] R. M. Ramsundar, J. Debgupta, V. K. Pillai, and P. A. Joy, "Co₃O₄ Nanorods—Efficient Non-noble Metal Electrocatalyst for Oxygen Evolution at Neutral pH," *Electrocatalysis*, vol. 6, no. 4, pp. 331–340, 2015.
- [126] H. Shi and G. Zhao, "Water oxidation on spinel nico₂o₄ nanoneedles anode: microstructures, specific surface character, and the enhanced electrocatalytic performance," *The Journal of Physical Chemistry C*, vol. 118, no. 45, pp. 25939–25946, 2014.

- [127] X. Wu, X. Han, X. Ma, W. Zhang, Y. Deng, C. Zhong, and W. Hu, "Morphology-controllable synthesis of zn-co-mixed sulfide nanostructures on carbon fiber paper toward efficient rechargeable zinc-air batteries and water electrolysis," *ACS applied materials & interfaces*, vol. 9, no. 14, pp. 12574–12583, 2017.
- [128] Y. Zhang, S. Chao, X. Wang, H. Han, Z. Bai, and L. Yang, "Hierarchical co9s8 hollow microspheres as multifunctional electrocatalysts for oxygen reduction, oxygen evolution and hydrogen evolution reactions," *Electrochimica Acta*, vol. 246, pp. 380–390, 2017.
- [129] M. Chauhan, K. P. Reddy, C. S. Gopinath, and S. Deka, "Copper cobalt sulfide nanosheets realizing a promising electrocatalytic oxygen evolution reaction," *ACS Catalysis*, vol. 7, no. 9, pp. 5871–5879, 2017.
- [130] J. Jiang, S. Lu, H. Gao, X. Zhang, and H.-Q. Yu, "Ternary fe-ni-co ultrathin nanosheets as an electrocatalyst for both oxygen evolution and reduction reactions," *Nano Energy*, vol. 27, pp. 526–534, 2016.
- [131] P. Li and H. C. Zeng, "Bimetallic ni-fe phosphide nanocomposites with a controlled architecture and composition enabling highly efficient electrochemical water oxidation," *Journal of Materials Chemistry A*, vol. 6, no. 5, pp. 2231–2238, 2018.
- [132] W. Li, X. Gao, D. Xiong, F. Xia, J. Liu, W.-G. Song, J. Xu, S. M. Thalluri, M. F. Cerqueira, X. Fu, *et al.*, "Vapor-solid synthesis of monolithic single-crystalline cop nanowire electrodes for efficient and robust water electrolysis," *Chemical science*, vol. 8, no. 4, pp. 2952–2958, 2017.
- [133] J. Li, M. Yan, X. Zhou, Z.-Q. Huang, Z. Xia, C.-R. Chang, Y. Ma, and Y. Qu, "Mechanistic insights on ternary ni2-xcoxp for hydrogen evolution and their hybrids with graphene as highly efficient and robust catalysts for overall water splitting," *Advanced Functional Materials*, vol. 26, no. 37, pp. 6785–6796, 2016.
- [134] D. Li, H. Baydoun, B. Kulikowski, and S. L. Brock, "Boosting the catalytic performance of iron phosphide nanorods for the oxygen evolution reaction by incorporation of manganese," *Chemistry of Materials*, vol. 29, no. 7, pp. 3048–3054, 2017.

- [135] X. Han, C. Yu, J. Yang, C. Zhao, H. Huang, Z. Liu, P. M. Ajayan, and J. Qiu, "Mass and charge transfer coenhanced oxygen evolution behaviors in coFe-layered double hydroxide assembled on graphene," *Advanced Materials Interfaces*, vol. 3, no. 7, p. 1500782, 2016.
- [136] J. Jiang, A. Zhang, L. Li, and L. Ai, "Nickel–cobalt layered double hydroxide nanosheets as high-performance electrocatalyst for oxygen evolution reaction," *Journal of Power Sources*, vol. 278, pp. 445–451, 2015.
- [137] K. Fan, H. Chen, Y. Ji, H. Huang, P. M. Claesson, Q. Daniel, B. Philippe, H. Rensmo, F. Li, Y. Luo, *et al.*, "Nickel–vanadium monolayer double hydroxide for efficient electrochemical water oxidation," *Nature communications*, vol. 7, no. 1, p. 11981, 2016.
- [138] Z. Lu, L. Qian, Y. Tian, Y. Li, X. Sun, and X. Duan, "Ternary nifemn layered double hydroxides as highly-efficient oxygen evolution catalysts," *Chemical Communications*, vol. 52, no. 5, pp. 908–911, 2016.
- [139] Y. Cui, Y. Xue, R. Zhang, J. Zhang, X. Li, and X. Zhu, "Vanadium–cobalt oxyhydroxide shows ultralow overpotential for the oxygen evolution reaction," *Journal of Materials Chemistry A*, vol. 7, no. 38, pp. 21911–21917, 2019.
- [140] Z.-F. Huang, J. Song, Y. Du, S. Xi, S. Dou, J. M. V. Nsanzimana, C. Wang, Z. J. Xu, and X. Wang, "Chemical and structural origin of lattice oxygen oxidation in co–zn oxyhydroxide oxygen evolution electrocatalysts," *Nature Energy*, vol. 4, no. 4, pp. 329–338, 2019.
- [141] F. Yan, C. Zhu, C. Li, S. Zhang, X. Zhang, and Y. Chen, "Highly stable three-dimensional nickel–iron oxyhydroxide catalysts for oxygen evolution reaction at high current densities," *Electrochimica Acta*, vol. 245, pp. 770–779, 2017.
- [142] E. A. Feigenbaum and B. G. Buchanan, "DENDRAL and META-DENDRAL: Roots of knowledge systems and expert system applications," 1978.
- [143] R. D. King, J. Rowland, S. G. Oliver, M. Young, W. Aubrey, E. Byrne, M. Liakata, M. Markham, P. Pir, L. N. Soldatova, A. Sparkes, K. E. Whelan, and A. Clare, "The automation of science," *Science*, vol. 324, no. 5923, pp. 85–89, 2009.

- [144] R. D. King, "Rise of the robo scientists," *Scientific American*, vol. 304, no. 1, pp. 73–77, 2011.
- [145] J. B. Gerken, S. E. Shaner, R. C. Massé, N. J. Porubsky, and S. S. Stahl, "A survey of diverse earth abundant oxygen evolution electrocatalysts showing enhanced activity from Ni-Fe oxides containing a third metal," *Energy and Environmental Science*, vol. 7, no. 7, pp. 2376–2382, 2014.
- [146] A. Sparkes, W. Aubrey, E. Byrne, A. Clare, M. N. Khan, M. Liakata, M. Markham, J. Rowland, L. N. Soldatova, K. E. Whelan, M. Young, and R. D. King, "Towards Robot Scientists for autonomous scientific discovery," *Automated Experimentation*, vol. 2, no. 1, 2010.
- [147] H. Liu, N. Stoll, S. Junginger, and K. Thurow, "Mobile robot for life science automation," *International Journal of Advanced Robotic Systems*, vol. 10, pp. 1–14, 2013.
- [148] Y. Xie, K. Sattari, C. Zhang, and J. Lin, "Toward autonomous laboratories: Convergence of artificial intelligence and experimental automation," *Progress in Materials Science*, vol. 132, p. 101043, feb 2023.
- [149] A. Dave, J. Mitchell, K. Kandasamy, H. Wang, S. Burke, B. Paria, B. Póczos, J. Whitacre, and V. Viswanathan, "Autonomous Discovery of Battery Electrolytes with Robotic Experimentation and Machine Learning," *Cell Reports Physical Science*, vol. 1, p. 100264, dec 2020.
- [150] C. W. Coley, N. S. Eyke, and K. F. Jensen, "Autonomous Discovery in the Chemical Sciences Part II: Outlook," *Angewandte Chemie - International Edition*, vol. 59, no. 52, pp. 23414–23436, 2020.
- [151] C. W. Coley, N. S. Eyke, and K. F. Jensen, "Autonomous Discovery in the Chemical Sciences Part I: Progress," *Angewandte Chemie - International Edition*, vol. 59, no. 51, pp. 22858–22893, 2020.
- [152] K. McCullough, T. Williams, K. Mingle, P. Jamshidi, and J. Lauterbach, "High-throughput experimentation meets artificial intelligence: A new pathway to catalyst discovery," *Physical Chemistry Chemical Physics*, vol. 22, pp. 11174–11196, may 2020.

- [153] M. M. Flores-Leonar, L. M. Mejía-Mendoza, A. Aguilar-Granda, B. Sanchez-Lengeling, H. Tribukait, C. Amador-Bedolla, and A. Aspuru-Guzik, "Materials Acceleration Platforms: On the way to autonomous experimentation," *Current Opinion in Green and Sustainable Chemistry*, vol. 25, p. 100370, oct 2020.
- [154] B. P. MacLeod, F. G. Parlane, T. D. Morrissey, F. Häse, L. M. Roch, K. E. Dettelbach, R. Moreira, L. P. Yunker, M. B. Rooney, J. R. Deeth, V. Lai, G. J. Ng, H. Situ, R. H. Zhang, M. S. Elliott, T. H. Haley, D. J. Dvorak, A. Aspuru-Guzik, J. E. Hein, and C. P. Berlinguette, "Self-driving laboratory for accelerated discovery of thin-film materials," *Science Advances*, vol. 6, no. 20, 2020.
- [155] B. Burger, P. M. Maffettone, V. V. Gusev, C. M. Aitchison, Y. Bai, X. Wang, X. Li, B. M. Alston, B. Li, R. Clowes, N. Rankin, B. Harris, R. S. Sprick, and A. I. Cooper, "A mobile robotic chemist," *Nature*, vol. 583, no. 7815, pp. 237–241, 2020.
- [156] F. Schüth and D. Demuth, "High-Throughput-Experimentation in der heterogenen Katalyse," *Chemie-Ingenieur-Technik*, vol. 78, no. 7, pp. 851–861, 2006.
- [157] F. Balkenhohl, C. Von dem Bussche-Hünnefeld, A. Lansky, and C. Zechel, "Combinatorial synthesis of small organic molecules," *Angewandte Chemie (International Edition in English)*, vol. 35, no. 20, pp. 2288–2337, 1996.
- [158] X. D. Xiang, X. Sun, G. Briceño, Y. Lou, K.-A. Wang, H. Chang, W. G. Wallace-Freedman, S.-W. Chen, and P. G. Schultz, "A combinatorial approach to materials discovery," *Science*, vol. 268, no. 5218, pp. 1738–1740, 1995.
- [159] A. Hagemeyer, P. Strasser, and A. F. Volpe, *High-Throughput Screening in Heterogeneous Catalysis*. Wiley-VCH, 2005.
- [160] A. F. Volpe and C. G. Lugmair, *High-Throughput Heterogeneous Catalyst Research, Development, Scale-Up, and Production Support*, ch. 74, pp. 611–661. John Wiley & Sons, Ltd, 2020.
- [161] J. M. Granda, L. Donina, V. Dragone, D. L. Long, and L. Cronin, "Controlling an organic synthesis robot with machine learning to search for new reactivity," *Nature*, vol. 559, no. 7714, pp. 377–381, 2018.

- [162] S. Mirjalili, "Dragonfly algorithm: a new meta-heuristic optimization technique for solving single-objective, discrete, and multi-objective problems," *Neural Computing and Applications*, vol. 27, no. 4, pp. 1053–1073, 2016.
- [163] P. J. Kitson, S. Glatzel, and L. Cronin, "The digital code driven autonomous synthesis of ibuprofen automated in a 3D-printer-based robot," *Beilstein Journal of Organic Chemistry*, vol. 12, pp. 2776–2783, 2016.
- [164] A. F. Zahrt, J. J. Henle, B. T. Rose, Y. Wang, W. T. Darrow, and S. E. Denmark, "Prediction of higher-selectivity catalysts by computer-driven workflow and machine learning," *Science*, vol. 363, no. 6424, 2019.
- [165] G. L. Hart, T. Mueller, C. Toher, and S. Curtarolo, "Machine learning for alloys," *Nature Reviews Materials*, vol. 6, no. 8, pp. 730–755, 2021.
- [166] T. Lombardo, M. Duquesnoy, H. El-Bouysidy, F. Årén, A. Gallo-Bueno, P. B. Jørgensen, A. Bhowmik, A. Demortière, E. Ayerbe, F. Alcaide, M. Reynaud, J. Carrasco, A. Grimaud, C. Zhang, T. Vegge, P. Johansson, and A. A. Franco, "Artificial Intelligence Applied to Battery Research: Hype or Reality?," *Chemical Reviews*, vol. 122, no. 12, pp. 10899–10969, 2022.
- [167] H. Mai, T. C. Le, D. Chen, D. A. Winkler, and R. A. Caruso, "Machine Learning for Electrocatalyst and Photocatalyst Design and Discovery," *Chemical Reviews*, vol. 122, no. 16, pp. 13478–13515, 2022.
- [168] N. Srinivas, A. Krause, S. M. Kakade, and M. Seeger, "Gaussian process optimization in the bandit setting: No regret and experimental design," *arXiv preprint arXiv:0912.3995*, 2009.

